COMPUTATIONAL FRAMEWORK FOR LESION DETECTION AND RESPONSE ASSESSMENT BASED UPON PHYSIOLOGICAL IMAGING FOR SUPPORTING RADIATION THERAPY OF BRAIN METASTASES

BY

REZA FARJAM

A dissertation submitted in partial fulfillment
of the requirements for the degree of
Doctor of Philosophy
(Biomedical Engineering)
in the University of Michigan
2013

Doctoral Committee:

Professor Yue Cao, Co-Chair
Professor Douglas C. Noll, Co-Chair
Professor J. Brian Fowlkes,
Research Associate Professor Luis Hernandez-Garcia ,

TO MY PARENTS

HABIB FARJAM AND HOMA FARHAD

ACKNOWLEDGMENTS

TABLE OF CONTENTS

Chapter III: Physiological imaging-defined, response-driven subvolumes of a tumor

Chapter IV: DCE-MRI Defined Subvolumes of a Tumor for Therapy Assessment

Chapter V: Diffusion Abnormality Index: a New Imaging Biomarker for Early Assessment of Tumor Response to Therapy

Chapter VI: Conclusion and Future Works 95

References……………………………………………………………………………… 104

LIST OF FIGURES

Chapter V

Chapter VI

LIST OF TABLES

Chapter II

Chapter III

Chapter IV

Chapter V

Chapter I

Introduction

Brain metastases are the most prevalent form of cancer in the central nervous system,[1] and up to 45% of cancer patients eventually develop brain metastases during the course of their illness,[2] wherein 60% of which are contributed from lung and breast cancers as primary sites [3]. Brain metastases have a poor prognosis, but modern treatments allow patients to live months and sometimes years after diagnosis [4-5]. In the past few decades, the primary cancer treatments included radiation therapy, chemotherapy and surgery. Radiation therapy plays a critical role in the treatment of brain metastases, and includes whole brain fractionated radiation therapy [4], and stereotactic radiosurgery [5]. Chemotherapy is rarely used for the treatment of brain metastases, as chemotherapeutic agents penetrate the blood brain barrier poorly. However, some cancers such as lymphomas, small cell lung carcinomas and breast cancer are highly chemo-sensitive, and hence chemotherapy may be used to treat extra-cranial sites of metastatic disease in these cancers [2]. Brain metastases are often managed surgically, with maximum surgical resection followed by stereotactic radiosurgery or whole brain radiotherapy, leading to a superior survival rate compared to whole brain irradiation alone [2]. Detecting the precise number of brain metastases, their size, and early assessment of their response to a therapy is crucial to choose an appropriate treatment for the patient and modify the

course treatment if needed. Hence, this dissertation is aimed to address the current state and limitations of brain metastases detection and to develop physiological imaging biomarkers for therapy guidance and early prediction of brain metastases response to radiation therapy.

I.A Computer-aided Detection of Brain Metastases

The number and size of brain metastases are crucial to choose whole brain radiation therapy (WBRT) vs. stereotactic radiosurgery (SRS) in patients with brain metastases [4-6]. Usually 3 lesions or less with the sizes smaller than 3cm in diameter may lead to selection of SRS [6]. Failure to accurately diagnosis of the presence of small lesions can result in inappropriate selection of treatment. At present, radiologists diagnose brain metastases using contrast-enhanced MRI [7] on which the lesions are highlighted due to disrupted blood-tumor barriers. However, manually screening MR images for diagnosis of brain metastases is prone to potential errors [8], especially for small lesions, given the limitation of 2D screening of a large number of brain MRI slices. Hence, computer-aided automatic screening of MR images is of interest. In this dissertation, an assistive technology was developed to help radiologists detect small lesions, with diameters <5mm, in post-Gd T1-weighted magnetic resonance imaging (MRI) data.

I.B Response Assessment of Brain Metastases to Radiation Therapy

A recent study [9] has shown that WBRT produces a decrease in neurocognitive status compared to SRS. Hence, more and more patients are receiving focal treatment for brain metastases. As WBRT is being done less, more patients are developing new lesions after treatment of the initial lesions, and thus are being treated to new lesions over time. Thus, the needs for developing a tool to early assess the brain metastasis response to therapy will become more and more important as patients receive more and more focal treatment. Also, it is hypothesized that dose painting of the physiological imaging-defined subvolumes of the tumors could lead to a better outcome than distributing a uniform dose within a target volume defined by anatomic imaging. Hence, the main goal in this dissertation is to develop a general method to define the physiological target volumes of a tumor based upon multiple physiological imaging and then test their complementary roles for assessment of brain metastases response to radiation therapy.

I.B.1 Response assessment based upon tumor vascular properties

As tumors grow and progress, the surrounding vascular supply is no longer sufficient to support the increasing metabolic demands of the rapidly proliferating tumor cells [10]. The regional hypoxia and hypoglycemia then precede leading to escalation of vasoactive endothelial growth factor (VEGF) regulation through which the process of new blood vessel formation from the existing vasculature, known as angiogenesis, Fig. 1(A), is initiated [11]-[12]. The new vessels formed in this way often lack the elegant structure of

the normal vasculature, hence, resulting in high permeability and leakage of the endothelial membrane [13]. Tumor growth can also disrupt the existing vasculature and facilitate the blood-brain barrier (BBB) breakdown, which ends up to a network of leaky microvasculature. The latter itself expedites the endothelial mitosis and new vessel formation, which has a direct effect on ingrowth of the new vessels into the interstitial stroma. Tumor vasculature map plays critical roles not only in supplying nutrients and oxygen to the demanding cells but also in providing a roadmap for tumor infiltration and a feedback with tumor hypoxia and necrosis [14]. This indicates that regulation of the angiogenesis process and prevention of leaky vasculature formation [15]–[16] within a tumor could have a major role in efficacy of the therapeutic approach used to cure the malignant tumors. Hence, alterations of the perfusion and vascular parameter maps within tumors could be a biomarker to measure the effect of the anti-angiogenic drugs on preventing the formation of the tumor vasculature.

http://www.gene.com/gene/research/focusareas/oncology/angiogenesis.html
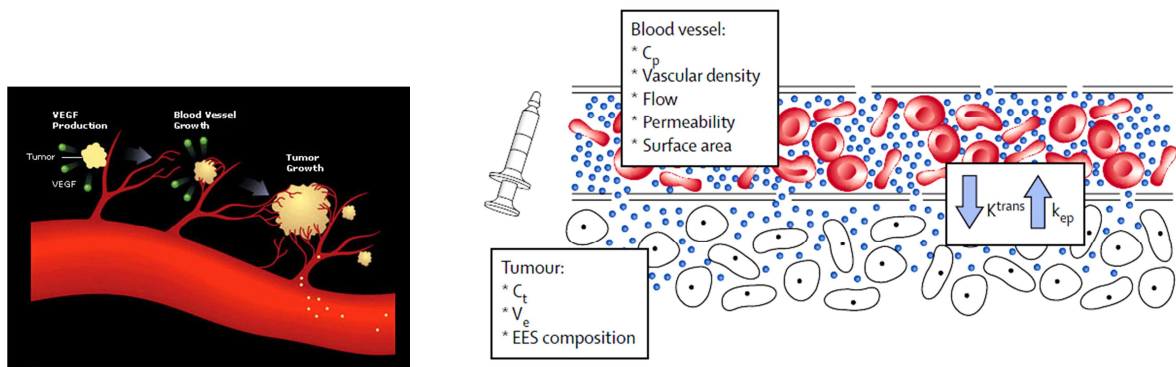
(A)

C_p = concentration of contrast in plasma;
C_t = concentration of contrast in tumor extracellular–extra-vascular space (EES);
V_e = fractional volume of EES;
k^{trans} = volume transfer constant between plasma and EES;
k_{ep} = rate constant between EES and plasma.

(B)

Fig. I.1. (A) Angiogenesis and (B) Factors influencing the contrast enhancement pattern. M. Zahra et al. *Lancet Oncology*, 8, pp. 63–74, 2007.

Dynamic contrast enhanced magnetic resonance imaging (DCE-MRI) is a noninvasive imaging tool, which is extensively used in oncology for diagnosis and therapy assessment, [17] and also as an imaging biomarker for development of anti-angiogenic drugs [18]. The DCE-MRI technique is based upon rapid acquisition of a series of T1-weighted images from tissue of interest before, during and after intravenous bolus injection of a gadolinium-based contrast agent (CA) [19], Fig. 1(B). As the CA perfuses into the tissue under investigation, T1 values of the tissue water decrease to an extent which depends upon the CA concentration. Hence, the characteristic signal intensity time course, relating to the CA concentration, in a region of interest or a voxel of the tissue can be subsequently analyzed by a pharmacokinetic (PK) model. By fitting the DCE-MRI data to a PK model, a set of volumetric maps of physiological parameters can be obtained, for example, tissue perfusion, microvascular permeability and extravascular extracellular volume [20]. Longitudinal changes in maps of the physiological parameters of tissue of interest from pre- to post-treatment could aid in for assessment and prediction of treatment response and outcome as well as for drug development [21-22]. In the chapter III of this dissertation, we aimed to develop an algorithm to extract the perfusion imaging-defined "phenotype" subvolumes of a tumor and to relate them to treatment response and outcome. However, the physiological parameter maps derived from the PK models involve in a series of uncertainties [23]. Hence, the chapter IV is devoted to develop a general framework to derive a response-predictor from DCE-MRI data without using the PK model in order to have a semi-automated or fully automated tool for supporting clinic decision-making, and to compare the subvolumes determined by this approach with the physiological imaging parameter defined ones.

I.B.2 Response assessment based upon tumor cellularity properties

Diffusion weighted magnetic resonance imaging (DW-MRI) has been shown to be an imaging biomarker for assessing tumor cellularity and aggressiveness and early response to therapy in various cancers [24-27]. The DW-MRI acquisition is rapid, noninvasive, without exogenous contrast agent, and no ionizing radiation. The apparent diffusion coefficient (ADC), quantified from DW-MRI, measures water mobility in tissue, and is sensitive to cellular density, extracellular space tortuosity, and intactness of cellular membrane [24-25]. However, quantification of an ADC change in the tumor is still a challenge and affects its sensitivity and specificity for early prediction of tumor response to therapy, mainly because the ADCs in a tumor manifest a heterogeneous distribution [26-27] due to spatial variation in cellular density, cell structure and water content. In a high cellular region, the mobility of water molecules is restricted, and thus the ADC is low; while in a region with necrosis or edema, water molecules move more freely or are in a high content, and thus the ADC is high. Animal studies have shown that the ADC is inversely correlated with tumor cellularity [26]. When a tumor responds to treatment, the ADC in the high cellular region could increase due to cell shrinkage followed by phagocytosis [27]. Also, the ADC in the edema region could decrease due drainage of water into cells [27]. Hence, the directions of changes depend upon where the ADCs are measured and what the original values of the ADCs are. Therefore, the heterogeneity in the tumor ADCs and the complex changes result in that a change in the mean ADC of a tumor is a poor indicator for therapy response. In this dissertation, we also aim to quantify the diffusion abnormality of a brain metastatic tumor as a quantitative indicator of tumor cellular properties for early assessment of tumor response to therapy.

6

The organization of this dissertation is as follows. In chapter II, a computer-aided detection system for automatic detection of brain metastases in post-Gd T1-W magnetic resonance imaging is explained. The chapter III is devoted to describe the general framework to extract the subvolumes of a tumor from the physiological imaging data and to show the results of the regional cerebral blood volume (rCBV) and Gd-DTAP transfer constant from plasma to tissue (K^{trans}) for assessing brain metastases response to therapy. The next chapter describes the general framework to derive the similar response-predictor from the DCE-MRI data without using a PK model and compare the results with ones from chapter III. In chapter V, we show our proposed approach to quantify the diffusion abnormality of tumor. In the final chapter, the future directions, combining multiple physiological and metabolic imaging parameters to achieve a better response-predictor, will be discussed, and the preliminary results of combining the perfusion and diffusion parameters will be described.

An automated approach for computer-aided detection of brain metastases in post-Gadolinium T1-weighted magnetic resonance imaging

II.A. Introduction

As mentioned earlier, selection of WBRT versus SRS highly depends on the number of lesions and their size and failure to accurately diagnosis of the presence of small lesions can result in inappropriate selection of treatment. At present, radiologists diagnose brain metastases using contrast-enhanced MRI [7] on which the lesions are highlighted due to disrupted blood-tumor barriers. However, manually screening MR images for diagnosis of brain metastases is prone to potential errors [8] especially for small lesions. Hence, to address the limitations of the 2D screening, this chapter aims to develop a computer-aided detection system for automatic screening of MR images.

So far, several computer-aided detection (CAD) systems using template matching [28] have been proposed for the detection of lesions, especially in the lung [29-34] and breast [35-36]. In template matching, a set of templates with different resolutions is usually cross-correlated with regions of interest to localize objects of an unknown size. The most crucial task in template design is to optimally determine the shape, size, number of templates, and a cross-correlation coefficient threshold in order to achieve high sensitivity

and specificity of lesion detection as well as computation speed. Currently, most CAD systems using template matching have been developed for CT or radiography, in which nodules are usually surrounded by a fairly homogeneous background. One study adopted a CAD system originally developed for the detection of lung nodules on CT to detect brain metastases from contrast-enhanced MRI [37]. This work demonstrated the suitability of using spherical templates to detect brain metastatic lesions, which are often observed as bright spherical-like solid masses on contrast-enhanced MRI. However, as a lesion grows, a necrotic region may develop in the center of the mass. This previous work did not take into account the pattern of necrotic regions in their template design, which affected the performance of the CAD system. Most importantly, this previous work did not optimize the template set in design with respect to the size and shape of the lesions, and noise and intensity variation in contrast-enhanced MRI, which resulted in a large number of false positives. Also, one important clinical issue for the diagnosis of brain metastases is that small lesions have been missed more frequently compared to large ones, for which a CAD system could potentially assist a radiologist in diagnosis. All these require a more comprehensive study in the design of CAD systems for brain metastatic lesions.

In this chapter, the newly developed CAD system for the detection of small brain metastases from contrast-enhanced MRI is explained[1]. The spherical shell templates are designed to simulate a tumor growth pattern. The theoretical and simulation analyses of effects of size and shape heterogeneity of lesions are then performed to optimize the number and size of the templates and the cross-correlation thresholds. It is also

---

[1] Farjam et al. An approach for computer-aided detection of brain metastases in post-Gd T1-W MRI. *Magnetic Resonance Imaging,* 30 (6): 824-836, 2012.

investigated how image factors, e. g., nodule-contrast to intensity variations in the nodule and background, affect the performance of the CAD system. Hence, a nodule enhancement strategy and a set of rule-based criteria to reduce false positives are proposed. To develop and evaluate the proposed system, nine (including 60 lesions) and twenty patients (186 Lesions) were used in the training and testing steps, respectively. The screening results from two neuroradiologists are also included in this study.

II.B. Materials and Methods

II.B.1 Template Design

Brain metastases, when small, are seen as sphere-like solid masses on contrast-enhanced MRI. As a lesion grows, a necrotic region starts developing at the center of the lesion. Hence, we designed our templates to mimic a brain tumor growth pattern simulated in a model [38] in which the diameter of the necrotic region, r_n, is non-linearly related to the diameter of the lesion as: $r_n = R - 0.53R^{\frac{2}{3}}$ (Fig. II.1A). We create a 3D spherical shell zero-mean mask as following (Fig. II.1B):

$$M_r = \begin{cases} 1 & r_n^2 \leq x^2 + y^2 + z^2 \leq R^2 \\ 0 & x^2 + y^2 + z^2 < r_n^2 \qquad |x|,|y|,|z| < |a| \quad \& \quad a = 2R \\ -\beta & x^2 + y^2 + z^2 > R^2 \end{cases} \qquad \textbf{(Equation II.1)}$$

where M_r denotes a mask at resolution r, and β normalizes the mask to have a zero mean. Since the necrotic region is not seen in all lesions, we set intensities in the necrotic zone to be zero, and thereby this area is excluded from analysis. For a given M_r, the mask volume, V_{Mr} is defined by the number of non-negative voxels (including zeros).
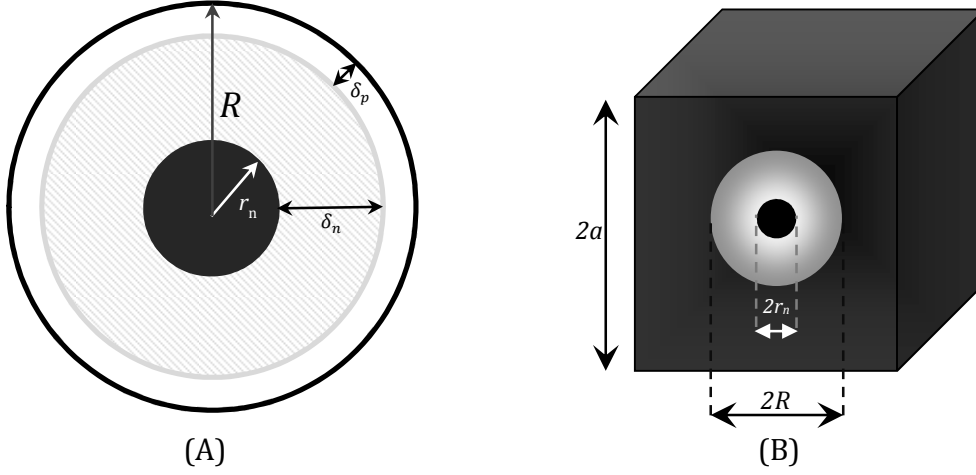
Fig. II.1. A simulated brain tumor growth pattern and a spherical shell template. (A) The brain tumor could have necrotic core (black), non-proliferative zone (crosshatched) and proliferative zone (white). (B): A spherical shell 3D template is designed based upon the simulated brain tumor growth pattern. Here, R, r_n, δ_n, and δ_p represent the radius of the lesion, the radius of the necrotic core, and the lengths of the non-proliferative and proliferative zones [38], respectively.

II.B.2 Selection of Template Size & Cross-Correlation Threshold

To localize a lesion by M_r, a cross-correlation coefficient (CCC) map between M_r and signal intensities of MR volume (V_{MR}) is calculated:

$$Corr_{M_r}(V_{MR}, i, j, k) = \frac{\sum_{x=-a}^{a}\sum_{y=-a}^{a}\sum_{z=-a}^{a}[M_r(x,y,z)] \cdot [w_{ijk}(x,y,z) - \overline{w}_{ijk}]}{(\sum_{x=-a}^{a}\sum_{y=-a}^{a}\sum_{z=-a}^{a}(M_r(x,y,z))^2 \cdot \sum_{x=-a}^{a}\sum_{y=-a}^{a}\sum_{z=-a}^{a}(w_{ijk}(x,y,z) - \overline{w}_{ijk})^2)}$$

$$w_{ijk}(x,y,z) = \begin{cases} V_{MR}(x,y,z) & \begin{array}{l} -a+i < x < a+i \\ -a+j < y < a+j \\ -a+k < z < a+k \end{array} \end{cases}$$ **(Equation II.2)**

where (i,j,k) represent voxel indices, $w_{ijk}(.)$ denotes intensity in a cubic region of V_{Mr} with a size of M_r centered at (i,j,k), $\overline{w}_{ijk}$ is the mean of w_{ijk}, $Corr_{M_r}(V_{Mr}, i, j, k)$ is the CCC between M_r and w_{ijk}. To localize a lesion, the cross correlation map is thresholded, all connected voxels above the threshold are grouped where each group represents one candidate lesion.

11

To localize all lesions, however, a set of multi-resolution masks had to be chosen. To select an optimal set of masks, {M_{ri}}, and a cross-correlation coefficient threshold, three main factors need to be considered: 1) tumor size variation, and 2) lesion shape variation, and 3) intensity variations within a tumors and its surrounding background. The effects of these factors on selecting an appropriate set of masks are quantitatively investigated and described in the following sub-sections. We designed {M_{ri}} and τ in a continuous space first, and then extended the concepts to a digital case.

II.B.2.i Design of {M_{ri}} and τ in a Continuous Space

To design a set of masks {M_{ri}} and a CCC threshold, τ, we first considered lesion size variations, but disregarded tumor shape and intensity variations for the time being. Let us consider a set of spherical tumors, {$T_{s,\,[i,\,i+1]}$}, with their volumes between two consecutive masks of M_{r_i} and $M_{r_{i+1}}$ (Fig. II.2) as:

$$V_{M_{r_i}} \leq V_{T_1} < \dots < V_{T_j} < \dots < V_{T_n} \leq V_{M_{r_{i+1}}}$$ **(Equation II.3)**
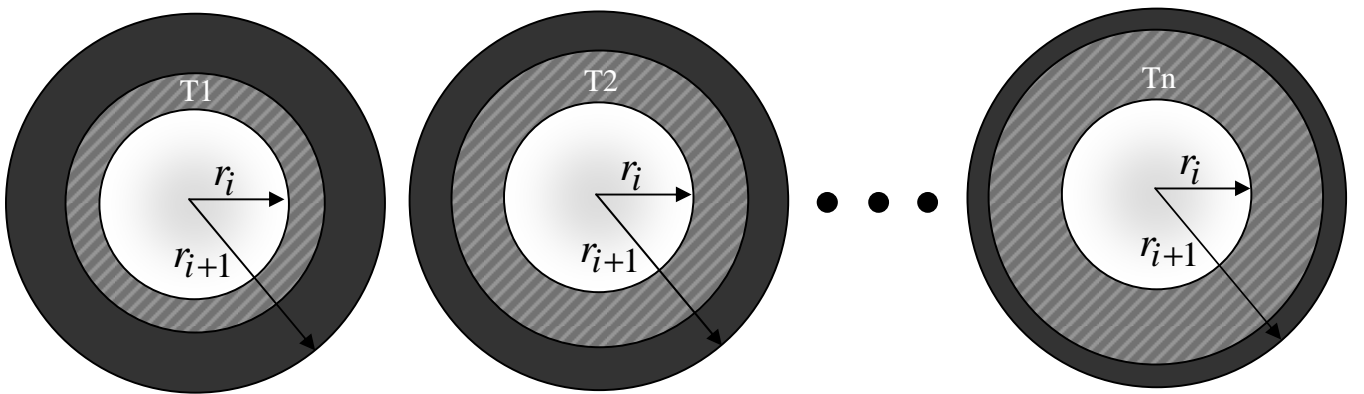
Fig. II.2. Cross sectional view of a set of spherical tumors ($T_1 < T_2 < \dots < T_n$) with radii (crosshatched) between two consecutive masks M_{ri} (light gray sphere) and M_{ri+1} (dark gray sphere). The two consecutive masks, M_{ri} and M_{ri+1} localize all tumors using a cross-correlation threshold determined by Eq. II.7.

where V_{T_j} and $V_{M_{ri}}$ are the volumes of the *j*th tumor and the *i*th mask, respectively. The CCC between T_j and M_{ri} or M_{ri+1} is determined by the number of mismatched voxels between the tumor and mask (we don't show the proof here).Fig. II.3 shows that the CCCs between $\{T_s\}$ and M_{ri} (or M_{ri+1}) form a right-side (or left-side) curve from the *ith* (or *i+1th*) mask. Also, the CCCs have the following orders:

$$Corr_{M_{ri,Right}}(T_j) > Corr_{M_{ri,Rightt}}(T_{j+1}) \qquad \textbf{(Equation II.4)}$$

$$Corr_{M_{ri+1,left}}(T_j) < Corr_{M_{ri+1,Left}}(T_{j+1}) \qquad \textbf{(Equation II.5)}$$

If a threshold, τ, of the CCC is selected at the intercept of the two CCC curves as:

$$\tau = Corr_{M_{r_i,Right}}(T_k) = Corr_{M_{r_{i+1}Left}}(T_k) \qquad \textbf{(Equation II.6)}$$

All tumors $\{T_{s,[i,i+1]}\}$ that have the volumes between M_{ri} and M_{ri+1} are detected by either M_{ri} or M_{ri+1}, depending upon the volume of the tumor smaller or greater than $T_k's$ (Fig. II.3). Using the same strategy, the threshold for the *i*+2th mask should be selected as:

$$Corr_{M_{r_{i+1},Left}}(T_k) = Coor_{M_{r_{i+1},Right}}(T'_n) = Corr_{M_{r_{i+2},Left}}(T'_n) = \dots \quad \textbf{(Equation II.7)}$$

where M_{ri+1} and M_{ri+2} localize the next set of tumors $\{T'_{s,[i+1,i+2]}\}$ (Fig. II.3). Note that a lower threshold value of τ can reduce the number of required masks by increasing the radius increment ($d_{i,i+1} = r_{i+1} - r_i$) between the two adjacent masks of M_{ri} and M_{ri+1}.
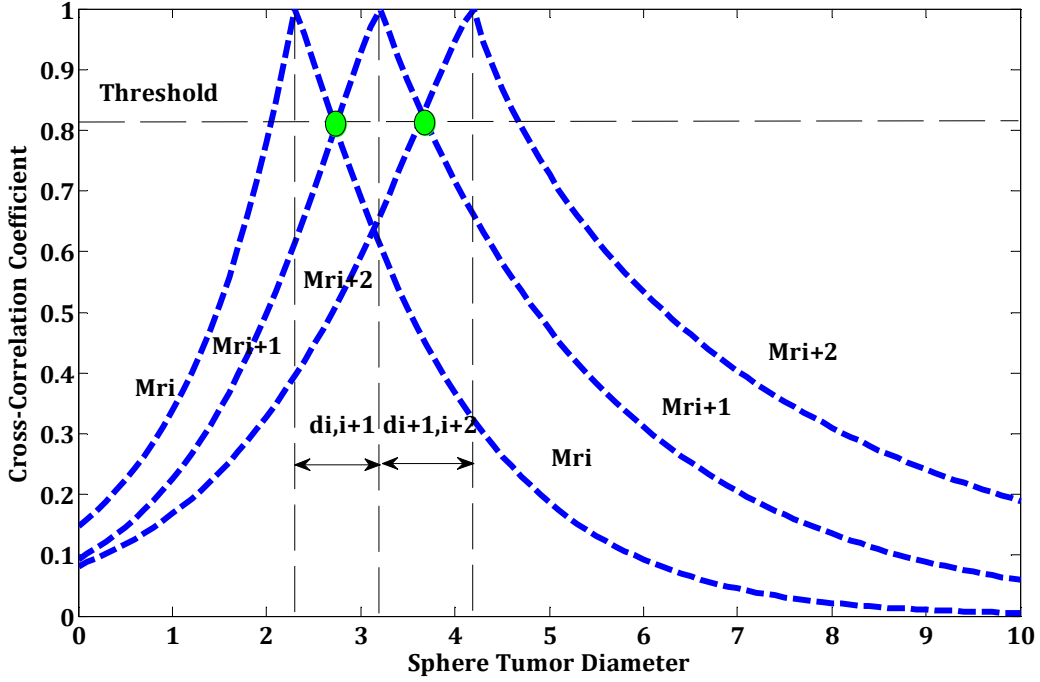
Fig. II.3. A scheme on the design of the masks, $\{M_{ri}\}$, and selection of the cross-correlation coefficient (CCC) threshold, τ, based on Eqs. II.3-7. Dashed curves represent CCCs between the masks and the spherical tumors with different sizes. A threshold chosen at the intercept of the CCC curves of the 1st and 2nd masks (at τ) is warranted to detect all tumors with the volumes between the two masks.

So far, we have not considered shape heterogeneity in our analysis. In fact, the CCC is only sensitive to the number of mis-matched voxels between the mask and the lesion. This means that the shape heterogeneity of a tumor with respect to a sphere can be quantified by the number of mis-matched voxels, and therefore, can be modeled similar to size heterogeneity. A tumor with its shape deviating from a sphere can be localized by the masks designed by Eqs. II.6 and II.7 if the CCC between the tumor and the mask is still above the threshold. For example, in a simple case, two tumors have the same volume and are located between a pair of adjacent masks, but one is a perfect sphere and another one is not. Since the two tumors have the same CCC, they will have the same probability for localization. This puts a limit on shape deviation of a tumor from a sphere. Since the

14

spherical tumor T_k (at the intercept of the two CCC curves in Fig. II.3) has the smallest CCC with either M_{ri} or M_{ri+1}, the number of mis-matched voxels of a non-spherical tumor with one of the masks has to be equal to or smaller than the $T_k's$ in order to be detected by the mask. Thus, $d_{i,i+1}$, the radius difference between the adjacent spherical shell masks limits tolerance of shape variation of a tumor from a sphere. If $d_{i,i+1}$ is set large enough, a set of masks can detect tumors with large shape heterogeneity and result in a high sensitivity for tumor localization. We designed our templates to be able to detect a non-spherical tumor that has the number of mis-matched voxels with the mask which is not greater than one of a sphere with the volume twice of the smallest mask. This is also the reason why we set $a = 2R$ in Eq. II.1 (Fig. II.1B). Note that shape deviation corresponding to the inter-shell of the mask can also be considered in a similar manner.

In summary, if $\{T_s\}$ is a set of tumors with various sizes and shapes, to localize $\{T_s\}$, the first mask is chosen as small as the smallest tumor. The second mask is determined by having the volume of the spherical tumor (T_k) at the intercept of the CCC curves of the two masks, twice as the first mask. The intercept of the two CCC curves also determines the threshold, τ. The remaining masks will be selected based on Eq. II.7.

II.B.2.ii Design of $\{M_{ri}\}$ and τ in a Digital Space

In order to find appropriate $\{M_{ri}\}$ and τ in the discrete form, a digital phantom comprised of different spheres with radii ranging from 1 to 6.2 mm and a step size of 0.1 is implemented (It will be discussed later in this chapter that we are only interested in localizing lesions with a diameter of < 5mm, and hence large spheres are not included in the phantom). We then follow the procedure described previously to find out which digital masks meet the

conditions given in Eqs. II.3-7. The smallest feasible digital mask M_1 is $r_1 = 1$. The radius of T_k is 1.26. To identify M_2, we first compute the CCCs of the digital phantom with M_1 and with all candidates (digitally resolvable) of M_{r2} ($\forall$ $r_2 > 1$). Next, we approximate the CCCs ($Corr_{r_1,Right}(.)$ and $Corr_{r_2,Left}(.)$) by an exponential function to find r_2 by having the radius of T_k close to 1.26 (Fig. II.4). As a result, we identify $r_2 = 1.5$ with $\tau = 0.8$ and $r_k = 1.25$ (radius of T_k). This procedure is repeated to find the remaining masks as $r = \{1, 1.5, 2.3, 3.2, 4.2...\}$. However, due to digitization, not all the remaining CCC thresholds were 0.8. Hencse, they are chosen slightly below 0.8 to retain maximum sensitivity, e.g., 0.74 for $M_{1.5}$, $M_{2.3}$ and $M_{3.2}$.
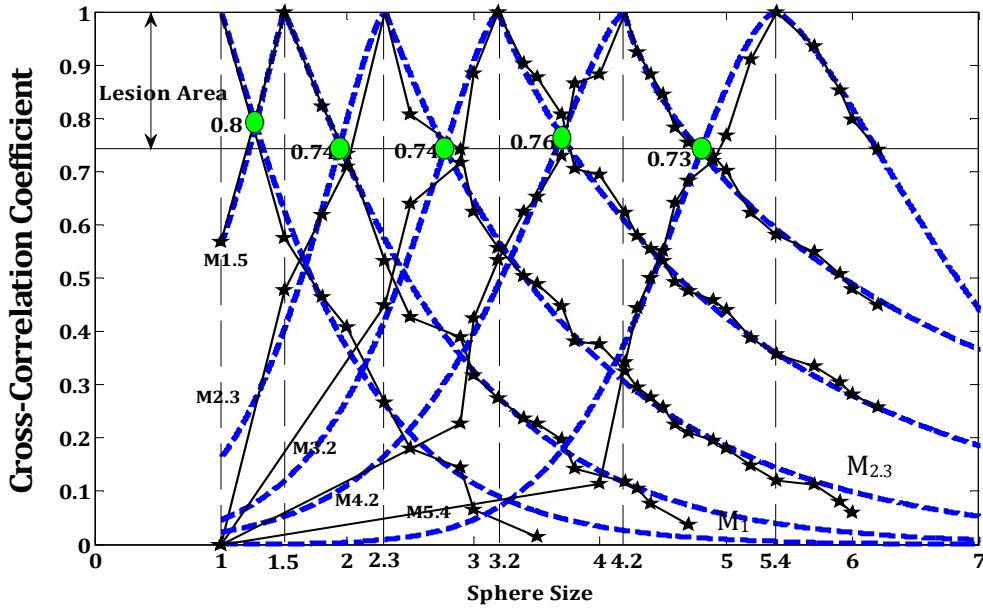
Fig. II.4. The optimal set of digital masks, $\{M_{ri}\}$ with $r = \{1, 1.5, 2.3, 3.2, 4.2,$ and $5.4 ...\}$, and the cross-correlation coefficient thresholds, τ. In the digital space, the thresholds are approximately 0.74. Solid line: regression fitting line; Solid symbols: data points of cross correlation.

II.B.2.iii Design of {M$_{ri}$} and τ with Intensity Variation

To consider effects of intensity variation and noise within a tumor and its surrounding background on the cross-correlation coefficients, we define a contrast to intensity variation ratio (CIVR) as following:

$$CIVR = \frac{|\mu_t - \mu_b|}{\sqrt{\frac{1}{(N_B + N_T)}\left[N_T\sigma_t^2 + N_B \cdot \sigma_b^2\right]}}$$
(Equation II.8)

where N is the number of voxels, μ and σ are the mean and the standard deviation of signal intensities, respectively, and subscripts t and b denote tumor and background, respectively. For a zero-mean mask given in Eq. II.1, we have:

$$\frac{N_T - \beta \cdot N_B}{N_T + N_B} = 0 \Rightarrow \beta = \frac{N_T}{N_B}$$

$$\overline{w} = \frac{N_T\mu_t + N_B\mu_b}{N_T + N_B}$$
(Equation II.9)

Using Eqs. II.8 and II.9, we rewrite Eq. II.2 as:

$$Corr_{M_r}(V_{MR}) = \frac{Corr_{M_r,V_{MR}}(WOIV)}{\sqrt{1 + \frac{(N_B + N_T)^2}{N_B N_T} \times \frac{1}{CIVR^2}}}$$
(Equation II.10)

$$Corr_{M_r,V_{MR}}(WOIV) = \frac{1}{\sigma_M}\sqrt{\frac{N_T}{N_B}}$$

where σ_M is the standard deviation of the mask, and $Corr_{M_r,V_{MR}}(WOIV)$ denotes the CCC between M_r and V_{MR} without intensity variations within the tumor and in the background ($CIVR = \infty$). Eq. II.10 shows that the CCC decreases with CIVR from the value without any intensity variation. We further investigated the effect of intensity variation on choosing the threshold of CCC by simulation, in which we add Gaussian noise with different standard deviations (δ) to the digital phantom described in Section 2.1.2.b, and recalculate $Corr_{r_i,Right}(.)$ and $Corr_{r_i,Left}(.)$ and the thresholds for the masks. As expected, the CCC thresholds depend upon δ (or CIVR), which will be used to train the system.

17

II.B.3 Nodule Localization

To localize tumors, after computing the CCCs of MRI volumes with a mask M_{ri} at resolution r_i, we identify all voxels above a threshold. Then, we group all connected (26-adjacency) voxels by growing regions [39], and pick the voxel with a maximum CCC from each connected group as the center of the candidate lesion at the r_ith resolution, $C_{ri,k}$.

To refine the definition of the candidate lesion, the k-Means method [39] is applied to classify the voxels within a cubic volume with a size of $2a$ (same size of the mask) and a center at $C_{ri,k}$ (the center of the candidate lesion) of MRI to bright and dark voxels. The candidate lesion is defined by all bright voxels connected to the center. The bright voxels disconnected from the candidate lesion center are discarded.

II.B.4 False Positives Reduction

As shown in Section 2.1.2.c, noise and intensity variations in both tumor and background affect the CCC values, and thereby the performance of a CAD system (causing a large number of false positives). In the following sections, we developed strategies to improve the CCCs and reduce the number of false positives.

II.B.4.i Nodule Enhancement

The intensity variations of a nodule and its surroundings are comprised of three main components: 1) image noise, 2) intra-tissue inhomogeneity, and 3) intensity variation of different tissues in the background. For a small lesion, image noise and intra-tissue inhomogeneity are the dominant components. However, as the mask size increases, tissue heterogeneity in the background surrounding the tumor becomes a major factor. In this

work, we focused our attention particularly on small lesions, and hence propose a method to enhance the CIVR of the small lesions in order to employ a higher CCC threshold and reduce false positives.

To increase the contrast of a lesion, histogram equalization [40] Eq. (11), is used to transform bright voxels of MR images to the upper extreme of a new gray scale as I_{he}:

$$I_{he}(k) = \sum_{i=0}^{k} P(i), \quad k = 0, \frac{L}{M}, \frac{2L}{M}, ..., L \qquad \textbf{(Equation II.11)}$$

where $P(i)$ is the occurrence frequency of the ith intensity scale in the original image, L is the number of gray scales in the original volume, and M is a quantization factor and determines the number of gray levels in I_{he}. Then, I_{he} is normalized to have a value of I'_{he} between 0 and Max (I_{he}):

$$I'_{he} = \frac{I_{he} - Min(I_{he})}{Max(I_{he}) - Min(I_{he})} \cdot Max(I_{he}) \qquad \textbf{(Equation II.12)}$$

Assuming tumors are in the upper portion of I'_{he}, power transformation is employed to further enhance the nodule and suppress the dark background:

$$I_{he,pt} = I'^{\lambda}_{he} \qquad \textbf{(Equation II.13)}$$

where $I_{he,pt}$ represents the gray scale after applying histogram equalization followed by power transformation, and λ is an exponent. Fig. II.5 illustrates that a large λ enhances the contrast of a nodule in the upper scale of I'_{he} by increasing the intensities in the higher gray scales and decreasing those in the lower ones. In addition, histogram quantization (Eq II.11) decreases the intensity inhomogeneity within a nodule. Combining the two steps, the ratio of the contrast to intensity variation of the nodule is enhanced. Fig. II.5 shows that the intensities in the lower half of the gray scale are suppressed almost entirely by $\lambda > 6$.

19

However, a large λ also increases intensity variations within a nodule, and thereby decreases the CIVR. Hence, λ will be optimized in the training step to balance these two effects.
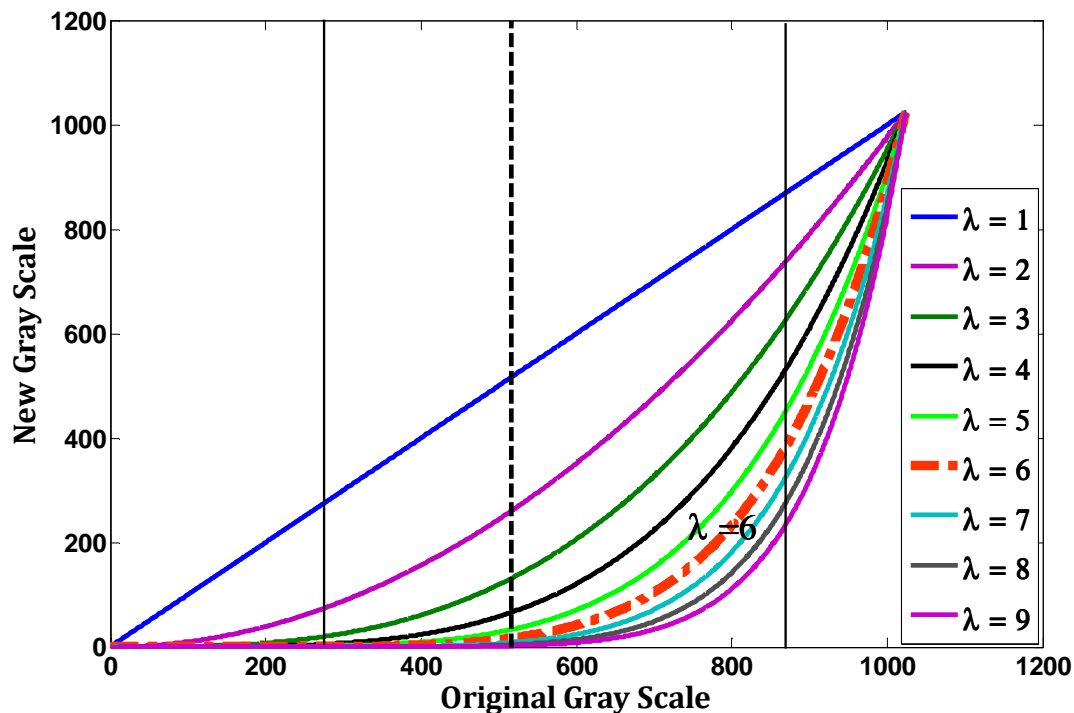
Fig. II.5. The impact of power transform in nodule enhancement. The power transformation, λ, increases the contrast between high and low intensities in I'_{he}. If a nodule is in the upper portion of I'_{he}, the application of power transform enhances the nodule contrast and suppresses its dark surrounding. For $\lambda > 6$, all intensities lower than a half of the maximum are almost entirely suppressed in $I_{he,pt}$. Here, I'_{he} has 1024 gray scales.

II.B.4.ii Size Criterion

While we develop strategies to increase the sensitivity of the CAD system, we also need to implement methods to reduce the number of false positives. Brain metastatic tumors are usually isolated lesions within the brain, while other detected nodules are typically part of an extended structure, e. g., contrast-enhanced blood vessels detected by low resolution masks of $r_i = 1$ and 1.5, where the size of the cross-section of the small blood

vessel is comparable to the mask. Hence, we further grow the initially detected segment by connecting similar voxels in the volume of $(25 * 2r_i)^3$ beyond the initial VOI by using descriptive statistics (maximum and minimum) of the initial connected voxels. The final size of the segment can differentiate an isolated lesion from an extended and non-tumor like structure. Hence we reject any nodule with a volume eight times ($R_n = 2R$) greater than the volume of the applied mask.

II.B.4.iii Sphere Index

To further reduce the number of false positives, e.g., a segment of blood vessel, we compute a sphere index of the detected nodule as the second false positive rejection criterion, which is based upon the fact that metastatic lesions are usually spherical-like instead of cylindrical-like. To do so, we compute eigenvalues (e_1, e_2, and e_3) of a covariance matrix of a matrix whose columns are comprised of x, y and z coordinates of the nodule voxels. For each nodule, the eigenvalues were normalized to max (e_1, e_2, e_3) = 1. The sphere index, *SI*, is defined as the geometrical mean of the eigenvalues as following:

$$SI = \sqrt[3]{e_1 e_2 e_3}$$ **(Equation II.14)**

For a spherical object, $e_1=e_2=e_3=1$ and hence *SI* = 1. As an object deviates from a sphere, SI decreases from 1. To find an appropriate threshold for *SI*, we use the descriptive statistics of the lesions in the training step, and define the threshold as: $\tau_{SI} = \mu_{SI} - 2.5\sigma_{SI}$, where μ_{SI} and σ_{SI} are the mean and the standard deviation of all the metastatic lesions, respectively.

II.B.4.iv Brightness Criterion

As mentioned in Section 2.2.1, tumors are transferred to the upper extreme of I'_{he} by the histogram equalization. This enables us to further reject the false positives using a brightness index. We exclude any detected nodule with a brightness index ($\frac{\mu_k}{Max(I'_{he})}$) less than 0.5, where μ_k denotes the mean intensity of the nodule in I'_{he}.

II.B.5 Methods of Training and Evaluation

II.B.5.i Human Subjects

Thirty one patients diagnosed with brain metastases were enrolled in a prospective MRI study. For each patient, 3D post-Gd-DTPA volumetric T1-W MRI with a voxel size of 0.9375 x 0.9375 x 1 (mm³) was acquired prior to radiation therapy using a Philips 3T MR scanner. Of the 31 patients, two were excluded from this study since the MR images were corrupted by motion artifact. From the remaining 29 patients, we defined the first 9 patients as a training set and the remaining 20 patients in the testing set. There were four patients, two in the training dataset and two in the testing dataset, who had more than 30 lesions each. As a total, there were 1279 and 2753 slices in the training and testing datasets, respectively.

II.B.5.ii Training and Optimization of the CAD System

To train and optimize our CAD system, we identified all the lesions in the initial training dataset. To do so, we put together the results of the initial neuro-radiologist as well as a separate retrospective reading by a second highly trained neuro-radiologist. We also ran the proposed CAD system in an over-sensitive mode on the training dataset by using a

fairly low cross correlation coefficient threshold (≈ 0.5) at each resolution in order to detect as many lesions as possible. The second neuro-radiologist had two analyses: First, the pre-RT MR images were analyzed without referring to the additional CAD results or further clinical follow ups and imaging studies; and the second analysis of the MRI images with all available clinical information as well as the CAD results. The first analysis was used to evaluate his performance, but the second analysis was aimed to detect all the lesions in order to train and further optimize the CAD system. In order to document what size and type of lesions that are likely missed by highly trained neuro-radiologists and our CAD system, we divided the lesions into three categories: solid mass without necrosis (regular), lesion with necrotic core (hole), and one located near the edge or the surface of the brain (edge). Table II.1 summaries the number of the lesions found in each of the categories in the training dataset.

Table II.1. Numbers and characteristics of metastatic lesions in the training data

< 5mm				< 8mm				All Lesions
Total	R	H	E	Total	R	H	E	All types
60	50	3	9	78	57	7	17	106

R, H, and E denote regular, hole and edge lesions.

To obtain the statistics of the lesions likely missed by the neuro-radiologists, we put together the screening results of the initial diagnosis by the first neuro-radiologist as well as the first independent reading of the second neuro-radiologist. Since the precise location of each of lesions for the two patients with 30 lesions or more were not available for the initial diagnosis, we excluded the two patients from this analysis. In the initial diagnosis,

when a patient has a large number of lesions, the locations of the lesions become irrelevant for treatment, and are usually not reported. Therefore, we cannot use the initial diagnosis of the two patients to find the sizes of the lesions likely missed in clinical screening, and excluded the two patients from the analysis.

To optimize the proposed CAD system, we ran the system on the training dataset at resolutions of r = 1, 1.5, 2.3, and 3.2 with combinations of all thresholds/parameters (including varying λ from 6 to 9 and τ from 0.5 to 0.75). Then, we generated free-response receiver operating characteristic (FROC) [41] curves to determine the optimal set of parameters for the CAD system, in which a false positive rate was calculated as a ratio of the total of false positives to the number of slices.

To study the effect of each of the proposed false positive rejection criteria, we compared the FROC curves resulted without applying any false positive rejection criteria with the ones by sequentially adding the criteria: (1) the nodule enhancement strategy, (2) the size criterion, 3) the sphere criterion, and (4) the brightness criterion. In this chapter, we mainly focus on rejecting intra-cranial false positives, since the extra-cranial false positives can be rejected by other methods, e.g., a skull stripping technique [42], which can be implemented, but is currently beyond the scope of this study.

II.B.5.iii Testing of the CAD system

To evaluate the proposed system, we ran the CAD system on the testing dataset by using the optimal set of the parameters determined from the training dataset. Similar to what was done in the training step, the second neuro-radiologist read the MR images twice: once without and then with all available reference materials. Finally, we put together the

results of the initial diagnosis and the first independent reading of the second radiologist to obtain the statistics of the lesions likely missed by the neuro-radiologists. The results of the second reading of the second neuro-radiologist were used as a reference to evaluate the performance of the CAD system. Table II.2 summarizes the categories of the lesions in the testing dataset.

Table II.2. Numbers and characteristics of metastatic lesions in the testing data

< 5mm				< 8mm				All lesions
Total	R	H	E	Total	R	H	E	All types
186	157	2	28	250	199	11	44	313

R, H, and E denote regular, hole and edge lesions.

II.C Experimental Results

II.C.1 Training and Optimization of the CAD system

II.C.1.i Size of Lesions Likely Missed by Neuro-Radiologist

Table II.3 shows the screening results of the initial diagnosis and the first reading of the second radiologist on the training data. Neither of the two neuro-radiologists missed any lesions if the diameter of the lesion was > 5mm. However, the lesion detection rates of the initial diagnosis decreased from 93% to 81% and to 73% for lesion diameters $\geq$ 4 mm, $\geq$ 3 mm, and to $\geq$ 2 mm, respectively. The results of the first independent reading of the second radiologist were similar to the initial diagnosis. If only considering the lesions with diameters less than 5 mm (27 lesions), the two radiologists detected 60% and 66% of the

lesions. Based upon these observations, we trained our proposed CAD system to detect lesions smaller than 5 mm by using the masks with resolutions r= 1, 1.5, 2.3 and 3.2.

Table II.3. Numbers of the lesions in the training data detected by radiologists

Method	≥ 2mm	≥ 3mm	≥ 4mm	≥ 5mm	≥ 8mm
1st Radiologist	30/41 (73%)	22/27 (81%)	15/16 (93%)	14/14 (100%)	10/10 (100%)
2nd Radiologist	32/41 (78%)	24/27 (88%)	15/16 (93%)	14/14 (100%)	10/10 (100%)

No lesions with diameter greater than 5mm were missed by the radiologists. Considering only the lesions smaller than 5mm in diameter, 60% (16/27) and 66% (18/27) are detected by the two radiologists. Seven patients were included.

II.C.1.ii Optimal Parameters of the CAD system

To optimize the proposed CAD system, the FROC curves of the detected lesions from the training dataset were generated by varying the exponent of the power transformation of λ = 6, 6.5, 7, 7.5, 8, 8.5 and 9 and the threshold of CCC from 0.5 to 0.75 (Fig. II.6). As seen, for a sensitivity of 96.7% (or 90%), the lowest intra-cranial false positive rate (IC-FPR) is 0.0211 (27/1279), or 0.006 (8/1279), which is obtained by using λ = 8.5, the CCC threshold corresponding to CIVR = 5.12 (or 5.85), and the sphere index (SI) > 0.24. Other values of λ produced worse false positive rates when the sensitivity was set greater than 90%. The areas under the FROC curves (AUC) for the FPRs ranged from 0.000 to 0.029 (the maximum shown in Fig. II.6) are 0.818, 0.827, 0.852, 0.850, 0.848, 0.884, and 0.877 for λ = 6, 6.5, 7, 7.5, 8, 8.5 and 9, respectively. The AUC also indicates that λ = 8.5 performs the best.
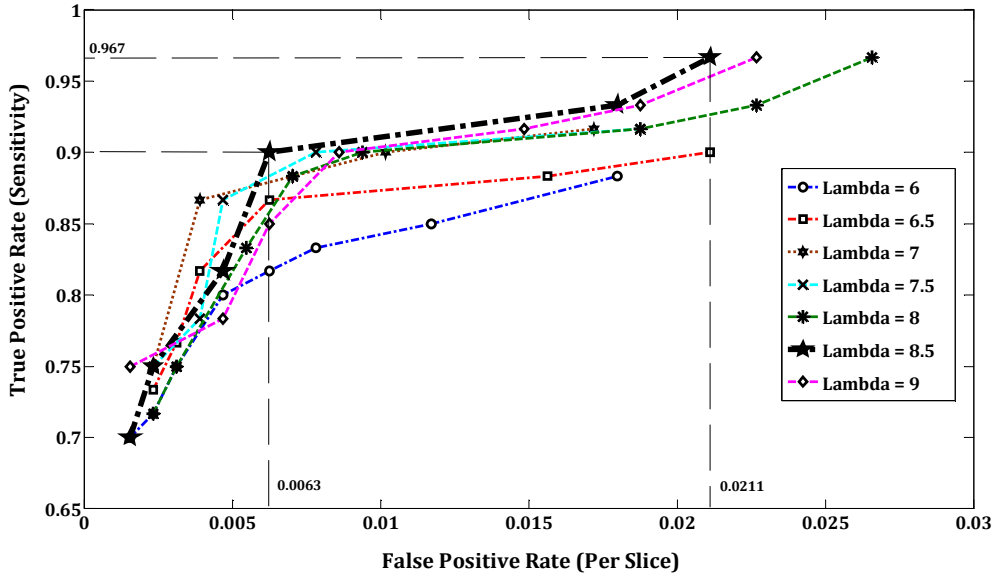
Fig. II.6. FROC Curves of the lesions and false positives detected by our proposed CAD system in screening of the training dataset. Each of the curves was generated with different values of λ and CCC thresholds. Using λ = 8.5 yields a sensitivity of 90% and a false positive rate of 0.006 (8/1279), or a sensitivity of 96.7% and a false positive rate of 0.021 (27 / 1279). The CCC thresholds were set corresponding to the CIVR = 5.12, and sphere index (*SI*) was > 0.24.

II.C.2 Effect of Nodule Enhancement

Next, we compared the FROC curves obtained from the training dataset with and without the nodule enhancement strategy and without applying any false positive rejection criteria. Fig. II.7 shows that our nodule enhancement strategy (with the optimal λ = 8.5) improves both sensitivity and specificity significantly. For the IC-FPR of 0.0758, the sensitivity improved from 81% to 98.3%. However, without using nodule enhancement, the FROC curve reaches a plateau in sensitivity, indicating that sensitivity cannot be improved more than 0.82 even when we increase the false positive rate. For the FPRs ranged from 0.000 to 0.029, the AUCs are 0.681, 0.784 and 0.884 for the lesion detections without module enhancement and any false positive rejections, with module enhancement but without false positive rejections, and with all false positive rejection criteria,

respectively, in Fig. II.7. Fig. II.8 shows examples of intensity histograms of a slice of T1-weighted MRI, and intensity variations within and around a lesion with and without applying the nodule enhancement strategy. Note that the histogram equalization transfers gray scales of the nodule to the upper extreme of the image histogram (Figs. II.8B and II.8F), and thereby the nodule is bright as well as the vessel and skin are (Figs. II.8A and II.8E). The histogram equalization also reduces the noise (standard deviation) within the nodule due to quantization (Figs. II.8C and II.8G), and in the surrounding background. The power transformation further increases the contrast of the nodule with respect to the background, and suppresses the intensity variation in the background (Figs. II.8L and II.8H). As a result, the *CIVR* of the nodule is improved from 5.26 (in the original image) to 13.2 (in the $I_{he,pt}$ with $\lambda = 6.5$), which enables the selection of a higher threshold of CCC and thereby to have a lower false positive rate. However, a further increase in λ increases false positives and deteriorates the performance of the system. The optimal λ (=8.5) has to be determined from the FROC curves as previously shown in Fig. II.6.
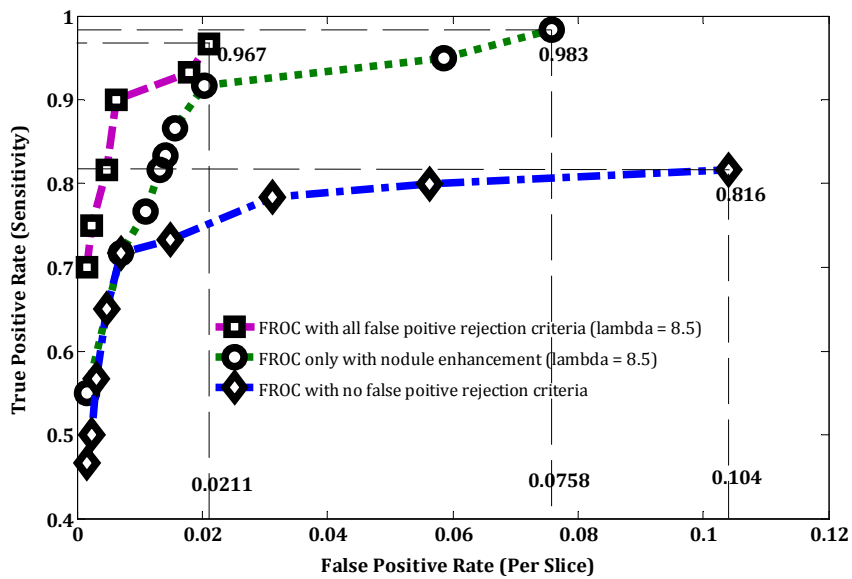
Fig. II.7. The effect of nodule enhancement on the FROC curves.

28

(A)	(B)	(C)	(D)
(E)	(F)	(G)	(H)
(I)	(J)	(K)	(L)
MR Slice	**Slice Histogram**	**Intensity Variation within Tumor**	**Intensity Variation around Tumor**
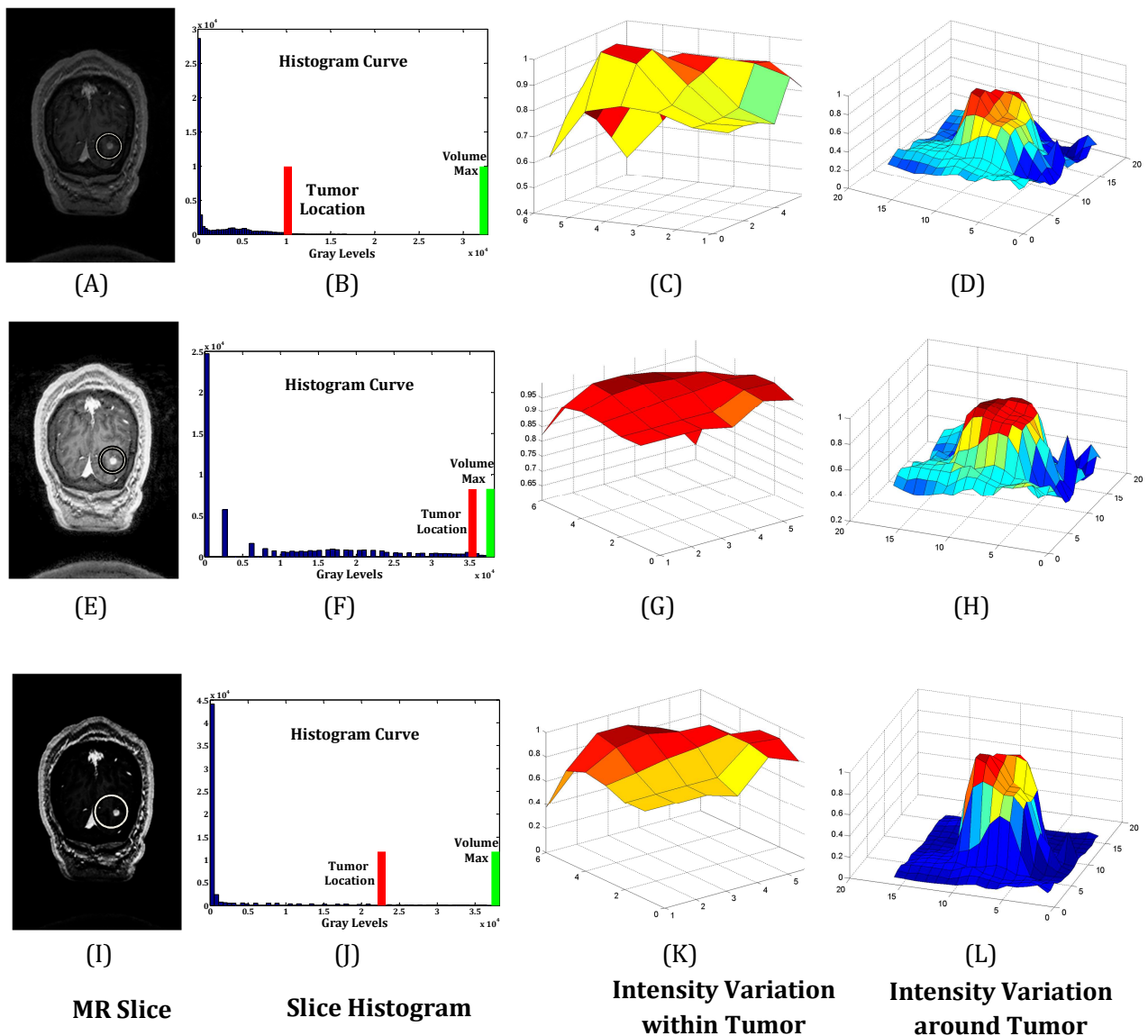
Fig. II.8. An example showing the different stages of applying the nodule enhancement strategy to a typical contrast-enhanced lesion. The effects of the nodule enhancement on the post-Gd T1-W MRI (left), intensity histogram (second left), intensity variation within the lesion (second right) and intensity variation in the surrounding background (right) of the lesion. Top row: the original data; Middle row: the data after applying the histogram equalization; Bottom row: the data after applying the power transformation of $\lambda = 6.5$.

II.C.3 False Positive Rejection

Table II.4 shows the effects of false positive rejection criteria on improvement in specificity of the proposed system. For the 60 lesions with a diameter < 5 mm on 1279

slices in the training dataset, using the nodule enhancement only, intra-cranial false positives were 97, decreased to 48 after applying the size criterion, to 28 after applying the size and sphere criteria, and to 27 when applying the size, shape and brightness criteria. The size criterion and the sphere index are effective for rejecting both the intra- and extra-cranial false positives, while brightness criterion is useful for rejecting the extra-cranial false positives. Note that one lesion was rejected mistakenly by the size criterion due to the fact that the lesion was connected to a blood vessel.

Table II.4. Effects of false positive rejection criteria in the training data

NE			NE & Size			NE, Size & SI			NE, Size, SI & B			NE & B		
Miss	TP	FP	Miss	TP	FP	Miss	TP	FP	Miss	TP	FP	Miss	TP	FP
1	59	97(610)	2	58	48(211)	2	58	28(171)	2	58	27(106)	1	59	85(320)

NE: nodule enhancement; Size: size criterion; SI: sphere index; B: brightness criterion; TP: true positive; FP: false positive. The intra- and extra-cranial FPs are given outside and inside the parentheses, respectively.

II.C.4 Testing of the CAD system

II.C.4.i Size of Lesions Likely Missed by Neuro-Radiologists

The screening results of the testing dataset from the initial diagnosis and the first independent reading of the second radiologist was similar to what was observed in the training dataset: the lesions with a diameter < 5 mm had a higher frequency of being missed (Table II.5). Again, we excluded the 2 patients with 30 lesions or more from this analysis due to lack of precise location of each of these lesions. Again if only considering the lesions with diameter less than 5 mm (30 lesions), the two neuro-radiologists detected 70% and 80% of the lesions.

Table II. 5. Numbers of the lesions in the testing data detected by radiologists

Method	≥ 2mm	≥ 3mm	≥ 4mm	≥ 5mm	≥ 8mm
1st Radiologist	66/75 (88%)	56/60 (93%)	48/49 (98%)	45/45 (100%)	29/29 (100%)
2nd Radiologist	69/75 (92%)	58/60 (96%)	49/49 (100%)	45/45 (100%)	29/29 (100%)

No lesions with diameter greater than 5mm were missed by the radiologists. Considering only the lesions smaller than 5mm in diameter, 70% (21/30) and 80% (24/30) of the lesions are detected by the two radiologists. Eighteen patients were included.

II.C.4.ii Testing of the CAD System

Using the optimal set of parameters obtained in the training step, a sensitivity of 93.5% (174/186) was achieved with an IC-FPR of 0.024 (66/2753) in the testing data (186 lesions with a diameter < 5 mm from 20 patients). Fig. II.9 shows examples of the lesions (diameters of 2.2, 3.4 and 4.5) missed by the radiologists but detected by the proposed CAD system.

II.C.5 Sources of False Negatives

The lesions missed by our proposed system can be divided into three main categories: 1) lesions with low contrast to intensity variation, 2) lesions attached to a structure and rejected after applying the size criterion, and 3) lesions near the edge of the brain surface. Fig. II.10 shows examples from each category. Table II.6 shows the number of lesions missed in each category. Of the 186 tested lesions, six lesions having a low contrast to intensity variation ratio (3.8%), 5 lesions attached to a blood vessel (3.1%), and 1 near the edge of the brain surface (3.5%) was missed by our CAD system. Also, all of the five missed lesions in the second category were at the midline of the brain (see the middle

31

panel of Fig. 10), where blood vessels have a higher spatial density. Note that no lesion with necrotic core was missed by our proposed approach.

Table II.6. Lesions missed by our proposed system

Dataset	Regular		Hole	Edge	Total
	Low CIVR	Attached to an Object			
Training	0 / 50 = 0%	1 / 50 = 2%	0%	1/9 = 11%	2 / 60 = 3.3%
Testing	6 / 157 = 3.8%	5 / 157 = 3.1%	0%	1/28 = 3.5%	12 / 186 = 6.4%
Total	6 / 207 = 2.9%	6 / 207 = 2.9%	0%	2 / 37 = 5.4%	14 / 246 = 5.6%
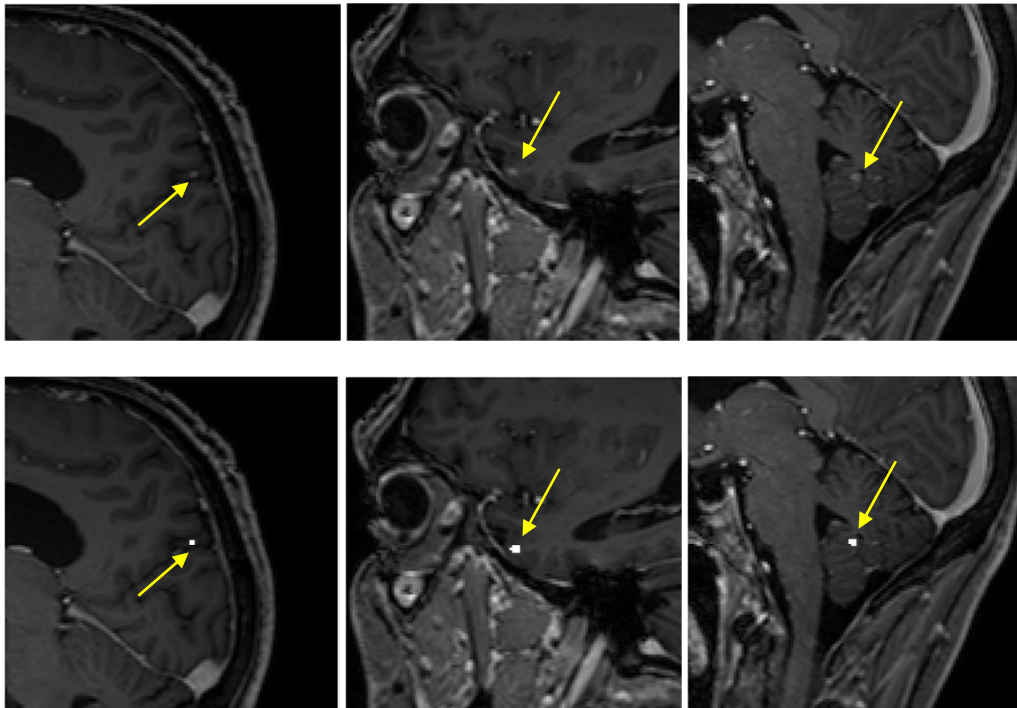
Fig. II.9. Three examples of lesions missed by the radiologists and detected by our proposed CAD system. The lesions diameters are 2.15, 3.37, and 4.51 from left to right. Note that the blood vessels are rejected as a false positive in these images. Top row: the original images; Bottom row: the segmentation map.
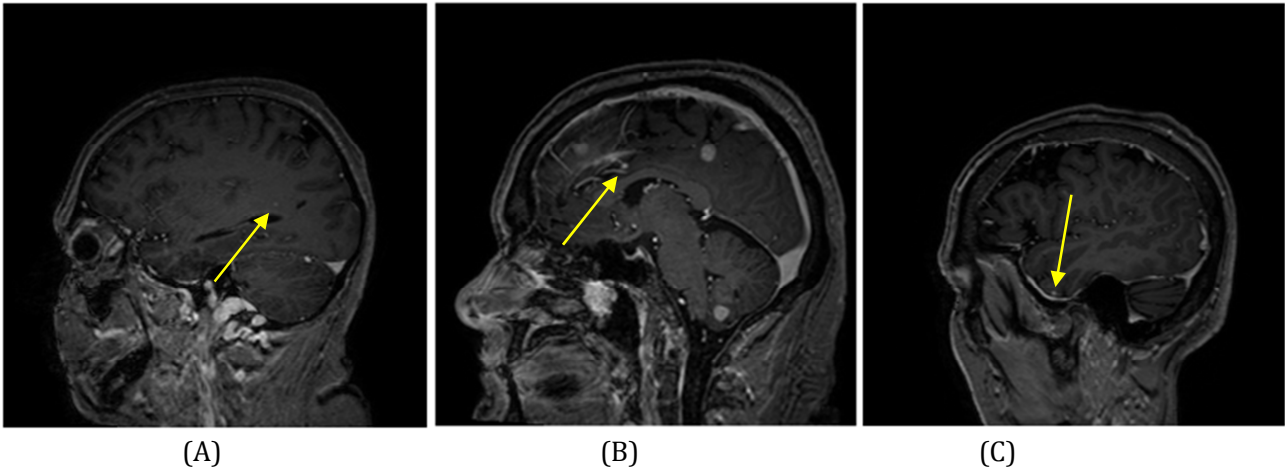
Fig. II.10. Examples of the three types of lesions missed by our proposed CAD system: Left: a lesion with a low contrast to intensity variation ratio; Middle: a lesion attached to a small blood vessel in the midline of the brain; Left: a lesion near the edge and attaching in some parts to the brain surface.

II.D Discussion

In this chapter, a computer-aided detection system has been developed and evaluated for automatic detection and discrimination of small brain metastases in post-Gd T1-weighted MRI, which have a higher frequency of being missed in routine radiological diagnosis. In the development of the system, first we designed a set of multi-resolutions of 3D spherical shell masks, which mimic a bright tumor with or without necrotic core and on a dark background, to localize metastatic lesions by cross-correlation with MR volumes. The analytic and simulation investigations were performed to study the effects of size and shape heterogeneity as well as the intensity variation within a tumor and the surrounding background in order to optimize the template design. Secondly, we developed strategies to improve sensitivity and specificity of the CAD system by using the nodule enhancement strategy to increase the contrast to intensity variation ratio of the lesion and the

background, and by using a set of rule-based false positive rejection criteria based upon the size, shape and brightness of the metastatic lesions. Overall, we achieved 93.4% sensitivity and 0.024 intra-cranial FPR for detecting the brain metastases with a size less than 5 mm, which is 10 times less than the intra-cranial FPR of a previous study [37]. This CAD system has the potential to improve lesion detection especially in lesions less than 5 mm and therefore may aid in the physician's decision-making for selecting appropriate treatment strategy.

Selecting an optimal set of mask sizes and the cross-correlation threshold depend on three major factors: 1) nodule size, 2) nodule shape, and 3) the intensity variation within the tumor and the background. We showed that two consecutive masks can localize all spherical tumors with volumes between the two masks if the cross-correlation coefficient threshold is selected at the intercept of the two cross-correlation curves. We also showed that the shape heterogeneity of the tumors can be modeled similar to size heterogeneity. Hence, a nodule can be localized if its shape deviation from a sphere does not exceed the maximum tolerable size variation, which is determined by the radius difference between the two consecutive masks. However, if the radius difference is too large, the masks could be over-sensitive to the nodules with a large range of shape variations, resulting in an increase in false positives. Furthermore, our analysis (Fig. II.4) shows that it is not necessary to evenly space the masks as stated in a previous study [32]. In fact, evenly spaced masks may not increase sensitivity significantly but definitely increase computation time and possibly false positives. In addition, the data in Tables II.1 and II.2 indicate that the majority of the small lesions have no necrotic core, and thus a solid spherical template seems to be a choice for detecting the small lesions. While a spherical shell template,

34

excluding the voxels in the center from analysis, can detect both solid and necrotic lesions, a solid template can result in some non-matching voxels in the center of a lesion with necrotic core. When using a solid template for detecting both solid and necrotic lesions, we need to low the threshold to reach the maximum sensitivity, which results in more false positives than using a spherical shell template (data not shown).

In our CAD system, we implemented several strategies to reduce false positives. Brain metastases are often seen as isolated masses, while other detected nodules are typically be part of the other structures, e. g., blood vessels. Segments of small blood vessels have a high probability of being detected by the masks. In the previous study [37], of the 16 lesions having a diameter < 5 mm, fourteen lesions were detected, but the false positive rate is as high as 0.22, in which the majority of them are blood vessels. The detected vessel segments usually belong to a large vascular tree. Therefore, we grew the detected segment beyond the initial VOI by connecting more similar voxels. Hypothetically, the extended structure is unlikely to be a tumor, and can be rejected based on size criterion. Using the size criterion and the sphere index, we are able to reject 71% of the intra-cranial false positives and 72% of the extra-cranial false positives in the training dataset. In the training processing, we learned that there are some lesions, which have a low contrast with respect to its surrounding background and a large intensity variation, and thus have a greater probability of being missed by a CAD system. Our proposed nodule enhancement strategy improves the low nodule contrast and reduces the intensity variation, and enables us to gain both sensitivity and specificity (Fig. II.7). Overall, we are able to reduce intra-cranial FPR to 0.024, which is a major improvement compared to the previous work. Further reduction of the extra-cranial false positives can be better achieved by using a skull

stripping technique [42], which is not the aim of this study but can be incorporated into a final CAD package.

In this chapter, we analyzed what types of lesions are missed by our CAD system (Table II.6). The main reasons are typically due to the attachment to another structure, especially in the midline of the brain, or have a low contrast to intensity variation ratio (CIVR). In the former case, segmenting vessels from tissues in the midline could be helpful, e.g., using publically-available software of SPM [43]. One easy solution for the latter problem is to decrease the cross-correlation threshold, but this may increase the false positive rate substantially. For example, the lesion shown in Fig. II.10A can be detected by decreasing the cross-correlation threshold at the cost of increasing the false positive rate to 0.1 (that is 5 times greater than we have now). Although our proposed nodule enhancement strategy improves both sensitivity and specificity of the proposed CAD system, developing a technique to locally adapt the CIVR could further improve the performance of the CAD system. A strategy to deal with a lesion near a vessel could also improve the CAD system.

II.E Conclusion

The CAD system described in this chapter is especially designed to localize small brain metastatic lesions, given that the small lesions have a higher probability of being missed by the clinicians. Our proposed CAD system has high sensitivity and fairly low FPR for detection of the small lesions in MRI of the brain compared to previous ones and neuroradiologists. Also, this work can be further extended to localize larger lesions as well. The technical issues as well as clinical needs for detection and segmentation of large

lesions, in a certain extent, differ from the small ones, which require different emphases in the design of the CAD system. For large lesions, segmentation is more clinically interesting than detection. The potential of this method to assist clinical-decision making warrants further evaluation and improvements. A clinical study evaluating the impact of our CAD system on overall diagnosis is ongoing.

<div align="center">**Chapter III**</div>

Physiological imaging-defined response-driven subvolumes of a tumor

III.A Introduction

The ability of intensity-modulated radiotherapy (IMRT) to deliver high-precision nonuniform dose patterns has raised a question on how to paint doses in the radiation target volume to improve the therapeutic ratio and outcome [44]. Conventional IMRT optimizes and delivers a treatment plan within a target volume primarily based upon anatomic images of computed tomography (CT) and/or magnetic resonance imaging (MRI). Geometrically conforming high doses within the target volume by IMRT can reduce dose-spread into normal tissue and organs at risk. However, target volume delineation based upon anatomic information is increasingly becoming a major limitation. Also, considering spatially-heterogeneous biological properties of a tumor, a uniform dose distribution within a target volume might not lead to an optimal treatment outcome. Hence, dose painting/sculpting based on the biological target has the potential to improve local control or even outcome [45].

The biological target can be defined by *in vivo* functional, metabolic and molecular imaging [44]. It has been suggested that a tumor biological target volume could consist of multiple biological target subvolumes that are imaged by multiple functional imaging

examinations, each having a prognostic or predictive value for radiation response and outcome. It has been hypothesized that dose painting of the biological target subvolumes defined this way could lead to a better outcome than distributing a uniform dose within a target volume [44-45]. However, it lacks a robust methodology to delineate the subvolumes of a tumor based upon physiological imaging and to relate them to tumor response to radiotherapy.

In this study, the main goal is to propose an image analysis framework to integrate the physiological and biological information from a variety of functional imaging sources, to delineate the imaging-defined "phenotype" subvolumes of a tumor and to relate them to treatment response and outcome[2]. We applied the proposed strategy to delineate the tumor subvolumes from regional cerebral blood volume (rCBV) and Gd-DTPA transfer constant from blood plasma to tissue (K^{trans}) in patients who had brain metastases and received whole brain radiotherapy (WBRT). We then examined the association of a change in the subvolume of the tumor from pre to during RT with post-RT treatment response.

III.B Materials and Methods

III.B.1 Patient

Twenty patients (11 women and 9 men, ages 41-76 years) diagnosed with brain metastases were enrolled in an institutional review board (IRB)-approved prospective MRI study (Table III.1). The histology included melanoma (11), non-small cell lung cancer (6), renal cell carcinoma (1), breast cancer (1), and head & neck squamous cell carcinoma (1).

---

[2] Farjam et al. Physiological imaging-defined, response-driven subvolumes of a tumor. *International journal of radiation oncology, biology, physics* (in press).

All patients received WBRT with a total dose of 30 Gy in 10 fractions or 37.5 Gy in 15 fractions. Thirteen of the 20 patients received Bortezomib during WBRT as a radiation sensitizer as part of a separate IRB-approved study. If a patient had three brain metastases or fewer, all lesions were included in this analysis. If a patient had more than three lesions, only the three largest lesions were included. If a patient had more than three lesions larger than 1 cm^3, the lesions greater than 1 cm^3 were also included. As a total, 45 lesions with a median volume of 1.65 cm^3 and a range of 0.1-17.6 cm^3 were analyzed.

Table III.1. Patient characteristics information

Pt. No.	Gender/Age (Y)	Histology	No. of lesions	Volume range (cm^3)	Total accumulated dose/Fx (Gy)	Concurrent drug treatment
1	F/54	BC	3	4.23 - 11.78	37.5/2.5	None
2	M/63	RCC	2	13.23 - 14.67	30/3	Bortezomib
3	M/41	M	3	0.150 - 1.24	37.5/2.5	Bortezomib
4	F/60	NSCLC	1	0.518	37.5/2.5	None
5	F/52	M	1	2.74	37.5/2.5	Bortezomib
6	F/45	M	1	2.07	30/3	Bortezomib
7	M/49	M	2	0.171 - 4.09	30/3	Bortezomib
8	F/51	NSCLC	3	0.503 - 4.55	30/3	Bortezomib
9	M/61	M	4	6.64 - 17.67	37.5/2.5	Bortezomib
10	M/52	NSCLC	1	0.479	30/3	None
11	F/55	M	2	0.421 - 0.545	30/3	Bortezomib
12	M/76	M	1	0.680	30/3	Bortezomib
13	F/46	M	6	1.25 - 1.95	30/3	Bortezomib
14	F/57	M	2	0.941 - 1.58	30/3	Bortezomib
15	F/64	NSCLC	1	0.108	37.5/2.5	None
16	M/60	M	3	0.179 - 1.31	30/3	Bortezomib
17	F/74	M	4	0.690 - 5.81	30/3	Bortezomib
18	M/43	H&N SCC	1	0.601	30/3	None
19	M/58	NSCLC	3	2.38 - 10.69	30/3	None
20	F/66	NSCLC	1	0.954	37.5/2.5	None

Abbreviation: Pt. No. = patient number; Y = year; F = female; M = male; BC = breast cancer; RCC = renal cell carcinoma; M = melanoma; NSCLC = non-small cell lung cancer; and H&N SCC = head and neck squamous cell carcinoma.

III.B.2 Imaging and Data Acquisition

All patients had MRI scans on a Philips 3T scanner prior to RT (Pre-RT), 2 weeks after the start of RT (2W), and 1 month after the completion of treatment (1M Post-RT). MRI scans included pre and post Gd-DTPA volumetric T1-weighted images, multi-slice 2D T2-weighted images, and 3D volumetric dynamic contrast enhanced (DCE) T1-weighted images. The 40 image volumes of DCE-images were acquired using a 3D gradient echo sequence in the sagittal plane (a field-of-view of 240 x 240 x 160 (mm), a voxel size of 2 x 2 x 2 (mm^3), a flip angle of 20°, TE/TR of 1.04/5.14 msec and a temporal resolution of 6 sec) with a 0.1 mM/kg Gd-DTPA in an injection rate of 2 s/cc.

III.B.3 Image Analysis

III.B.3.1 Pre-processing

Using an in-house software package, Functional Image Analysis Tool (FIAT) [46], anatomical and DCE-MR images were co-registered to have a voxel size of 0.9375 x 0.9375 x 3 (mm^3). Each lesion of interest was contoured by a physician on the post-Gd T1-weighed images obtained pre-RT, 2W and 1M post-RT. The general Toft model was used to calculate the rCBV and K^{trans} maps as described previously [20].

III.B.3.2 Probability Density Functions of Physiological Parameters

To analyze the rCBV distributions in lesions and subsequent changes during treatment, a probability density function (PDF) of rCBV of a lesion was generated using a non-parametric PDF estimator. The PDF consists of 150 evenly-spaced points to cover the

range of rCBV values for all lesions of interest. A value of PDF at a point x, $H(rCBV = x)$, of a lesion was calculated as:

$$H(rCBV = x) \equiv n_i : x - \varepsilon \leq rCBV_i \leq x + \varepsilon \qquad \textbf{(Equation III.1)}$$

where n_i was the number of voxels within $|rCBV_i - x| < \varepsilon$, and ε was a smooth factor and set as $\varepsilon = \dfrac{\sigma}{4}$ where σ denotes the standard deviation of rCBV distribution in the tumor. After calculating Pre-RT and 2W PDFs for each lesion ($H_{Pre}(x)$ and $H_{2W}(x)$, respectively), $H(x)$ was normalized to have an area under the PDF curve equal to one ($\int H(x)dx = 1$), see Fig. III.1(A). Then, the normalized $H_{Pre}(x)$s of all lesions were summed to generate a pooled PDF (H_p) of brain metastases, in which each lesion contributes equally regardless of its size.
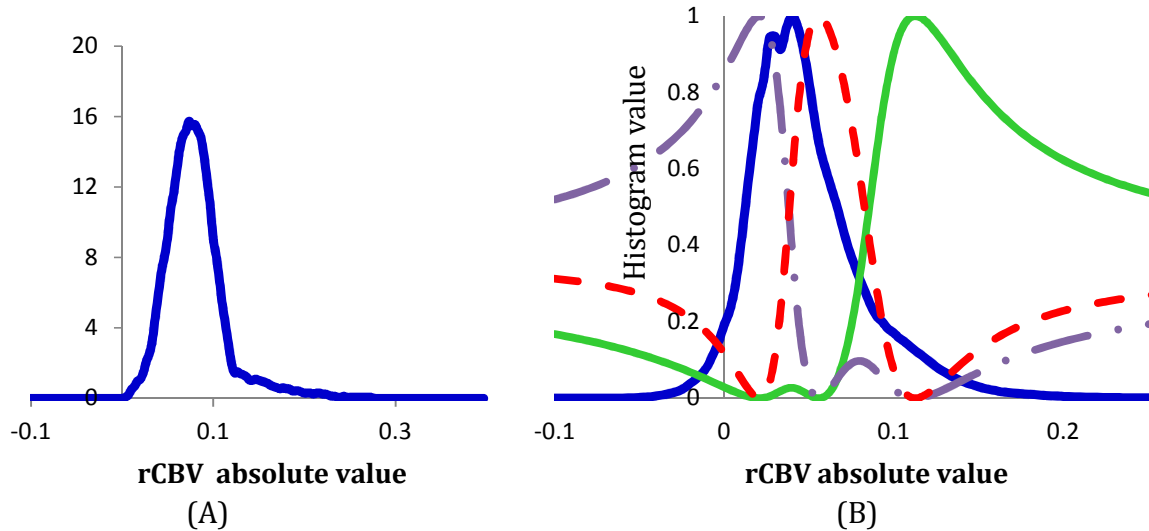
Fig. III.1. Application of FCM in classification of tumor space into classes of low, intermediate and high rCBV. (A) The Pre-RT rCBV histogram of a typical lesion (from patient #13) with a tumor volume of 1.26 cm³. (B) The pooled PDF (blue) of the Pre-RT rCBV from all the lesions and the three probability membership functions determined by FCM clustering. The pooled PDF is partitioned into three classes: low (purple, dot-dashed), intermediate (red, dashed) and high (green, solid) rCBV classes. rCBV: regional cerebral blood volume, PDF: probability density function.

III.B.3.3 Probabilistic Membership Function

Previous studies have suggested that the rCBV distribution of a brain tumor is abnormal compared to normal cerebral tissue, as elevated rCBV in a subvolume of the tumor and low rCBV in another one [47]. A renormalization of tumor vasculature, such as decreasing the elevated rCBV and increasing the low one, could be an indicator of tumor response to treatment [48]. Our goal is to find a set of probability functions that are associated with high, intermediate and low rCBV classes. Hence, the pooled H_p $(rCBV)$ pre-RT is partitioned into three classes using fuzzy-c-means (FCM) clustering analysis by minimizing an objective function J_m:

$$J_m = \sum_{i=1}^{N} \sum_{j=1}^{C} P_j (rCBV_i)^m \left\| rCBV_i - c_j \right\|^2, \ 1 \le m < \infty \qquad \textbf{(Equation III.2)}$$

where c_j is a prototype vector of the jth class, $P_j(rCBV_i)$ is a probabilistic membership of a rCBV value belonging to the jth class, and m is a fuzzy exponent and chosen as 2. The solutions of Eq. III.2 are determined iteratively by:

$$C_j = \frac{\sum_{i=1}^{N} P_j (rCBV_i)^m \cdot rCBV_i}{\sum_{i=1}^{N} P_j (rCBV_i)^m}, \qquad \textbf{(Equation III.3)}$$

$$P_j (rCBV_i) = \frac{1}{\sum_{k=1}^{C} \left[\frac{\left\| rCBV_i - C_j \right\|}{\left\| rCBV_i - C_k \right\|} \right]^{\frac{2}{m-1}}} \qquad \textbf{(Equation III.4)}$$

until reaching stopping criteria. The probabilistic membership function, $P_j(rCBV_i)$, is a new representation of a rCBV value of a tumor voxel (mathematically transfers the data from an image space into a new space) see Fig. III.1(B). Note that the FCM analysis does not classify

a rCBV value into a single class (no hard threshold) rather assigns a probability belonging to a class. A similar computation is applied to K^{trans}.

III.B.3.4 Physiological-parameter Defined Tumor Subvolume

Our primary interest is to test if a change in the subvolume of tumor defined by high, intermediate or low rCBV classes is related to tumor response to therapy. We define a subvolume (SV) of a tumor with low, intermediate or high rCBV using $P_j(rCBV)$, and calculate a percentage change in SV from Pre-RT to 2W:

$$\hat{\Delta} SV_{pre \to 2w,i}(rCBV) = \frac{GTV_{2w} \cdot \int P_j(x) H_{2w}(x) dx - GTV_{pre} \cdot \int P_j(x) H_{pre}(x) dx}{GTV_{pre} \cdot \int P_j(x) H_{pre}(x) dx} \cdot 100,$$

$$j \in \{low, intermediate, or high\} \textbf{ (Equation III.5)}$$

A similar calculation is applied to K^{trans}.

III.B.3.5 Association of the Physiological-parameter Defined Tumor Subvolume with Response

Endpoint. A percentage change in gross tumor volume (GTV) from pre to post RT was used as an endpoint for response assessment. Several patients did not have 3 or 6 months post treatment imaging follow-ups. For the patients in whom 3 and 6 months post-RT images were available, there were good correlations in the GTV changes between 1 and 3 months post RT and between 3 and 6 months post RT (data not shown). Also, previous studies indicate that brain metastases exhibit little pseudo-response and pseudo-progression one month after RT [49]. Therefore, we used a percentage change in the GTV from Pre-RT to 1 month post RT, $\hat{\Delta} GTV_{pre \to 1M\ Post-RT}$, as a measure of response to therapy.

44

From Pre-RT to 1M Post-RT, 16 tumors had a decrease in the GTV at least 25%, defined as responsive, 11 tumors had an increase at least 25%, defined as progressive, and the remaining 18 were defined as stable. We noticed that there were heterogeneous responses of multiple lesions from a single patient. Thus, each lesion was considered independently.

Statistical Analysis. First, we tested if there were any significant differences in changes of $\hat{\Delta}SV_{pre \to 2w, j}(rCBV)$ between responsive, stable, and progressive tumors using Mann-Whitney *U* Test. Similar tests were applied to changes in $\hat{\Delta}SV_{pre \to 2w, j}(K^{trans})$. To justify multiple comparisons (6 parameters), a *p*-value < 0.01 was considered as significance. Next, we performed a *Receiver Operating Characteristic* (ROC) analysis to evaluate sensitivity and specificity of the significant metrics identified in the previous test for predicting responsive tumors using software package ROCKIT [50]. Also, we compared these newly developed metrics with the conventional ones: a percentage change in the GTV from Pre-RT to 2W, $\hat{\Delta}GTV_{pre \to 2w}$, and a change in the mean rCBV (K^{trans}) values of a tumor from pre-RT to 2W, $\hat{\Delta}\mu_{pre \to 2w}(rCBV(K^{trans}))$, for predicting post treatment response. The significant difference of the area under ROC curves (AUC) between the metrics were compared by *t*-test, for which the standard error and the difference between the two AUCs were calculated by the method proposed by DeLong et al. [51]. Also, the leave-one-out technique was used to evaluate the prediction risk of the metrics. Furthermore, we estimated the sample size required for validation of the results in an independent study with a=0.05and power of 0.8 using the data in the current study.

III.B.3.6 Tumor Subvolume Defined by Combined Physiological Parameters

Finally, we tested whether combining the physiological parameters of rCBV and K^{trans} could improve prediction for tumor response. First, a joint histogram of rCBV and K^{trans} of a lesion is computed, e.g. H(rCBV = x, K^{trans} = y). Then, a joint probability function, $P_{j,k}$(rCBV, K^{trans}, α), is defined as follows:

$$P_{j,k}(rCBV, K^{trans}, \alpha) = \frac{P_j(rCBV) + \alpha \cdot P_k(K^{trans})}{1 + \alpha}$$

$$j, k \in \{low,\ intermediate,\ or\ high\} \qquad \textbf{(Equation III.6)}$$

where α is a weighting factor of the two parameters. Applying the joint probability function to Eq. III.5, a percentage change in the subvolume of a tumor defined by rCBV and K^{trans} classes from Pre-RT to 2W is given by:

$$\hat{\Delta}SV_{pre \to 2w, j, k}(rCBV, K^{trans}, \alpha) =$$

$$\frac{GTV_{2w} \cdot \iint P_{j,k}(x, y, \alpha) \cdot H_{2w}(x, y)dxdy - GTV_{pre} \cdot \iint P_{j,k}(x, y, \alpha) \cdot H_{pre}(x, y,)dxdy}{GTV_{pre} \cdot \iint P_{j,k}(x, y, \alpha) \cdot H_{pre}(x, y,)dx, dy} \cdot 100$$

$$j, k \in \{low,\ intermediate,\ or\ high\} \quad \textbf{(Equation III.7)}$$

We selected the weighting factor α that led to a maximum area under the ROC curve for predicting tumor response.

III.C Experimental Results

III.C.1 Probability Function Maps

Examples of maps of the probability functions belonging to the high rCBV class, high K^{trans} class and combination of two of a responsive and a stable lesion Pre-RT and at 2W are shown in Fig. III.2. Note that the spatial distribution of the probability function map of the

high rCBV class of a lesion can be different from one of the high K^{trans} class, and both can change from Pre-RT to 2W. For the responsive lesion, the voxel probability functions belonging to the high rCBV class were reduced to almost zero from Pre-RT to 2W, and for the stable lesion the reduction was in a much smaller extent.
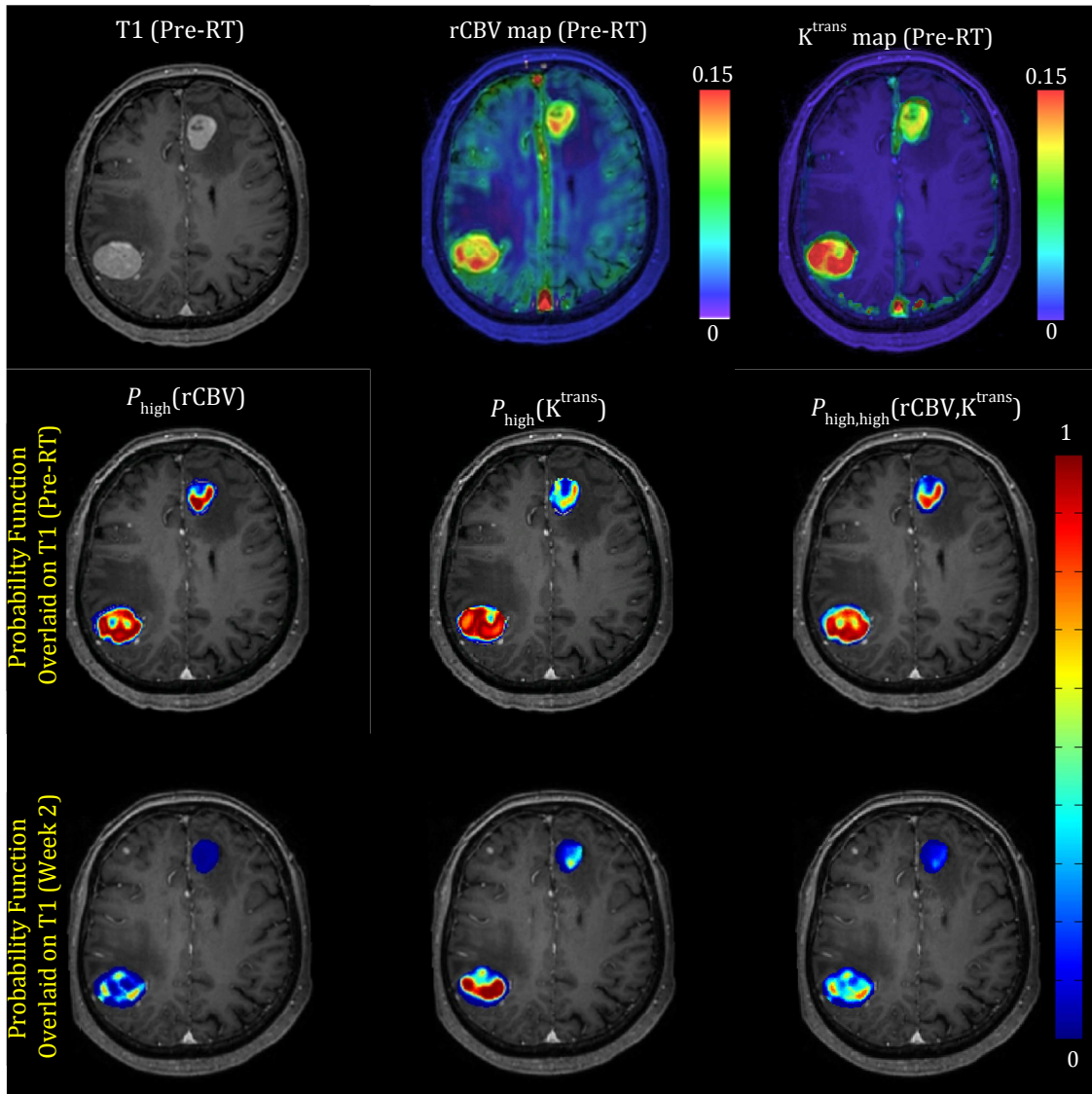
Fig. III.2. Example of physiological-defined tumor subvolumes and their longitudinal changes in a responsive and a stable lesion. Top row: Pre-RT T1 weighted image (left), and rCBV (middle) and K^{trans} (right) maps of a patient with two brain metastases; Middle and Bottom rows: Probability function maps of the high-rCBV class (Left column), high-K^{trans} class (Middle column) and combination of the two (Right column) overlaid on T1-W images Pre-RT (middle row) and 2W (bottom row). The anterior lesion is responsive and posterior one is stable.

47

III.C.2 Physiological-Parameter Defined Subvolumes

We found that the responsive tumors showed a greater decrease in the high-rCBV subvolume of the tumors from Pre-RT to 2W than the progressive tumors ($p<0.0072$) and a group of combining the progressive and stable lesions ($p<0.0057$). Also, the decrease in the high-rCBV sub-volume of the responsive tumors was marginally different from the stable ones ($p=0.033$) (Table III.2). Similar but much weaker trends were observed in the decrease of the high-K^{trans} subvolumes of the tumors between the groups. The percentage decrease in the tumor subvolumes defined by both high-rCBV and high-K^{trans} classes with an equal weighting (described in III.B.3.6) from Pre-RT to 2W differentiated the three groups with improved statistical significances, compared to using either variable alone. Specifically, the responsive group differed significantly from the progressive group ($p=0.0012$) and from the group of combining the progressive and stable tumors ($p=0.0017$). For the conventional metrics, a greater decrease was observed in the mean tumor rCBV from Pre-RT to 2W in the responsive group than in the stable tumors ($p<0.0049$) and the group of combining the stable and progressive ones ($p<0.0066$). Also, a decrease in the GTVs of the responsive tumors from Pre-RT to 2W was greater than in the progressive tumors significantly ($p<0.0039$) but marginally from the group of combining the progressive and stable tumors ($p<0.0124$).

Table III.2: Differences between responsive, stable and progressive tumors

Metric		R vs. S	S vs. P	R vs. P	R vs. {S & P}
				Group of lesions	
				p-value	
$\hat{\Delta}SV_{pre\to 2w,j}(rCBV)$	*j*=low	0.1086	0.2517	0.6392	0.1803
	j=intermediate	0.2771	0.3339	0.0513	0.0900
	j=high	0.0338*	0.3568	0.0072**	0.0057**
$\hat{\Delta}SV_{pre\to 2w,k}(K^{trans})$	*k*=low	0.1012	0.8750	0.1910	0.0773
	k=intermediate	0.3088	0.2909	0.8243	0.5613
	k=high	0.6663	0.0162*	0.0406*	0.4992
$\hat{\Delta}SV_{pre\to 2w,high,high}(rCBV,K^{trans},1)$		0.0218*	0.0758	0.0012**	0.0017**
$\hat{\Delta}SV_{pre\to 2w,high,high}(rCBV,K^{trans},0.6)$		0.0199*	0.0687	0.0012**	0.0015**
$\hat{\Delta}\mu_{pre\to 2w}(rCBV)$		0.0049**	0.2336	0.1088	0.0066**
$\hat{\Delta}\mu_{pre\to 2w}(K^{trans})$		0.5233	0.1704	0.5704	0.8775
$\hat{\Delta}GTV_{pre\to 2w}$		0.1086	0.0653	0.0039**	0.0124*

Abbreviations: GTV = gross tumor volume; R = responders; S = stables; P = Progressive; ^ The optimum value of α is 0.6, see the results of the ROC analysis. *: P<0.05; **: P<0.01.

III.C.3 Predictive Values of the Physiological-Parameter Defined Subvolumes

In prediction of post-RT response, the areas under the ROC curves were 0.80 ± 0.07 ($\pm$SEM), 0.70 ± 0.08, 0.67 ± 0.08 and 0.60 ± 0.08 for $\hat{\Delta}SV_{pre\to 2w,high}(rCBV)$, $\hat{\Delta}\mu_{pre\to 2w}(rCBV)$, $\hat{\Delta}GTV_{pre\to 2w}$ and $\hat{\Delta}SV_{pre\to 2w,high}(K^{trans})$, respectively (Fig. III.3), indicating that the high-rCBV defined subvolume of the tumor performed the best in predicting the responsive tumors. The change in the subvolume defined by the high-rCBV and high-K^trans classes, $\hat{\Delta}SV_{pre\to 2w,high,high}(rCBV,K^{trans},\alpha)$, resulted in the largest AUC, 0.86 ± 0.06. The pair-wise comparison of the ROC curves revealed that $\hat{\Delta}SV_{pre\to 2w,high,high}(rCBV,K^{trans},\alpha)$ was a slightly but not significantly better predictor than $\hat{\Delta}SV_{pre\to 2w,high}(rCBV)$ ($p > 0.18$), or $\hat{\Delta}\mu_{pre\to 2w}(rCBV)$

($p > 0.05$). However, both $\hat{\Delta}SV_{pre \to 2w, high}(rCBV)$ and $\hat{\Delta}SV_{pre \to 2w, high, high}(rCBV, K^{trans}, \alpha)$ were significantly better predictors than $\hat{\Delta}GTV_{pre \to 2w}$ ($p = 0.02$ and $p = 0.01$, respectively). Finally, $\hat{\Delta}\mu_{pre \to 2w}(rCBV)$ was a better predictor than $\hat{\Delta}GTV_{pre \to 2w}$ ($p > 0.4$), but not significantly. Also, the application of the leave-one-out technique resulted in the average AUCs of 0.857 ± 0.062(±SEM), 0.79 ± 0.0672, and 0.68 ± 0.087 for $\hat{\Delta}SV_{pre \to 2w, high, high}(rCBV, K^{trans}, \alpha)$, $\hat{\Delta}SV_{pre \to 2w, high}(rCBV)$, and $\hat{\Delta}GTV_{pre \to 2w}$, respectively, suggesting no significant bias in the computed ROCs. Also, it requires a sample size of 110 lesions with 39 responsive ones to validate the results in an independent study.
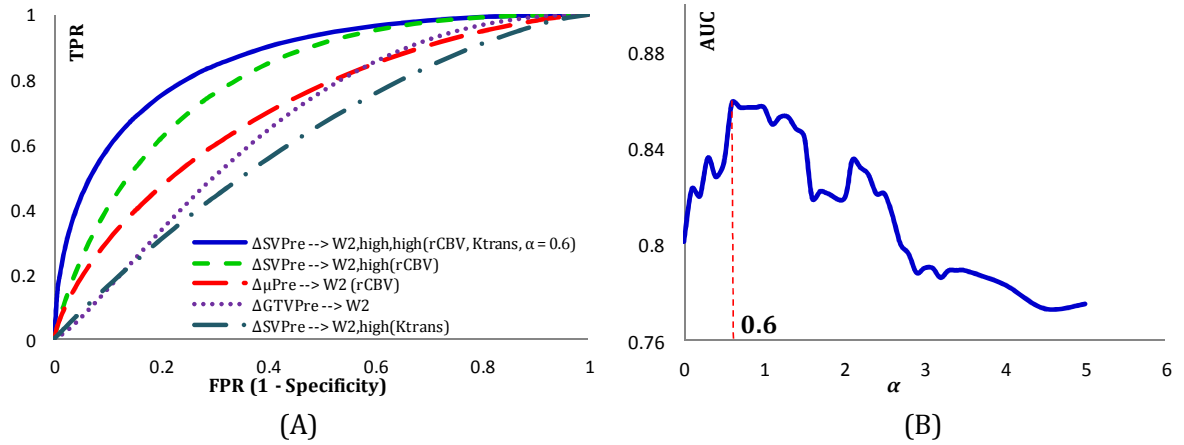
Fig. III.3. Performance of the metrics listed in Table III.2 in prediction of responsive lesions. (A) ROC analysis (B), AUC vs α in Eq III.6. FPR: False Positive Rate TPR: True Positive Rate; AUC: Area Under Curve;

III.D Discussion

In this chapter, we proposed a new approach to delineate the subvolums of a tumor defined from physiological imaging-parameters and related their early changes to

50

treatment response in patients who had brain metastases and were treated by WBRT. Our proposed approach analyzes the heterogeneous distributions of physiological and/or biological imaging-parameters of the tumors, then assigns each tumor voxel a probabilistic membership function belonging to the physiological/biological classes defined in a sample of tumors, and then calculates the related subvolumes in each tumor. In the application of our approach to rCBV and K^{trans} images of brain metastases, we found that a percentage decrease in the tumor subvolumes defined by the high-rCBV class from Pre-RT to 2 weeks after the start of RT predicted volumetric tumor response one month after RT. The ROC analysis showed that this new metric was significantly better than the decrease in the gross tumor volume (GTV) observed during the same time interval for predicting post-therapy response, suggesting that physiological imaging adds discriminatory information compared to the volumetric change. The framework presented in this study can be applied to other physiological, metabolic or molecular images, e.g., apparent diffusion coefficient and ^{11}C-Methinion PET, to delineate a different physiological-parameter defined subvolume of a tumor. A subvolume of the tumor defined in such way could be a candidate as a boost target.

Our proposed approach differs from the method that generates the parametric response map (PRM) [52] and the one that uses hard thresholding to divide the tumor volume [53]. In the PRM method, after co-registration of a pair of images acquired at two different time points over therapy, a voxel-to-voxel comparison is applied to the images, and a response value is assigned to each voxel according to its change above or below a cutoff threshold. Although analyzing a voxelwise change in a tumor is an interesting approach, mis-registration of the image voxels, particularly in region where a tumor

51

shrinks or grows during the time interval, could compromise the result. In addition, the PRM-based analysis considers an absolute change in rCBV/K^{trans}, regardless of the original value of the physiological parameters, whereas an increase/decrease in the low or high-perfused voxels may have a very different implication. For example, a decrease in regions with high perfusion may be more related to treatment response than a decrease in low-perfused areas. Also, while using a threshold value to segment a tumor volume is simple, the binary decision discards parameter continuity at the threshold value. Furthermore, finding an adequate threshold value is always a challenge, and often done empirically and sometimes arbitrarily. In contrast, our approach does not depend upon voxelwise accuracy of image registration or use any hard threshold to determine the subvolume of the tumor. It is worth to point out that our proposed method incorporates the tumor volume into analysis, and thus a change in the defined subvolumes represents both physiological and morphological changes in a tumor, which could increase the sensitivity in prediction of tumor response to therapy as well. Also, although our method does not rely on accuracy of image registration, spatial information of the subvolume of physiological imaging parameters at each time point of measurement is well preserved as shown in Fig III.2.

The previous studies have shown that a high mean or regional value of CBV or K^{trans} in the brain tumor prior to therapy is correlated with a high tumor grade [47], and worse outcome [48]. A reduction in the high CBV and/or K^{trans} in brain tumors during radiation therapy is associated with better outcome [48]. All these suggest that high-CBV and/or K^{trans} in the brain tumor, as an imaging-defined tumor "phenotype", and the related changes during therapy could be important prognostic and predictive indictors. Our results indicate that the early change in the high rCBV-defined subvolume of the tumor has the potential to

be used for selecting the lesion and defining the target for intensified treatment. To improve the performance of the proposed metric (from AUC=0.86), our general approach can be used to test whether including other physiological imaging parameters into analysis, e. g. apparent diffusion coefficient or ^{11}C-MET PET, by creating a joint probability function and joint histogram, can improve prediction of treatment response. This type of analysis can help determine whether multiple physiological and metabolic imaging parameters provide complementary or redundant information. Also, it is interesting to further establish the relationship between the imaging-defined and molecular biology-defined "phenotypes" in the tumor and response to radiation, as it has been shown in a previous study that poor perfusion in head and neck squamous cell carcinoma xenografts is associated with less radiation-induced double-strand DNA damage [54]. Therefore, a poorly perfused subvolume of head and neck cancers could be a candidate for boost target [55]. The similar concept could also apply to Glioblastoma Multiforme.

III.E Conclusion

In this chapter, we delineated the subvolumes of a tumor for therapy assessment and guidance using physiological parameters such as the regional cerebral blood volume (rCBV) and the Gd-DTPA transfer constant (K^{trans}) derived by fitting the dynamic contract enhanced (DCE) curves into a pharmacokinetic model. However, as mentioned in chapter I, using pharmacokinetic model to obtain the physiological parameter maps involve in series of uncertainties. Hence, we also aim to see if directly analyzing the DCE curves could provide similar results to what we obtained in this chapter with the goal of achieving an automatic and faster decision making tool for therapy assessment and guidance. The next

chapter is entirely devoted to this issue. Also, we are willing to consider the role of other physiological parameters such as apparent diffusion coefficient (ADC) and investigate if adding the diffusion data could improve the prediction results or not. We discuss this in the chapters V and VI, respectively. At last, further development and testing of the method proposed in this chapter using larger database and other types of tumors, such as glioblastoma and liver tumors, warrants its value for outcome prediction and therapy guidance.

DCE-MRI Defined Subvolumes of a Tumor for Therapy Assessment

IV.A Introduction

As mentioned in chapter I, the physiological parameter maps derived from the pharmacokinetic (PK) models, although useful for diagnosis and therapy assessment, involve in a series of uncertainties [56]. Foremost, the DCE-MRI data often cannot be fitted to a selected PK model perfectly, and hence may be a source of errors affecting the accuracy of the physiological parameters. In addition, the "physiological parameters" derived from the PK models may not accurately reflect the underlying physiology, due to oversimplification in the models and lack of physiological validation of the models. For example, interpretation of K^{trans} derived from the Toft model [20] depends upon flow limited, permeability limited or mixed. Also, computing the physiological parameters by fitting the DCE-MRI data into the PK models is time consuming, which is inadequate for decision making support in therapy assessment. Hence, a model free approach to analyze the DCE-MRI data (e.g., the methods based on factor analysis [57-58], independent component analysis (ICA) [59], and principal component analysis (PCA) [60-63]) could potentially facilitate the development of the real-time decision-making supportive tools in diagnosis and therapy assessment. PCA has shown the potential to be a very robust and fast technique in analyzing the DCE-MRI data [60-63]. However, to the best of our knowledge,

no standard approach has been proposed so far to incorporate PCA into an automatic supportive tool for decision-making in therapy assessment. Hence, the main goal in this work is to develop a pharmacokinetic model free framework combining PCA and a pattern recognition technique to facilitate the process of decision making in therapy assessment.

As shown in chapter III, an early change in the subvolume of a brain metastatic tumor with high-rCBV and high-K^{trans} is a better predictor for post radiation therapy response than a tumor volumetric change and a change in the mean tumor rCBV observed in the same time interval. In previous chapter, we showed that the physiological imaging-defined tumor subvolume, as a response-predictor, is determined through a two-step process: 1) deriving the physiological parameters by fitting the DCE MRI data to a PK model and 2) delineating the subvolume by analysis of the physiological parameters in the tumor using a pattern recognition technique. Hence, in this chapter, the main goal is to develop a general framework to derive a response-predictor from DCE-MRI data without using the PK modeling and to have a semi-automated or fully automated tool for supporting clinic decision-making. We evaluated whether our model-free approach could provide a similar or even better metric, in defining the subvolume of a tumor, for assessment of therapy response, compared to the subvolume defined by the physiological parameters obtained from the PK model. We compared the two approaches using the same patients described in chapter II.

IV.B Materials and Methods

Our proposed PK model free framework consists of two phases: development phase and usage phase. In the development phase, a sample of the DCE data from tumors is processed and analyzed to develop the model and the predictive metric. In the usage phase, we

determine if the predictive metric could be extracted rapidly from the DCE data of a new patient scan.

IV.B.1 Development Phase

A flowchart of the development phase, shown in Fig. IV.1, includes preprocessing, modeling of DCE curves of a sample of tumors (including PCA and feature classification) to obtain a single metric, and evaluating the metric for response assessment. Each step is described in the following subsections in detail.

Development Phase
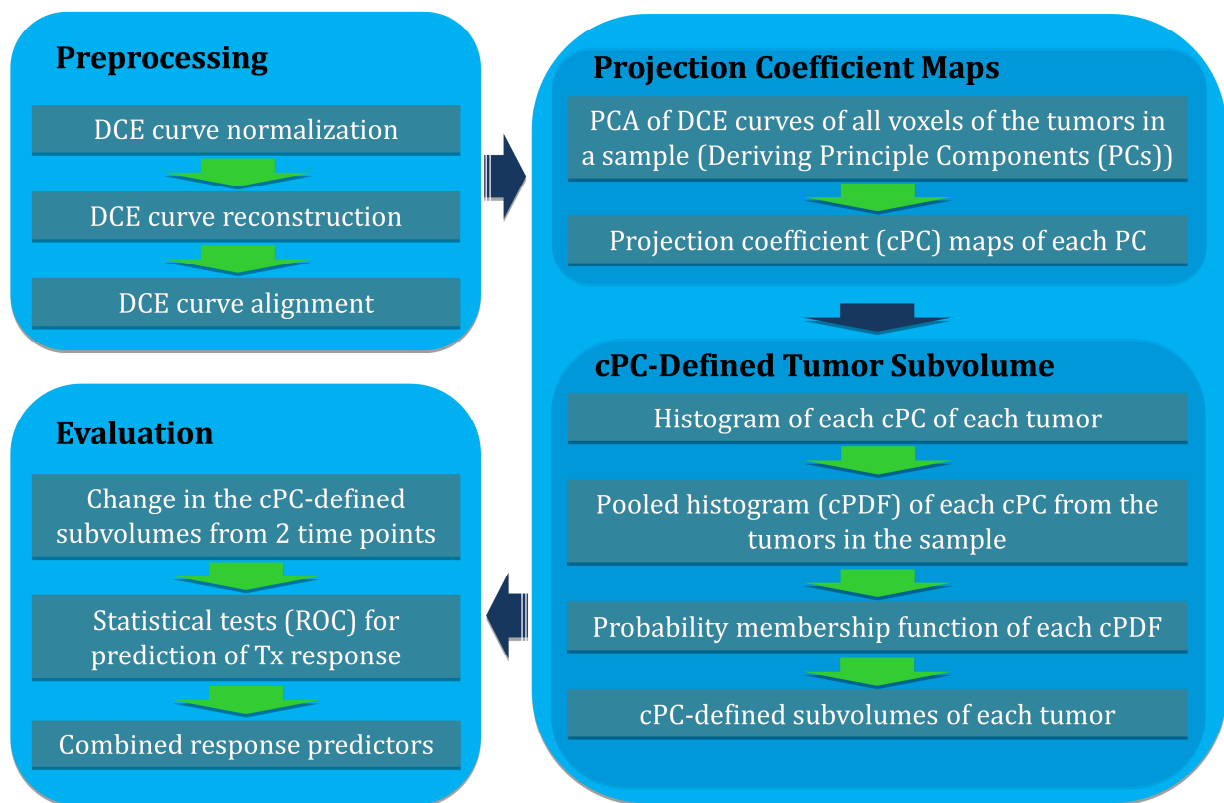
Fig IV.1. The flowchart of our proposed PK model free approach to analyze the tumor DCE data for supporting decision-making of assessment of therapy response. cPC: Projection coefficient map; cPDF: Pooled histogram corresponding to a cPC.

IV.B.1.i Pre-processing

DCE Curves Normalization: The dynamic curve at each voxel represents the temporal changes in signal intensity after the contrast injection. We calculate the signal intensity change ΔS from pre (baseline) to post contrast as following:

$$\Delta S(t) \equiv \frac{S(t) - S_0}{S_0}$$ **(Equation IV.1)**

where $S(t)$ and S_0 represent signal intensities of a DCE curve at times t and 0 (the time of contrast injection), respectively. Note that ΔS(t) is proportional to ΔR1, the change in the longitudinal relaxation rate, as long as TR x R1 << 1. To account for the individual hemodynamic response to contrast, we normalize ΔS at each voxel using the peak of the arterial input function, AIF_{max}, obtained during the same scan as:

$$\Delta S_N(t) = \Delta S(t) \cdot \frac{1}{AIF_{max}}$$ **(Equation IV.2)**

An arterial input function can be determined from a region of interest (ROI) in a large artery (e.g., carotid artery for our application) manually, semi-automatically or automatically.

DCE Curve Reconstruction: The DCE curves in each scan may not be acquired with the exactly same temporal resolutions and time durations. Hence, we standardize the DCE curves in such a way that all curves have the same temporal resolution and length. We use the spline curve-fitting method [64] to reconstruct each DCE curve, and then resample them to have a same temporal resolution and total length.

DCE Curve Alignment: The DCE curves from voxels within the tumor volumes of all patients need to be temporally aligned for further processing. We use the arterial input

function (AIF) obtained from each patient scan to align the DCE curves of voxels in the tumor volumes. First, we fit the Gamma variate function [65] to each AIF as follows:

$$g = \begin{cases} (t - t_0)^\alpha exp^{-\beta(t-t_0)} & t \geq t_0 \\ 0 & t < 0 \end{cases}$$

(Equation IV.3)

$$AIF = g(t) + \lambda \int_0^t g(t - \acute{t}) d\acute{t}$$

All AIFs are then aligned at t_0 that is resigned to be time 0. Using the resultant time shifts, the DCE curves from each scan are adjusted accordingly.

IV.B.1.ii Projection Coefficient Map from Karhumen-Loeve Expansion of DCE Curves

Our primary goal is to extract response-predictive features rapidly and directly from the DCE curves. Hence, we expand the DCE curves using a set of basis functions, by which the coefficients of the projection vectors for each DCE curve is a unique representation in a new space. First, in the development stage, using DCE data from a sample of tumors (e.g. pre-therapy DCE data), we construct matrix **C** (N x T) in which each row represents a DCE curve from one voxel in the tumors. N is the total number of voxels in all tumors and T is the number of time points in each curve. Next, we apply principal component analysis (PCA) to **C** to obtain a complete set of a total of T orthonormal principal components (PC_i). Then, we perform the Karhumen-Loeve transformation of each DCE curve, ΔS_N, in each voxel of the tumor to:

$$\Delta S_N = \sum_{i=1}^T a_i PC_i \rightarrow \Delta S_N \equiv (a_1, a_2 \ldots, a_T)$$ **(Equation IV.4)**

where a_i is the projection coefficient (cPC) corresponding to the ith principal component. Hence, each DCE curve in a tumor volume is represented uniquely by $\{\alpha_i\}$ in a T-

dimensional coefficient space. However, Eq. IV.4 can be truncated at the first M principal components which contain 99% of energy of the original DCE curves. We will show that M is significantly smaller than T. Decomposing DCE curves of a new tumor to the first M PCs is much faster than fitting them to a PK model. We will show later that this process reduces the computation time and burden dramatically.

IV.B.1.iii Projection Coefficient Defined Tumor Subvolumes

Probability Density Function of a Projection Coefficient in a Tumor: Each PC depicts a feature of the tumor DCE curve. Each voxel in a tumor has a unique projection coefficient on each PC. For each PC, the projection coefficients of the voxels in a tumor, which can be presented as a volumetric map of a lesion, have a distinct role in predicting the treatment response and outcome. The distribution of the projection coefficients in a large tumor is heterogeneous, similar to the physiological parameters. Hence, similar to what has been done previously for the physiological parameters and described in previous chapter, we analyze the distribution patterns of a projection coefficient, a_i, in the lesions, and subsequent changes during treatment. A probability density function (PDF) or histogram of a_i of a lesion is generated similarly. The PDF consists of 150 evenly-spaced points to cover the range of a_i for all the lesions of interest. A value of the PDF at a point *x*, $H(a_i = x)$, of a lesion is calculated as:

$$H(a_i \ = \ x) \equiv n_i : x - \varepsilon \leq a_i \ < x + \varepsilon \qquad \textbf{(Equation IV.5)}$$

where n_i is the number of voxels within $|a_i$ -*x*$| < \varepsilon$, and ε is a smooth factor of *H* and set as $\varepsilon = \frac{\sigma}{4}$ where σ denotes a standard deviation of the a_i distribution in the tumor. For each

lesion, PDFs are calculated for scans at baseline (e.g., Pre-therapy as $H_{Pre}(x)$) and after

starting therapy (e.g. at week-2 during therapy as $H_{2W}(x)$). After $H_{Pre}(x)$ is normalized to

have an area under the PDF curve equal to one ($\int H(x)dx = 1$), the $H_{Pre}(x)$s of all the

lesions are summed to generate a pooled PDF (*cPDF*), in which each lesion has an equal

contribution regardless of its size (Fig. IV.2(B)). An example of $H_{Pre}(x)$ of a lesion is shown

in Fig. IV.2(A).
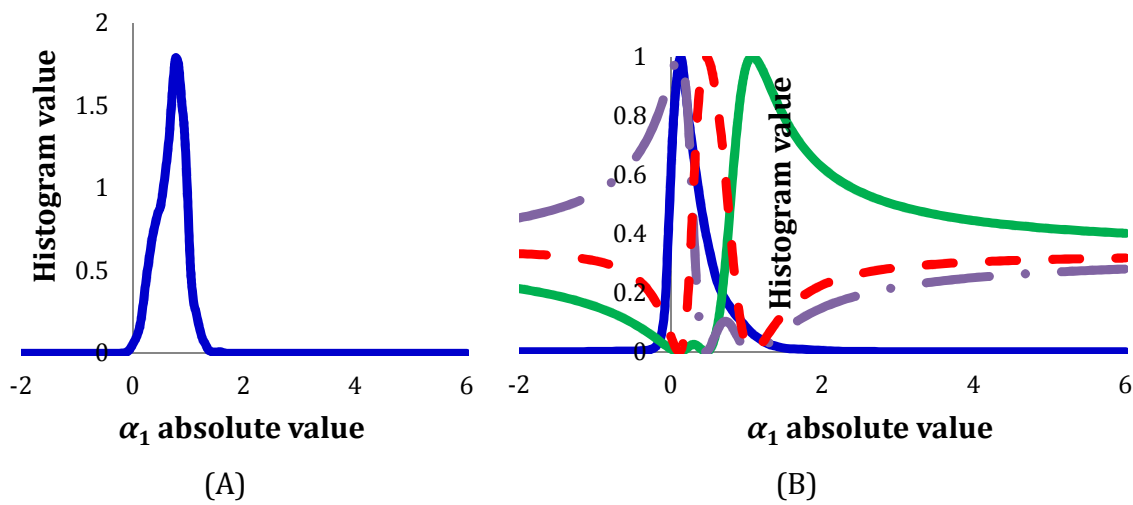
Fig IV.2. Application of FCM in classification of tumor space into classes of low, intermediate and high a_1. (A): An example of the Pre-RT a_1 histogram of a brain metastasis with a tumor volume of 17.6 cm³. (B): The pooled PDF (light gray) of the Pre-RT a_1 (*cPDF₁*) from all the lesions and the three probability membership functions determined by FCM clustering. The cPDF₁ is partitioned into three classes: representing low (dot-dashed black), intermediate (dashed black) and high (solid black) a_1 classes. a_1: coefficient projection of the DCE curves on the 1st principal component.

Probabilistic Membership Functions of Projection Coefficients: Previous studies have

suggested that the rCBV (or K^trans) distribution in a brain tumor is abnormal compared to

normal cerebral tissue, as elevated rCBV in a subvolume of the tumor and low rCBV in

another one [66-67]. A renormalization of tumor vasculature, such as decreasing the

elevated rCBV and increasing the low one, could be an indicator of a tumor response to

treatment [47-48]. The DCE-derived physiological parameters (e.g., rCBV and K^trans) and

projection coefficients, $(a_1, a_2 \ldots, a_T)$, are two representations of the DCE curves. Therefore, it is reasonable to assume that a_i in the tumor could also distribute abnormally in contrast to normal tissue, and changes during treatment could predict tumor response to therapy. Hence, similar to what has been done for rCBV and explained in previous chapter, we classify the pooled distribution of $H_{pre}(a_i)$ to three classes as high, intermediate and low a_i classes using fuzzy-c-means (FCM) clustering by minimizing an objective function J_m:

$$J_m = \sum_{i=1}^{N} \sum_{j=1}^{C} P_j(a_i)^m \|a_i - c_j\|^2, 1 \leq m < \infty \qquad \textbf{(Equation IV.6)}$$

where c_j is a prototype vector of the jth class, $P_j(a_i)$ is a probabilistic membership of a a_i value belonging to the jth class, and m is a fuzzy exponent and chosen as 2. The solutions of Eq. IV.6 are determined iteratively by:

$$c_j = \frac{\sum_{i=1}^{N} P_j(a_i)^m \cdot a_i}{\sum_{i=1}^{N} P_j(a_i)^m}, \qquad \textbf{(Equation IV.7)}$$

$$P_j(a_i) = \frac{1}{\sum_{k=1}^{C} \left[\frac{\|a_i - c_j\|}{\|a_i - c_k\|}\right]^{\frac{2}{m-1}}}. \qquad \textbf{(Equation IV.8)}$$

until reaching stopping criteria. Note that the FCM cluster analysis does not classify a a_i value into a single class (no hard threshold) rather generates a probabilistic function of a_i that belongs to a class. The probabilistic membership function, $P_j(a_i)$, describes that a voxel having a projection coefficient a_i has a probability P belonging to a class j, which is a new representation of a a_i value of a tumor voxel (mathematically transfers the data from the a_i space into a new space) see Fig. IV.2(B).

Projection Coefficient Defined Tumor Subvolume: Primary interest is to test if a change in a subvolume of the tumor defined by high, intermediate or low a_i values is

related to tumor treatment response. We define a subvolume (SV) of a tumor with low, intermediate or high a_i using the probabilistic membership function $P_j(a_i)$, and calculate a percentage change in the SV from pre-therapy to after starting treatment (e.g., 2 weeks) as:

$$\hat{\Delta}SV_{Pre \to 2W,j}(a_i) = \frac{GTV_{2W} \cdot \int P_j(a_i).H_{2W}(a_i)da_i - GTV_{Pre} \cdot \int P_j(a_i).H_{Pre}(a_i)da_i}{GTV_{Pre-RT} \cdot \int P_j(a_i).H_{Pre}(a_i)dx} \cdot 100,$$

$$j \in \{low, intermediate, or\ high\} \qquad \textbf{(Equation IV.9)}$$

We will test whether a change in each of the first M cPC defined tumor subvolumes during RT is associated with post-RT tumor response in a group of patients, which will be described in evaluation section.

Tumor Subvolume Defined by Combined Projection Coefficients : We would like to test if combining the different *cPCs* could improve prediction for tumor response compared to using one *cPC*. To do so, first a joint histogram of $(a_1, a_2 ..., a_M)$ of a lesion is computed, e. g. $H(a_1 = x_1, a_2 = x_2, ... a_M = x_M)$. Then, a joint probability function, $P(\{a_i\}, \{\beta_i\})$, is defined as:

$$P(\{a_i\}, \{\beta_i\}) = \frac{P_{j_1}(a_1) + \sum_{i=2}^{M} \beta_i P_{j_i}(a_i)}{1 + \sum_{i=2}^{M} \beta_i}, \beta_1 = 1 \qquad \textbf{(Equation IV.10)}$$

where β_i is the weighting factor of each coefficient and $j_i \in \{low, intermediate, or\ high\}$. Applying the joint probability function to Eq. IV.10, a percentage change in a subvolume of a tumor defined by $\{a_i\}$ classes from Pre-therapy to after starting treatment (e.g. 2 weeks (2W)) is given by:

$$\hat{\Delta}SV_{Pre \to 2W}(\{a_i\}, \{\beta_i\}) =$$

$$\frac{GTV_{2W} \cdot \int \int ... \int P(\{a_i\}, \{\beta_i\}) H_{2W}(a_1 a_2 ... a_M) da_1 ... da_M - GTV_{Pre} \cdot \int \int ... \int P(\{a_i\}, \{\beta_i\}) H_{Pre}(a_1 a_2 ... a_M) da_1 ... da_M}{GTV_{Pre} \cdot \int \int ... \int P(\{a_i\}, \{\beta_i\}) H_{Pre}(a_1 a_2 ... a_M) da_1 da_2 ... da_M} \cdot 100$$

$$\textbf{(Equation IV.11)}$$

The weighting factor $\{\beta_i\}$ can be selected based upon the best prediction for response from a developmental dataset and evaluated by an independent data set. We will demonstrate the principle in next section.

IV.B.2 Image Processing for a New Tumor

For a new patient scan, first, we perform pre-processing of the DCE curves and then compute the projection coefficient maps of the first M or selected principal components. Next, we compute the histograms or a joint histogram of the selected coefficients within the tumor. Then, using the probability membership function obtained in the development step, we calculate the cPC-defined tumor subvolumes by Eqs. IV.10 or IV.11. Finally, we determine a change of the subvolume from pre-therapy to during or post therapy (Fig. IV.3).
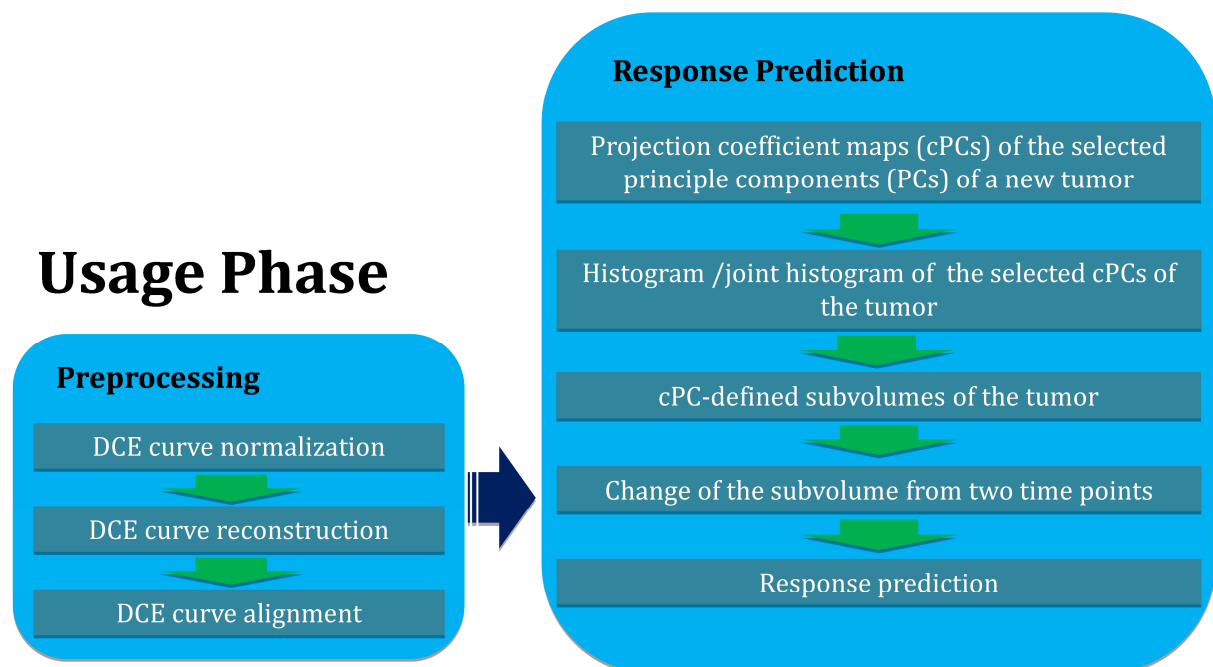
Fig IV.3. A flowchart of the procedure required for a new patient scan

IV.B.3 Evaluation

IV.B.3.i Patient

We have used the same patient list described in previous chapter to evaluate our proposed PK model free approach and compare it with other metrics.

IV.B.3.ii Imaging Acquisition and Processing

Image Acquisition. All patients had MRI scans on a Philips 3T scanner prior to radiation therapy (Pre-RT), 2 weeks after the start of RT (2W), and 1 month after the completion of treatment (1M Post-RT). MRI scans included pre and post Gd-DTPA volumetric T1 weighted images, multi-slice 2D T2 weighted images, and volumetric dynamic contrast enhanced (DCE) T1 weighted images. The 3D volumetric DCE-images were acquired during bolus injection of a standard dose of 2Gd-DTPA with an injection rate of 2 cc/s. The DCE-images were acquired in the sagittal plane with an image matrix of 128 x 128 x 80, a field-of-view of 240 x 240 x 160 (mm), a voxel size of 2 x 2 x 2 (mm^3), a flip angle(α) of 20°, and TE/TR of 1.04/5.14 msec and a temporal resolution of 6 sec. Using an in-house software package, Functional Image Analysis Tools (FIAT) [46], both anatomical and DCE-MR images were co-registered and resampled to have a voxel size of 0.9375 x 0.9375 x 3 (mm^3). Each lesion of interest was manually contoured by a physician on the post-Gd T1 weighed images obtained pre-RT, 2W and 1M post-RT.

Pre-processing. DCE images were pre-processed as explained above. The arterial input function of each patient scan was obtained by the following steps: First, a region of interest containing brain and neck is contoured. Then, DCE curves within the contour are averaged to determine the peak enhancement, T_{max}, in the tissue. Assuming that the arterial

input function reaches the enhancement peak prior to tissue, the first 20 voxels with the maximum enhancement in $\Delta S(T_{max} - \Delta t)$, one time frame before T_{max}, within the contour are thresholded, and then the corresponding DCE curves are averaged to be considered as an arterial input function. Currently, this is done semi-automatically, but can be fully automated. Then, DCE curve in each voxel of the tumors was reconstructed to have a temporal resolution of 4 sec and a total length of 120 sec and re-aligned, respectively.

Model Development. We pooled the DCE curves from all voxels of all 45 lesions pre-RT together to determine the PCs, but not ones at week-2 during RT. After obtaining the projection coefficient map for each tumor by projecting the DCE curves onto the PCs, the probability memberships of classes of each of projection coefficients were determined by using pre-RT data only.

cPC defined Subvolume. A change in a tumor subvolume defined by a projection coefficient class from pre-RT to 2W was calculated by Eqs. IV.9 or IV.11.

IV.B.3.iii Association of the cPC Defined Tumor Subvolume with Response

Endpoint. We used the same endpoint described in chapter 3 to evaluate our proposed PK model free approach and compare it with other metrics.

Statistical Analysis. First, we tested if there were any significant differences in the changes of $\hat{\Delta} SV_{Pre-RT \rightarrow 2W,i}(a_i)$ between responsive, stable, and non-responsive tumors using Mann-Whitney U Test. To justify multiple comparisons, a *p*-value < 0.01 was considered as significant. Next, we performed a *Receiver Operating Characteristic* (ROC) analysis to evaluate sensitivity and specificity of the significant metrics identified in the previous test for predicting responsive tumors using software package ROCKIT [50]. Also,

we compared these newly developed metrics with the conventional metrics including a percentage change in the gross tumor volume (GTV) from Pre-RT to 2W, $\hat{\Delta}GTV_{Pre \to 2W}$, and a change in the mean rCBV values of a tumor from pre-RT to 2W, $\hat{\Delta}\mu_{Pre \to 2W}(rCBV)$, for predicting post treatment response. The significant difference of the area under ROC curves (AUC) between the metrics were compared by *t*-test, for which the standard error and the difference between the two AUCs were calculated by the method proposed by DeLong et al. [51]. For the tumor subvolume defined by combining more than one cPC, we used the maximum AUC to determine the $\{\beta_i\}$.

IV.C Experimental Results

IV.C.1 Principal Components (PCs)

PCA revealed that the first three principal components (PCs) comprised more than 99% of the energy of the DCE curves of the tumors. Fig. IV.4 shows the first three principal components. Our further investigation (data not shown) revealed that the first component was related to the area under each DCE curve, while the second and third ones were associated with the enhancement rate of a DCE curve and its derivative, respectively. Fig. IV.5 shows the heterogeneous distributions of the first three cPC maps of a tumor, indicating an average cPC in the tumor would not be sensitive to a heterogeneous change. Therefore, the analysis described in the method section was applied to the histograms of the first three cPCs in a tumor to determine the subvolume of the tumor with a given class.
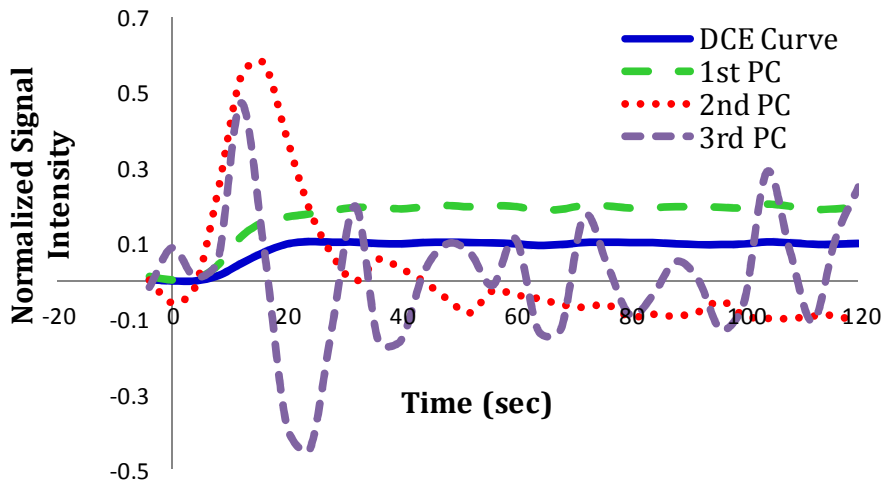
Fig. IV.4. An example of a typical DCE curve for a brain metastatic lesion and the first three principal components (PCs) resulted after applying PCA to the DCE-Matrix. The coefficient maps achieved by projecting the DCE curve onto the first three components are related to the area under the DCE curve, enhancement rate and first derivative of the enhancement rate, respectively.
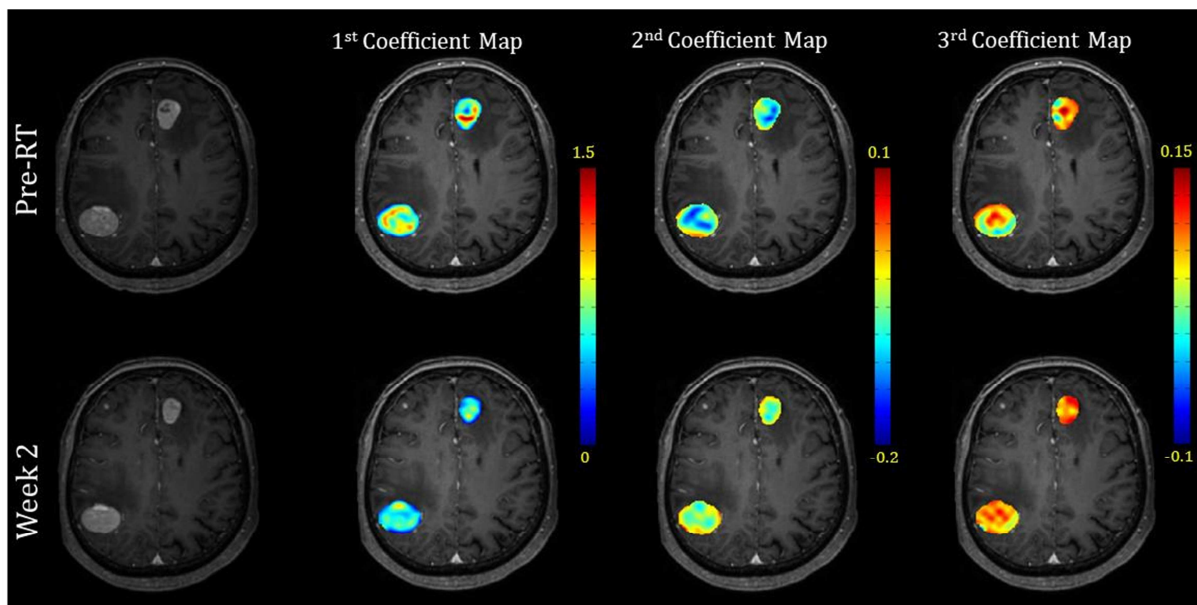
Fig. IV.5. Distribution patterns of the first three projection coefficient maps in tumors overlaid on T1-weighted images pre-RT and week 2 after start of whole brain radiotherapy.

IV.C.2 Association of cPC-Defined Tumor Subvolume with Response

Associations of the changes in the first three cPC-defined tumor subvolumes with high, intermediate or low coefficients from pre-RT to 2W with the tumor response to

68

treatment are given in Table IV.1. We found that for the responsive group, a percentage decrease in the high-a_1 subvolumes of the tumors from Pre-RT to 2W differed significantly from the progressive group ($p<0.0015$) and from a group combining progressive and stable tumors ($p<0.0017$), but marginally from the stable group ($p<0.0199$), Table IV.1. A change in the intermediate-a_1 or low-a_1 subvolumes of the tumors from pre-RT to 2W did not differentiate any response groups. We observed a similar but weaker trend for a_2. Furthermore, a percentage decrease in the low-a_3 subvolume of the tumor was more associated with tumor response than the high-a_3 or intermediate-a_3 subvolume. Also, a percentage decrease in the subvolumes defined by combining the high-a_1 and low-a_3 classes from pre-RT to 2W revealed that adding a_3 improved the statistical significance for differentiating the responsive tumor from the group of stable and progressive lesions compared to either coefficient alone but a_2 did not add discriminatory information.

For comparison, the results of the rCBV-K^{trans} analysis that were reported in the previous chapter and other conventional metrics are included in Table IV.1. In summary, we found that the percentage decrease in the high-rCBV subvolumes of the tumors from Pre-RT to 2W of the responsive group differed significantly from the progressive group ($p<0.0072$) and from a group combining progressive and stable tumors ($p<0.0057$), but not from the stable group ($p=0.033$) (Table IV.1). The percentage decrease in the tumor subvolumes defined by both the high rCBV and high K^{trans} classes from Pre-RT to 2W differentiated the three groups with improved statistical significances, compared to using either variable alone. Specifically, the responsive group significantly differed from the progressive group ($p=0.0012$) and from the group combining the progressive and stable tumors ($p=0.0015$). For the conventional metrics, the decrease in the mean tumor rCBV

from Pre-RT to 2W of the responsive group differed significantly from the stable group (p<0.005) and the group of combining the stable and progressive tumors (p<0.0066); and the percentage decrease in the GTVs from Pre-RT to 2W of the responsive group differed significantly from the progressive group (p<0.004) but marginally from the group of combining the progressive and stable tumors (*p*<0.012). These data show that both physiological-defined and cPC-defined subvolumes of a tumor achieve a similar level of statistical significance in differentiation of responsive, stable and progressive tumors.

Table IV.1: Differences between responsive, stable and non-responsive tumors

Metric		Group of lesions			
		R vs. S	S vs. NR	R vs. NR	R vs. {S & NR}
		p-value			
$\hat{\Delta}SV_{Pre \to 2W,j}(a_1)$	j=low	0.8766	0.7024	0.3878	0.5937
	j=intermediate	0.2477	0.3339	0.0457	0.0773
	j=high	0.0199*	0.1321	0.0015**	0.0017**
$\hat{\Delta}SV_{Pre \to 2W,j}(a_2)$	j=low	0.7431	0.7702	0.3359	0.4843
	j=intermediate	0.8766	0.2002	0.1596	0.5774
	j=high	0.3979	0.0561	0.0096**	0.0661
$\hat{\Delta}SV_{Pre \to 2W,j}(a_3)$	j=low	0.0068**	0.2002	0.1323	0.0094**
	j=intermediate	0.7693	0.2909	0.2083	0.4133
	j=high	0.1522	0.0143	0.1088	0.8403
$\hat{\Delta}SV_{Pre \to 2W,high,low}(a_1, a_3, 0.3)^{\wedge}$		0.0018	0.3568	0.0053	0.0005
$\hat{\Delta}SV_{Pre \to 2W,j}(rCBV)$	j=low	0.1086	0.2517	0.6392	0.1803
	j=intermediate	0.2771	0.3339	0.0513	0.0900
	j=high	0.0338*	0.3568	0.0072**	0.0057**
	j=low	0.1012	0.8750	0.1910	0.0773
$\hat{\Delta}SV_{Pre \to 2W,j}(k^{trans})$	j=intermediate	0.3088	0.2909	0.8243	0.5613
	j=high	0.6663	0.0162*	0.0406*	0.4992
$\hat{\Delta}SV_{Pre \to 2W,high,high}(rCBV, k^{trans}, 0.6)$		0.0199*	0.0687	0.0012**	0.0015**
$\hat{\Delta}\mu_{Pre \to 2W}(rCBV)$		0.0049**	0.2336	0.1088	0.0066**
$\hat{\Delta}\mu_{Pre \to 2W}(k^{trans})$		0.5233	0.1704	0.5704	0.8775
$\hat{\Delta}GTV_{Pre \to 2W}$		0.1086	0.0653	0.0039**	0.0124*

Abbreviations: GTV = gross tumor volume; R = responders; S = stables; NR = non-responders; ^The optimum value of β_3 is 0.3, see the results of the ROC analysis. *: P<0.05; **: P<0.01.

IV.C.3 Predictive Values of the cPC Defined Subvolumes

We explored the predictive value of the decrease in the subvolumes of the tumors defined by the cPCs from Pre-RT to 2W for predicting responsive tumors post-RT, and compared their performance with the decrease in subvolumes of the tumors defined by the high rCBV and high K^{trans} and two conventional metrics. The ROC analysis showed that the AUCs were $0.83 \pm 0.06(\pm SEM)$, 0.77 ± 0.07, 0.80 ± 0.07, 0.70 ± 0.08, 0.67 ± 0.08 and 0.56 ± 0.09 for $\widehat{\Delta}SV_{Pre \to 2W,high}(a_1)$, $\widehat{\Delta}SV_{Pre \to 2W,low}(a_3)$, $\widehat{\Delta}SV_{Pre \to 2W,high}(rCBV)$, $\widehat{\Delta}\mu_{Pre \to 2W}(rCBV)$, $\widehat{\Delta}GTV_{Pre \to 2W}$ and $\widehat{\Delta}SV_{Pre \to 2W,high}(K^{trans})$, respectively (Fig. IV.6), indicating the high-a_1 defined subvolume of the tumor had the best performance among the tested variables for predicting responsive tumor. The subvolumes defined by the high-a_1 and low-a_3 classes with the weighting factor $= 0.3$, determined by empirical evaluation of the AUCs (right panel of Fig. IV.6), resulted in the largest AUC, 0.88 ± 0.05. The subvolumes defined by the high-rCBV and high-K^{trans} classes with the weighting factor $= 0.6$ resulted in the AUC of 0.86 ± 0.06.

The statistical analysis of the pair-wise ROC curves revealed that $\widehat{\Delta}SV_{Pre \to 2W,high,high}(\alpha_1, \alpha_3, 0.3)$ was a slightly but not significantly better predictor than $\widehat{\Delta}SV_{Pre \to 2W,high}(a_1)$, and $\widehat{\Delta}SV_{Pre \to 2W,high,high}(rCBV, k^{trans}, 0.6)$, ($p = 0.1$, and $p = 0.4$, respectively). However, it was a predictor significantly better than $\widehat{\Delta}\mu_{Pre \to 2W}(rCBV)$, and $\widehat{\Delta}GTV_{Pre \to 2W}$ ($p = 0.0463$, and $p = 0.02$), respectively. Finally, the predictive value of $\widehat{\Delta}\mu_{Pre \to 2W}(rCBV)$ was slightly but not significantly better than $\widehat{\Delta}GTV_{Pre \to 2W}$ ($p < 0.4$).

IV.C.4 Probability Membership Function Maps

Examples of maps of the probability functions belonging to the class of high-rCBV and high-K^{trans} and the class of high-a_1 and low-a_3, see Fig. IV.5, of a responsive and a stable lesion at Pre-RT and 2W are shown in Fig. IV.7. For the responsive lesion, the voxel probability functions belonging to the high rCBV-K^{trans} class were reduced to almost zero from Pre-RT to 2W, and for the stable lesion the reduction was in a much smaller extent. A similar pattern was also observed for the probability functions belonging to the class of high-a_1 and low-a_3. However, as seen, the latter highlights fewer voxels to the treatment response representing a more specific response-related map.
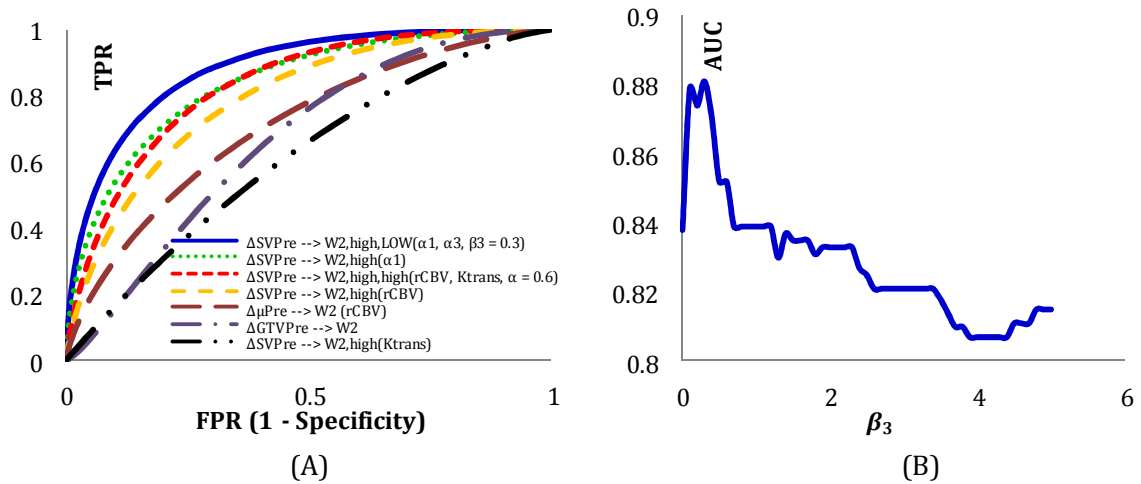
Fig IV.6. Performance of the metrics listed in Table IV.2 in prediction of responsive lesions. (A): ROC curves of the metrics listed in Table 2 for predicting responsive tumors; (B): AUC vs β_3 in Eq. IV.11. FPR: False Positive Rate TPR: True Positive Rate; AUC: Area Under Curve;
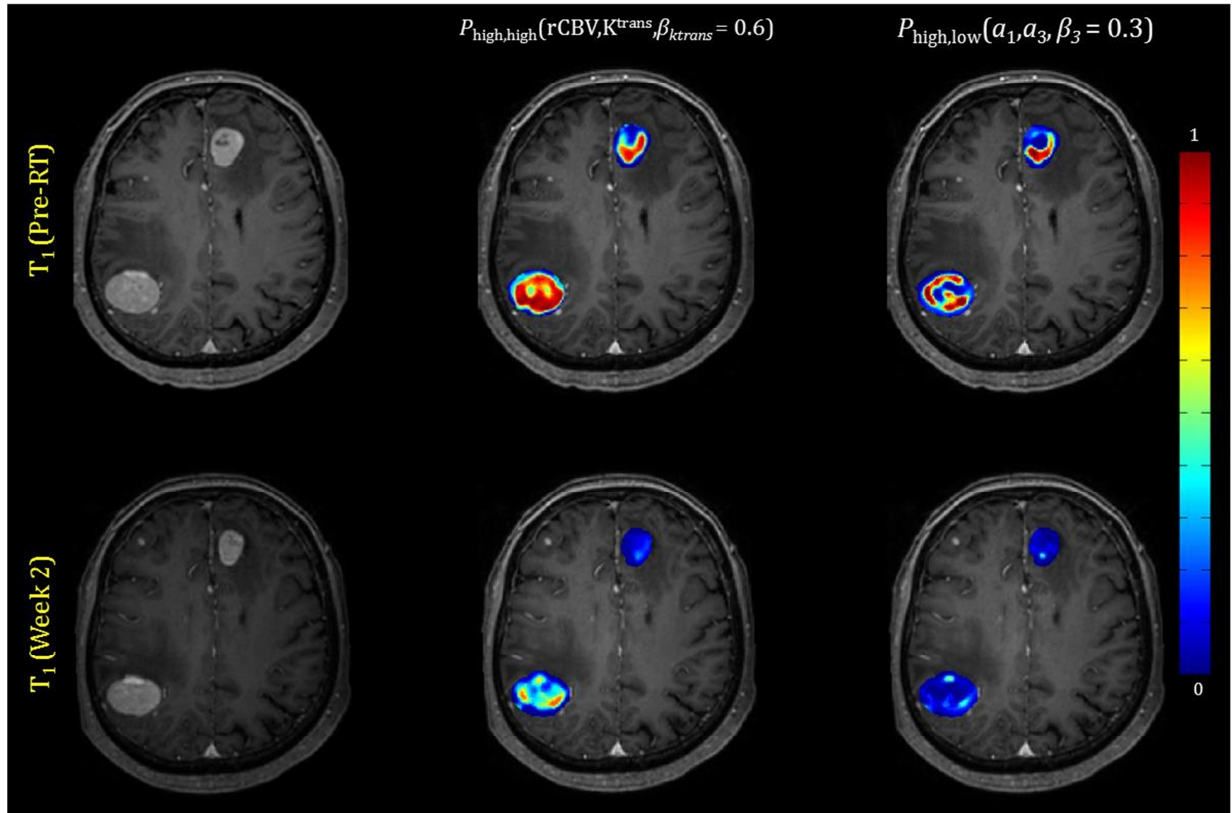
Fig. IV.7. Comparison of the physiological-defined and PCA-defined tumor subvolumes and their longitudinal changes in a responsive and a stable lesion. Top row: Pre-RT T_1 weighted image (left), probability function map of the class with the high-rCBV and high K^{trans} Pre-RT (middle) and probability function map of the class with the high-a_1 and low-a_3 Pre-RT (right). Bottom row: the similar images at 2W. The anterior lesion is responsive and posterior one is stable.

IV.D Discussion

In this study, we proposed a general framework based on principal component analysis (PCA) and a pattern recognition technique for directly delineating the response-driven subvolume of a tumor from the DCE-MRI data. We compared the predictive values of the PC-defined tumor subvolume with the physiological-parameter-defined one (based upon regional cerebral volume (rCBV) and K^{trans}) in the patients who had brain metastases and were treated by whole brain radiation therapy. We found that the two approaches could predict the tumor response to therapy similarly while the PC-defined subvolume can

be delineated more rapidly, which is required for supporting clinical decision making. Overall, our findings indicate that the projection coefficient maps from the first three principal components (PCs) may contain almost all response-related information of the DCE curves. Our further investigation revealed that the first coefficient that is related to the area under the DCE curve is the main factor to determine the response (AUC = 0.83) while the third component (derivative of the enhancement rate) has complimentary information (AUC = 0.88). Our approach had the potential to be an effective tool for supporting real-time decision making.

Our proposed approach to analyze the DCE-MRI data has several advantages in compared with the other model-free techniques which are based on factor analysis [56-57], ICA [58] or extracting characteristic features, such as time to peak or maximum enhancement, from the DCE curves [68]. Foremost, for each tumor type or body site, a set of principal components (PCs) used in calculation of the coefficient maps can be achieved offline and are available before a new patient is scanned. Also, we address the heterogeneous distributions of the principal component coefficients within the tumor by using fuzzy clustering analysis to determine the probability membership functions of classes that the principal component coefficients belong to. Again, this relationship is established offline. Hence, for a new patient scan, computations for the DCE curves only involve in preprocessing the DCE curves, projecting them onto a couple of pre-determined principal components, calculating the histograms of the two projection coefficients in the tumor, and computing the metric given in Eq. IV.10. Computing a couple of principal component coefficients is a much faster process than fitting PK modeling. Our model can be updated when the new patients' data are accumulated, including PCs, the probability

membership functions, and the predictive statistics given in Fig. IV.6(A). Also, re-aligning and reconstructing all DCE curves from all tumors in the DCE-Matrix to determine the PCs, has the potential to overcome the inter-scan variation in the DCE time series. In addition, the set of projection coefficients obtained for each curve is a complete representation of the curve in an N-dimensional feature space wherein the data reduction is performed with the best approximation and without significant concerns regarding the information loss. As shown, almost all response-related information is derived from the first three components. However, for the approaches based on feature extraction, there is no guarantee that the computed features incorporate all relevant information for therapy assessment.

One very important note regarding the proposed methodology is that it is critical to use the arterial input function to normalize the DCE curves. Our investigations showed the enhancement peak of AIF is not linearly correlated with the enhancement peaks of the DCE curves of other tissues, such as normal white matter, gray matter and even veins, indicating intra-patient variation on the peak enhancement. Also, the enhancement peak of AIF manifests great inter-patient variation. It is worthwhile to point out that the projection coefficients (e.g. the first three components) and subsequent delineated subvolume determined by our approach have great tolerances on the temporal resolution and total acquisition time of the DCE curves, while the image acquisition parameters may affect the accuracy of the physiological parameters derived from the PK models [69]. Hence, we may be able to estimate the projection coefficient maps of a tumor accurately using a lower temporal resolution, by which a high spatial resolution can be achieved to delineate the tumor heterogeneity. Further investigation in this regard is ongoing.

IV.E Conclusion

This chapter proposed a general framework for directly analyzing the DCE-MRI data to delineate the response-driven subvolume of a brain metastatic tumor. However, this approach needs to be further validated using an independent dataset. Also, it could be extended and recalibrated to other tumor types, e.g. glioblastoma, for early assessment of tumor response to therapy.

Chapter V

Diffusion Abnormality Index: a New Imaging Biomarker for Early Assessment of Tumor Response to Therapy

V.A Introduction

Several methodologies have been proposed so far to quantify the ADC changes in tumors beyond a change in the mean ADC. The functional diffusion map (fDM)[70-74], probably the most common approach, measures interval changes voxel-to-voxel in a pair of the co-registered ADC images acquired pre and post the start of therapy. The voxels with an ADC change above a threshold are considered as a measure of response. Despite the promising results of the fDM-based approach and its modifications [75], the issue of voxel-to-voxel misregistration, particularly in the region where a tumor volume shrinks or grows during the interval of measurements, is not solved yet. Also, it is important to consider the original ADCs to interpret subsequent changes correctly. Alternatively, analysis of the tumor ADC histogram has been proposed [76-87]. A bi-normal distribution mixture model has shown that the mean value of the low-ADC distribution can predict the therapy response in gliomas [76-78]. Also, changes in mean, skewness and kurtosis of the ADC histogram or the minimum value of the ADC in tumors have been related to survival and the treatment outcome [79-87]. However, these methods have not considered changes in the whole ADC histogram, including both regions with high cellularity and edema, in each

of which a change could reflect a part of the process of a tumor response to therapy. Therefore, it is highly desirable to develop a new methodology for quantifying the tumor ADCs to improve the performance of DW-MRI for therapy assessment.

This chapter describes the development of a diffusion abnormality index (DAI), a new imaging biomarker, to quantify the diffusion abnormality of a brain metastatic tumor for early assessment of tumor response to therapy. The new approach assigns each voxel of the tumor a diffusion abnormal probability according to its ADC value, and then computes the DAI for the tumor. We then tested if an early decrease in the DAI of a tumor could predict therapy response in the patients who had brain metastases and were treated with either whole brain radiotherapy (WBRT) alone or in combination with Bortezomib as a radiation sensitizer.

V.B Materials and Methods

V.B.1 ADC Image Analysis Framework

V.B.1.i Histogram of ADCs in a Tumor

To analyze the ADC distribution in a tumor and a subsequent change during treatment, a histogram of ADCs in a lesion measured at each time point was generated using similar methods explained in the previous chapters. Then, the ADC histogram of each lesion at each scan is normalized to have an area under the histogram equal to one ($\int H(x) = 1$). The ADC histogram of normal tissue ($H_{NT}(ADC)$) is calculated in a similar fashion except the peak normalized to one (Fig. V.1(A)). Compared to the normally distributed ADC histogram of normal tissue, the ADC histogram of a tumor is spread, skewed and/or shifted (Fig. V.1(A)).
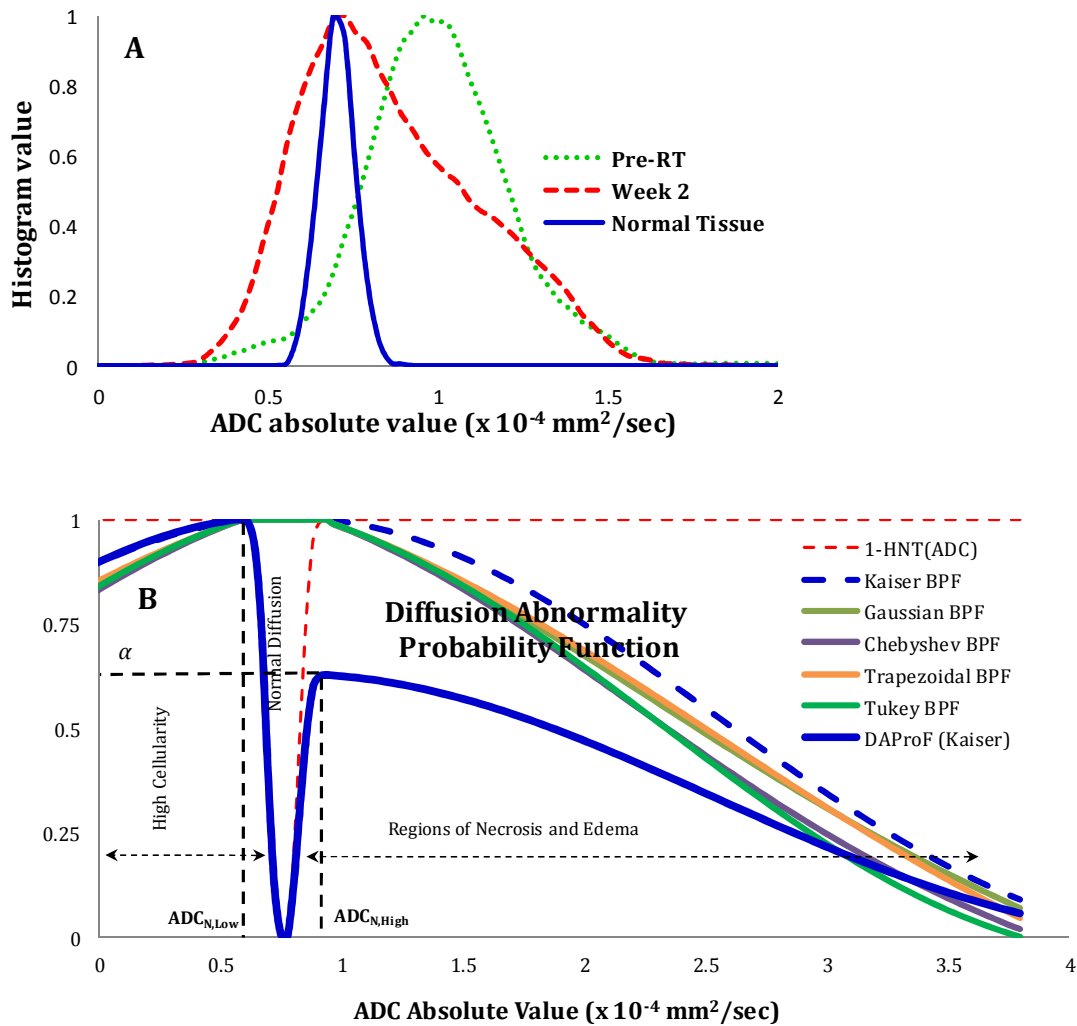
Fig. V.1. Example of a diffusion abnormality probability function (DAProF) for a lesion. (A) ADC histograms in a region of normal white matter (solid), and a progressive brain metastasis prior to treatment (doted) and 2 weeks after starting the treatment (dashed). Peaks of all histograms are normalized to one for visualization. (B) DAPoF of the same tumor (solid). The DAProF is equal to $(1-H_{NT})$ filtered by a band-pass filter and weighted by a factor α (< 1) for high ADCs.

V.B.1.ii Diffusion Abnormality Probability Function

Next, a diffusion abnormality probability function (DAProF) is developed to characterize the whole tumor ADC histogram based upon the normal tissue ADC distribution of each patient. The $H_{NT}(ADC)$ divides the tumor ADC histogram into three segments with low, normal, and high ADCs (Fig. V.1(A)). The first and latter are related to

high cellular density and edema, respectively. Therefore, for each patient, a DAProF can be defined as 1-$H_{NT}(ADC)$, and filtered by a band-pass filter (BPF) centered at the peak of $H_{NT}(ADC_{Norm})$ to reduce noise influence in the computation at two tails where the ADC approaches to positive or negative infinite (or zero) as:

$$DAProF = BPF \cdot \left(1 - H_{NT}(ADC)\right) \qquad \textbf{(Equation V.1)}$$

The 90% confidence interval of $H_{NT}(ADC)$ is used to define the band-width of BPF. Considering that changes in the low-ADC (high cellularity) tumor region could predominantly determine therapy response, a weighting factor α (<1) is used to weight low and high ADC contributions unequally in DAProF$_\alpha$ as:

$$DAProF_\alpha = \begin{cases} DAProF_{Low} = BPF \cdot \left(1 - H_{NT}(ADC)\right) & ADC \leq ADC_{Norm} \\ \\ DAProF_{High} = \alpha \cdot BPF \cdot \left(1 - H_{NT}(ADC)\right) & ADC > ADC_{Norm} \end{cases} \qquad \textbf{(Equation V.2)}$$

The DAProF$_\alpha$ is normalized to one at the peak. Note that DAProF$_\alpha$ is patient-specific. Also, we investigate the role of different BPFs e.g. the Kaiser, Chebyshev, Gaussian, Trapezoidal and Tukey filters in constructing the DAProF.

V.B.1.iii Diffusion Abnormality index

To quantify the extent of diffusion abnormality in a tumor at a specific scan time (τ), a diffusion abnormality index (DAI) is defined as:

$$DAI_\alpha(\tau) = GTV_\tau \cdot \int H_\tau(x) \cdot DAProF_\alpha(x)dx \qquad \textbf{(Equation V.3)}$$

where GTV$_\tau$ and $H_\tau(x)$ denote the gross tumor volume and the tumor ADC histogram at time τ, respectively. A low or high ADC abnormality index can be computed by replacing

DAProF$_\alpha$ by DAProF$_{Low}$ or DAProF$_{High}$ in Eq. V.3. A change in the DAI from pre-RT to 2W is calculated as:

$$\hat{\Delta}DAI_{\alpha,pre\rightarrow 2W} = \frac{DAI_\alpha(2W) - DAI_\alpha(pre-RT)}{DAI(pre-RT)} \cdot 100. \qquad \textbf{(Equation V.4)}$$

In response to a therapy, the ADCs in the region with high cellularity may increase due to cell shrinkage or necrosis [71] and in the region of edema may decrease due drainage of water into tumor cells. However, the ADC change in the region of high cellularity or edema may play a different role for assessment of response, which may depend upon a tumor type and therapeutic regime. Hence, low and high ADC contributions are weighted by α in Eqs V.3 and V.5 while forming a single metric for assessing tumor response to a specific treatment.

V.B.2 Evaluation

V.B.2.i Patient

Twenty four patients who had brain metastases and were treated by WBRT were enrolled in an institutional review board (IRB)-approved prospective MRI study (12 women and 12 men, ages 40-76 years, Table V.1). The histology included melanoma (14), non-small cell lung cancer (6), renal cell carcinoma (1), breast cancer (2), and head & neck squamous cell carcinoma (1). All patients received WBRT with a total dose of 30 Gy (16 patients) or 37.5 Gy (8 patients). Thirteen patients also received Bortezomib during WBRT as a radiation sensitizer. Each lesion was analyzed individually due to intra-patient heterogeneous lesion response to therapy. If a patient had three metastases or fewer, all lesions were included. If a patient had more than three lesions, only the three largest

lesions were analyzed. If a patient had more than three lesions larger than 0.5 cm^3, all lesions larger than 0.5 cm^3 were included. In overall 67 metastatic lesions were included in our dataset 28 of which were treated with radiotherapy alone and the rest were treated with radiotherapy in combination with Bortezomib as a radiation sensitizer.

Table V.1. Patient characteristics information

Pt.	Gender	Age(Y)	Histology	Total accumulated dose/Fx (Gy)	Concurrent Therapy	No. of L.	Tumor Volume Range (cm^3)
1	Female	54	Breast Cancer	37.5/2.5	None	6	0.5 - 11.78
2	Female	60	NSC Lung Cancer	37.5/2.5	None	1	0.52
3	Male	52	NSC Lung Cancer	30/3	None	1	0.479
4	Female	64	NSC Lung Cancer	37.5/2.5	None	1	0.11
5	Male	43	Head & Neck SCC	30/3	None	1	0.60
6	Male	58	NSC Lung Cancer	30/3	None	3	2.38 - 10.69
7	Female	66	NSC Lung Cancer	37.5/2.5	None	1	0.95
8	Female	53	Breast Cancer	30/3	None	4	0.45-8.9
9	Male	40	Melanoma	37.5/2.5	None	3	0.06-1.23
10	Male	58	Melanoma	30/3	None	4	0.48-6.47
11	Female	51	NSC Lung Cancer	30/3	None	3	0.50 - 4.55
12	Male	63	Renal Cell Carcinoma	30/3	Bortezomib	2	13.23 - 14.67
13	Male	41	Melanoma	37.5/2.5	Bortezomib	3	0.15 - 1.24
14	Female	52	Melanoma	37.5/2.5	Bortezomib	1	2.74
15	Female	45	Melanoma	30/3	Bortezomib	1	2.07
16	Male	49	Melanoma	30/3	Bortezomib	2	0.17 - 4.09
17	Male	61	Melanoma	37.5/2.5	Bortezomib	7	0.5 - 17.67
18	Female	55	Melanoma	30/3	Bortezomib	2	0.42 - 0.55
19	Male	76	Melanoma	30/3	Bortezomib	1	0.68
20	Female	46	Melanoma	30/3	Bortezomib	8	0.5 - 1.95
21	Female	57	Melanoma	30/3	Bortezomib	2	0.94 - 1.58
22	Male	60	Melanoma	30/3	Bortezomib	3	0.18 - 1.31
23	Female	74	Melanoma	30/3	Bortezomib	4	0.69 - 5.81
24	Male	67	Melanoma	30/3	Bortezomib	3	0.62-11.10

Abbreviation: Pt. = patient; Y = year; NSC = non-small cell; SCC = squamous cell carcinoma; No. of L. = number of lesions; and Fx=fraction size.

V.B.2.ii Image Acquisition and Pre-processing

All patients had MRI scans on a Philips 3T scanner prior to radiotherapy (Pre-RT), 2 weeks after the start of RT (2W), and 1 month after the completion of treatment (1M Post-

RT). MRI scans included pre and post Gd-DTPA volumetric T1-weighted images, 2D T2-weighted images, and diffusion-sensitive images. The diffusion weighted images were acquired using a spin-echo echo-planar imaging sequence (TR/TE = 2636/46 msec) with b_0= 0, and diffusion weighting along three orthogonal directions and b_1 = 1,000 sec/mm^2 to calculate the ADC images.

Using an in-house software package, all ADC images were co-registered to pre-RT post-Gd T1-weighted images by rigid transformation and mutual information to have a voxel size of 0.94 x 0.94 x 3 (mm^3). After each lesion of interest was contoured on the post-Gd T1 weighed images obtained pre-RT, 2W and 1M post-RT by a physician, the tumor volumes were transferred onto the ADC maps obtained at the same time point. The necrotic regions of the lesions were also contoured, and excluded from analysis. For each patient, a volume of 3-4 cc of normal white matter or cerebellum tissue, depending upon the location of the tumor of interest, was contoured on the pre-RT post-Gd T1-weighed images and transferred onto the pre-RT ADC map to obtain a distribution of normal ADCs.

V.B.2.iii DAI for Prediction of Response

Endpoint. Given that previous studies indicate that brain metastases exhibit little pseudo-response and pseudo-progression one month after RT [49], a percentage change in the gross tumor volume (GTV) from Pre-RT to 1 month post RT, $\hat{\Delta}GTV_{Pre \rightarrow 1M\ post}$, was used as a measure of tumor response to therapy. From Pre-RT to 1M Post-RT, of the 27 lesions treated with radiotherapy alone, 15 had a decrease in the GTV of at least 25%, defined as responsive, 7 had an increase of at least 25%, defined as progressive, and the remaining 6

were defined as stable. For the 39 lesions treated by radiotherapy in combination with Bortezomib, 10 lesions were responsive, 13 lesions were progressive and 17 were stable.

Predictive Model. First, we used the lesions in each treatment group to optimize α (< 1) in $\hat{\Delta}DAi_{\alpha,pre-RT \to 2W}$ by maximizing the group difference between the responsive and progressive lesions using Mann-Whitney U Test. Using the optimal value of α, we further tested if $\hat{\Delta}DAi_{\alpha,pre \to 2W}$ could differentiate responsive from stable tumors, and stable from progressive tumors in both treatment groups. A *p*-value < 0.05 was considered as significance. Next, we tested sensitivity and specificity of $\hat{\Delta}DAi_{\alpha,pre \to 2W}$ for predicting non-responsive tumors, including both progressive and stable tumors by *Receiver Operating Characteristic* (ROC) analysis (software package ROCKIT) [50]. Also, we compared the performance of $\hat{\Delta}DAI$ for predicting post-treatment response with the ADC metrics previously published by others, such as a mean of the low ADC distribution from the bi-normal ADC distribution mixture model [76-78] and skewness and kurtosis of tumor ADC distributions [80], and conventional metrics, such as a percentage change in the GTV, pre-treatment minimum ADC, a minimum ADC change and a change in the mean of tumor ADCs from pre-RT to 2W. The significant difference of the area under ROC curves (AUC) between the metrics were compared by *t*-test, for which the standard errors and the difference between the two AUCs were calculated by the method proposed by DeLong et al. [51]. We also used the leave-one-out technique to measure the prediction risk of $\hat{\Delta}DAI$.

V.C Experimental Results

V.C.1 Association of DAI with Response

The best separation of the group difference between the responsive and progressive tumors resulted in α values of {0.7, 0.65, 0.65, 0.625, and 0.6} and {0.2, 0.2, 0.125, 0.15 and 0.175} for lesions treated with radiotherapy alone and in combination with Bortezomib as a radiation sensitizer and for Kaiser, Gaussian, Chebyshev, Trapezoidal and Tukey band-pass filters, respectively. The results primarily suggest that a decrease in abnormality associated with low-ADCs could be a predominant indicator for tumor response to therapy compared to a decrease in abnormality with high-ADCs. Also they reveal secondarily that a decrease in abnormality associated with high-ADCs (edema) may be interpreted differently in determining the response of a tumor to various treatments. For lesions treated with radiotherapy alone, from Pre-RT to 2W, $DAI_{0.7}$(Kaiser) showed a significantly greater decrease in the responsive tumors than the stable lesions ($p < 0.0045$), Table V.2, and the progressive ones ($p < 0.0002$), or the non-responsive tumors (including both progressive and stable ones) ($p < 0.00004$). The results show that choosing different band-pass filters does not change the results significantly. Among the other metrics, the percentage decrease in the GTV from Pre-RT to 2W in the responsive group differed significantly from the stable group ($p < 0.0265$), the progressive group ($p < 0.0004$), and the group of combining the progressive and stable tumors ($p<0.0003$). The performances of the other metrics for differentiation of responsive, stable and progressive lesions are summarized in Table V2. As seen, skewness could differentiate between the responsive and progressive lesions and the percentage but change in GTV and DAI performed the best among all metrics for group differentiation in lesions treated with radiotherapy alone. For lesions treated with

radiotherapy combined with Bortezomib, none of the metrics except for DAI was able to differentiate between the responsive and progressive lesions ($p < 0.02$), see Table V.3. The DAI classifies the responsive and stable lesions similarly when Bortezomib was used as a radiation sensitizer. Also, Table V.3 show that the Kaiser, Gaussian and Tukey band-pass filters performed better than the other filters. Hence, for the rest of this chapter, we use the Kaiser filter to report the results. Finally, Fig V.2 shows the box plots summarizing the performance of the significant metrics (ΔSkewness, ΔKurtosis, ΔGTV and ΔDAI) listed in Tables V.2 and V.3 for differentiating responsive, stable and progressive lesions treated with radiotherapy alone and in combination with Bortezomib, respectively.

Table V.2: Association of the different diffusion metrics with response in lesions treated with whole brain radiotherapy alone

Metric (Pre-RT->Week2)	Lesion Response Group			
	R vs. S	S vs. P	R vs. P	R vs. {S & P}
	p-value			
ΔSkewness	0.2933	0.4452	0.0289	0.0382
ΔKurtosis	0.4137	0.7308	0.0668	0.0883
$\Delta\mu$	0.2933	0.6282	0.5728	0.3109
ΔMin	0.3305	0.1375	0.2903	0.9266
Min_{PreRT}	0.5593	0.2343	0.7780	0.8901
ΔLow-ADC (BNGM)	0.0391	0.2343	0.6282	0.3109
Low-ADC$_{PreRT}$ (BNGM)	0.0942	0.0350	0.3595	0.7125
ΔGTV	0.0265	0.0047	0.0004	0.0003
ΔDAI$_{0.7}$(Kaiser)	0.0045	0.0047	0.0002	0.00004
ΔDAI$_{0.65}$(Gaussian)	0.0045	0.0047	0.0002	0.00003
ΔDAI$_{0.65}$(Chebyshev)	0.0057	0.0023	0.0002	0.0001
ΔDAI$_{0.625}$(Trapezoid)	0.0057	0.0047	0.0002	0.0001
ΔDAI$_{0.6}$(Tukey)	0.0045	0.0047	0.0002	0.00004

The group differences between responsive, stable and progressive tumors treated with radiotherapy. For each metric, the absolute or percentage change from pre-RT to week 2 were evaluated and the best performance is reported. The black rows show significant metrics. Δ = Change from Pre-RT to Week 2; μ = mean of tumor ADC; Min = minimum; Low-ADC (BNGM) = the mean of the low ADC distribution in the bi-normal Gaussian mixture model [76-78]; GTV = gross tumor volume; DAI = diffusion abnormality index; R = responsive; S = stable; P = progressive;

Table V.3: Association of the different diffusion metrics with response in lesions treated with whole brain radiotherapy in combination with Bortezomib as a radiation sensitizer

| Metric (Pre-RT->Week2)	Lesion Response Group			
	R vs. S	S vs. P	R vs. P	R vs. {S & P}
	p-value			
ΔSkewness	0.4768	0.9825	0.4382	0.3940
ΔKurtosis	0.8952	0.7756	0.7330	0.7846
$\Delta\mu$	0.4768	0.8780	0.8768	0.5956
ΔMin	0.1331	0.5249	0.2778	0.1348
Min_{PreRT}	0.5800	0.6770	0.6869	0.5735
ΔLow-ADC (BNGM)	0.6542	0.6770	0.7802	0.6641
Low-ADC$_{PreRT}$ (BNGM)	0.5800	0.9476	0.8259	0.6877
ΔGTV	0.9370	0.0756	0.1628	0.5096
ΔDAI$_{0.2}$(Kaiser)	0.2572	0.0300	0.0101	0.0411
ΔDAI$_{0.2}$(Gaussian)	0.2572	0.0239	0.0120	0.0444
ΔDAI$_{0.125}$(Chebyshev)	0.3845	0.0132	0.0143	0.0692
ΔDAI$_{0.15}$(Trapezoid)	0.3295	0.0168	0.0170	0.0644
ΔDAI$_{0.175}$(Tukey)	0.2572	0.0149	0.0120	0.0444

The group differences between responsive, stable and progressive tumors treated with radiotherapy. For each metric, the absolute or percentage change from pre-RT to week 2 were evaluated and the best performance is reported. The black rows show significant metrics. Δ = Change from Pre-RT to Week 2; μ = mean of tumor ADC; Min = minimum; Low-ADC (BNGM) = the mean of the low ADC distribution in the bi-normal Gaussian mixture model [76-78]; GTV = gross tumor volume; DAI = diffusion abnormality index; R = responsive; S = stable; P = progressive;

Whole brain radiotherapy
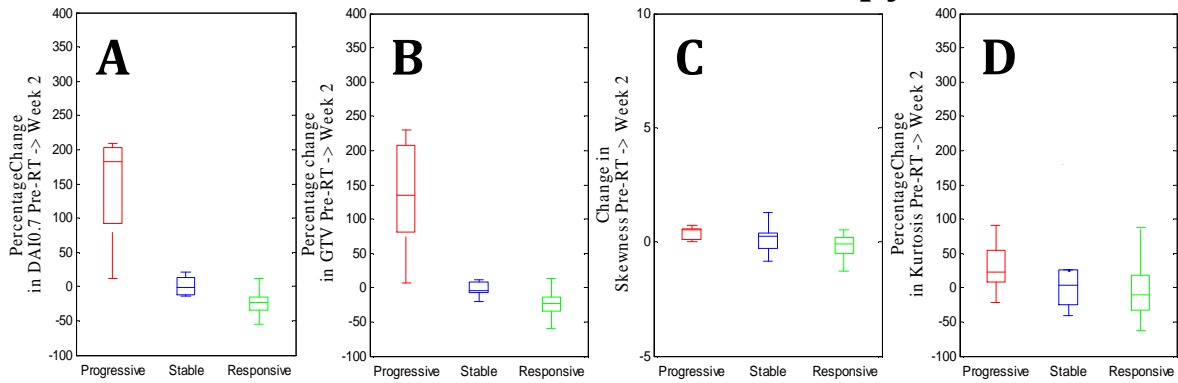
Whole brain radiotherapy combined with Bortezomib
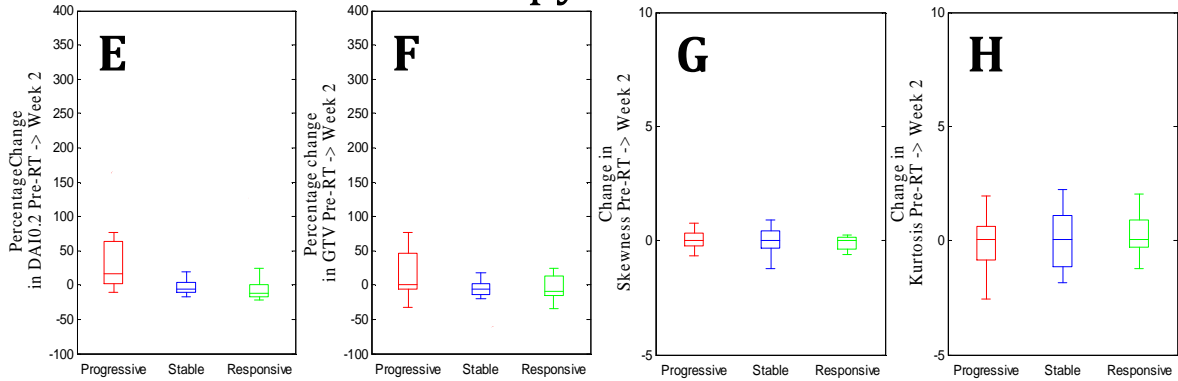
Fig. V.2. Box plots of ΔDAI (A and E), ΔGTV (B and F), ΔSkewness (C and G) and ΔKurtosis (D and H) for responsive, stable and progressive lesions treated by WBRT alone (top) or in combination with Bortezomib as a radiation sensitizer (bottom). The top row shows that ΔGTV and $\Delta DAI_{0.7}$ differentiate the responsive lesions from the stable and progressive ones treated by WBRT while $\Delta DAI_{0.2}$ differentiate the responsive and stable lesions from the progressive ones when Bortezomib is used as a radiation sensitizer.

V.C.2 Performance of the DAI for Prediction of Response

We evaluated the performance of the significant or marginally significant metrics in Tables V.2 and V.3, such as ΔDAI, ΔGTV, ΔSkewness, and ΔKurtosis, for prediction of non-responsive tumors post-RT for both treatments. When lesions treated with radiotherapy alone, the ROC analysis showed that the AUC was 0.96 ± 0.04 (±SEM), 0.91 ± 0.06, 0.64 ± 0.1, and 0.71 ± 0.1 for $\Delta DAI_{0.7}$, ΔGTV, ΔSkewness, and ΔKurtosis, respectively (Fig.

V.3(A)). A pair-wise comparison of the ROC curves of the two metrics revealed that $\Delta DAI_{0.7}$ is a predictor significantly better than ΔGTV ($p < 0.02$), suggesting the physiological change occurs prior to the morphological change. When Bortezomib was used as a radiation sensitizer, the AUC was of 0.70 ± 0.09 ($\pm$SEM), 0.57 ± 0.08, 0.61 ± 0.1, and 0.52 ± 0.1 were achieved for $\Delta DAI_{0.2}$, ΔGTV, $\Delta Skewness$, and $\Delta Kurtosis$, respectively (Fig. V.3(B)). Finally, the leave-one-out analysis resulted in $\alpha = 0.7 \pm 0.0 \, (SEM)$ and $\alpha = 0.19 \pm 0.02$ for radiotherapy alone and in combination with Bortezomib, respectively, indicating that there is no significant bias in the α value selection and also that α is a treatment-specific and even disease-specific parameter in the DAI.
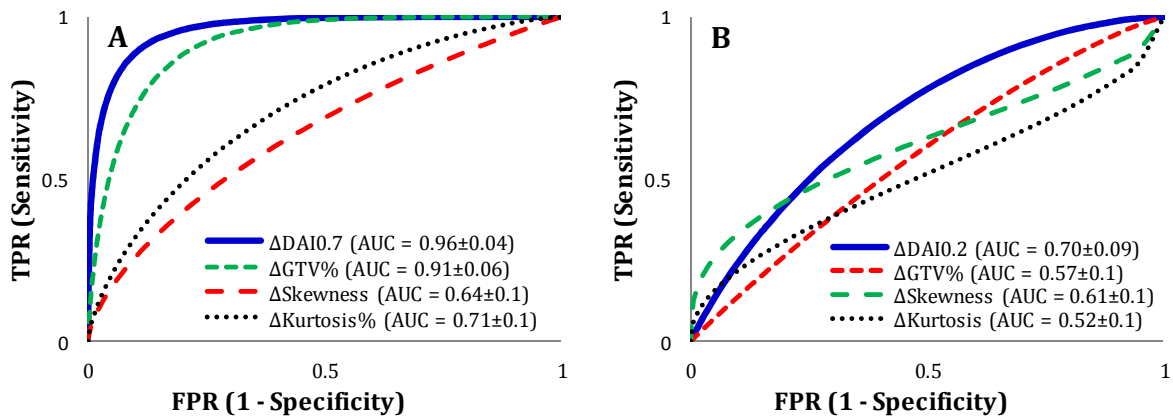
Fig. V.3. ROC curves of metrics ΔDAI, ΔGTV, $\Delta Skewness$, and $\Delta Kurtosis$ for predicting non-responsive tumors (including both stable and progressive tumors) treated with radiotherapy alone (A) and in combination with Bortezomib as radiation sensitizer (B).
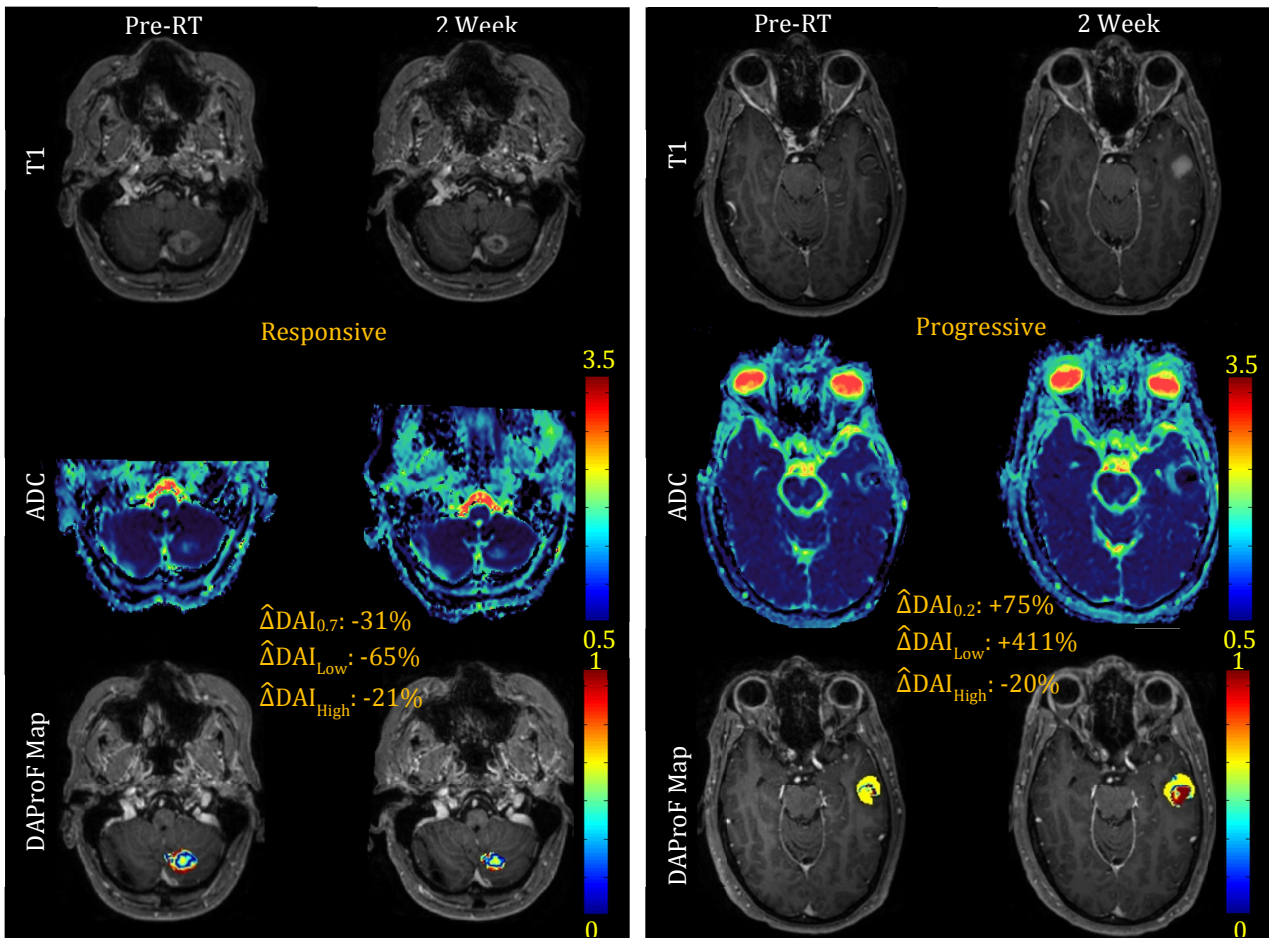
Fig. V.4. Example of changes in tumor cellularity map in a responsive and a progressive lesion. Top rows: T1- weighted images at Pre-RT and 2W, Middle rows: ADC maps at Pre-RT and 2W, and Bottom rows: maps of diffusion abnormality probability functions at Pre-RT and 2W. The images of a responsive case (with a volume of 3.7cc) are depicted in two left columns and the images of a progressive one (with a volume of 4.1cc) are represented in two right columns. From Pre-RT to 2W, the diffusion abnormality index (DAI) decreased ~31% for the responsive lesion, and increased ~16% for the progressive one. For the responsive lesion, treated by radiotherapy alone, α = 0.2 but for the progressive lesion where Bortezomib was used α = 0.7.

V.C.3 DAProF Map

Examples of maps of the ADC and the diffusion abnormality probability function, DAProF, for a responsive lesion, treated with radiotherapy alone, and a progressive one, treated with radiotherapy in combination with Bortezomib, at Pre-RT and 2W are shown in Fig. V.4. From Pre-RT to 2W, the DAI decreased ~31% for the responsive lesion but

increased ~75% for the progressive one. For the responsive lesion, the DAIs associated with low and high ADCs decreased approximately 65% and 21%, respectively. For the progressive lesion, the DAI associated with low ADCs increased 411% but the one associated with high ADCs decreased 20%.

V.D Discussion

In this chapter, a diffusion abnormality index was developed based upon diffusion weighted magnetic resonance imaging for early assessment of tumor response to therapy. The development of the DAI considers underlying physiology of abnormal ADCs in a tumor, including both high cellularity and edema, and a patient-specific abnormal diffusion probability. The DAI weights the abnormal ADC contributions from high cellularity and edema differently for predication of therapy response. The performance of DAI was evaluated in patients who had brain metastases and were treated by either whole brain radiotherapy (WBRT) alone or in combination with Bortezomib as a radiation sensitizer. Comparing with other ADC metric published previously and conventional metrics, the DAI was the best one for predicting volumetric response of brain metastases to radiotherapy. Also, our results indicate that the diffusion-related physiological change in the tumor occurs earlier than the morphological change in response to radiotherapy. The DAI developed and tested in this study could be also applied to other tumor types and treatment regimens after recalibration, e.g., glioblastoma and head and neck cancers, and anti-angiogenesis therapy, and has a potential to be a robust imaging biomarker for early assessment of therapy response and outcome.

In the development of the DAI, we found that the weighting factor, α, is different for different treatments or tumor types. For instance, when brain metastases were treated with WBRT, the changes in abnormality associating with high-ADCs contributed substantially for response assessment. In this case, both a decrease in cellularity and a decrease in edema could be an indicator for treatment response. However, when Bortezomib was used as a radiation sensitizer with WBRT to treat melanoma metastases to the brain, we realized that a decrease in abnormality associating with high-ADCs is less important for response assessment. Also, we found that for assessment of response of melanoma metastases treated by WBRT with Bortezomib, the performance of all tested ADC metrics, including the DAI, were worse than the metastases that were not from melanoma and treated by WBRT alone. This could be due to the nature of melanoma, high vascularity, edema and hemorrhage, and the effect of Bortezomib on the lesion [88-89]. Since Bortezomib could alter vascular properties of the tumor, a change in vascular characteristics of the tumor could be an important part of tumor response to therapy, and hence a perfusion change could be added into the DAI to improve response assessment. This hypothesis will be tested in the future. Our findings also suggest that the DAI could be used to assess a specific treatment effect on a specific tumor. For an anti-angiogenesis treatment to brain tumor, e.g., glioblastoma, a high ADC abnormality reduction indicates the treatment effect on the abnormal leaky vasculature but a low ADC abnormality decrease suggest the effect on the tumor.

The diffusion abnormality index proposed in this study has several advantages in comparison with functional diffusion map [70-74. Foremost, the diffusion abnormality index does not rely on voxel-to-voxel image registration accuracy, which the fDM-based

92

analysis solely depends upon. Hence, anatomical alteration of a tumor after starting therapy, e.g., a change in edema, or surgical cavity, and/or tumor growth or shrinkage, does not have an adverse effect on the DAI. In addition, we incorporate the tumor volume into the DAI, and thus a change in the DAI represents both physiological and morphological changes in a tumor, which could increase sensitivity of the DAI for tumor response to therapy. Furthermore, the fDM-based analysis only considers an absolute change in the ADC [70], regardless of the origin of the ADC, whereas an increase or a decrease in the low or high ADC region has a very different underlying implication. An ADC increase in the region with abnormal low diffusion and a decrease in the region with abnormal high diffusion both are positive indications for a tumor response to therapy, thereby accounted for in the DAI. Also, it is important to point out that although a change in the DAI of a tumor does not depend upon voxel-level accuracy of registration of images acquired pre and after the start of therapy, spatial information of diffusion abnormality of a tumor is available at any given measurement (Fig. V.4), which could be used for visualization or provide guidance for intensified treatment.

The DAI also has also several advantages in comparison with other histogram-based approaches [76-87]. In some of these techniques [76-78], only the low-ADC portion of the tumor histogram is used for therapy assessment. We have shown that a reduction in the abnormal high ADC in the edema region is also an important indicator for response prediction. Hence, combining the changes in both abnormal low and high ADC regions has the potential to produce a better predictor for assessing response to various treatments. The indices based upon the skewness and kurtosis of the tumor ADC histogram [80-81]

93

neglect diffusion physiology in a tumor, and may not be able to capture the complex change patterns in a heterogeneous tumor for response assessment.

V.E Conclusion

In this chapter, the diffusion abnormality index was demonstrated as a new imaging biomarker for assessment of brain metastasis response to WBRT. However, the DAI needs to be further validated using an independent dataset. Also, the DAI could be extended to other tumor types, e.g. glioblastoma, for early assessment of tumor response to therapy. Furthermore, the value of DAI in assessing the tumor response to therapy can be integrated to other metrics developed in this dissertation for providing better response-predictor. In the next chapter, we briefly show our initial thought and the preliminary results in how we plan to combine the metrics explained in this dissertation.

<center>**Chapter VI**</center>

<center># Conclusion and Future Works</center>

VI.A Overview

In this dissertation, we focused our attentions on improving the detection of brain metastases and assessing their early response to radiation therapy (RT). We initially discussed the difficulties of manually screening of the post-Gd T1-weighted magnetic resonance images (MRI) in diagnosis of brain metastases and then described the drawbacks of the currently available computer-aided detection (CAD) systems for automatic detection of brain metastatic lesions. Next, we explained our proposed CAD system to overcome these limitations. In the second part of this dissertation, we briefly noticed that whole brain radiation therapy (WBRT), a routine treatment for brain metastases, could produce a decrease in neurocognitive status compared to stereotactic radiosurgery (SRS) and therefore, more patients are receiving focal treatment for brain metastases. Hence, the needs for developing a tool to early assess the brain metastasis response to therapy are becoming more and more important as patients receive more and more focal therapy. Next, we described the development of new imaging biomarkers for early assessment of brain metastases to radiation therapy by quantification of the changes in brain metastasis vascular and cellularity properties using imaging measurements related to dynamic contrast enhanced (DCE) and diffusion-weighted (DW)-MRI. In this chapter, we

<center>95</center>

primarily aim to review our achievements in each part and then specify the direction for the future works accordingly.

VI.B CAD system for detection of brain metastatic lesion

Our investigations revealed that neuroradiologists may miss about 20%-40% of brain metastases with a diameter <5mm in a routine clinical screening and therefore, the CAD systems could assist in locating such lesions. However, we have seen that the performance of the previously proposed template-matching based CAD system for detection of brain metastases [37] is limited mainly due to production of large number of false positives and its fairly low sensitivity specially in locating the small lesions. Hence, using a more robust template and optimizing the size and the number of the required templates, we aimed to increase the sensitivity of our proposed CAD system. Furthermore, we proposed a lesion enhancement strategy and a series of rule-based criteria to reduce the number of false positives. In our experiment, we achieved a sensitivity of 93.4% with an intra-cranial false positive (ICFPR) rate of 0.024 in compared to a sensitivity of 87% and an ICFPR of 0.22 obtained for the CAD system proposed in [37].

In our investigation, we realized that the main reasons for the lesions to be missed by our proposed method is due to attachment to another structure, especially in the midline of the brain, or to have a low contrast to intensity variation ratio (CIVR). In the former case, we discussed that segmenting vessels from tissues in the midline could be helpful, e.g., using publically-available software of SPM [43]. This could be implemented in the future version of this work. Also, we realized that although our proposed nodule enhancement strategy improves both sensitivity and specificity of our proposed CAD

system, developing a technique to locally adapt the CIVR could further improve the performance of our proposed CAD system. A strategy to deal with a lesion near a vessel could be also helpful and can be addressed in the future. In addition, further reduction of the extra-cranial false positives can be achieved by using a skull stripping technique [42], and can be incorporated into a final CAD package in the future. Also, the impact of the CAD system on the overall patients' survival and the treatment outcome could be a subject of a clinical study down the road.

VI.C Physiological imaging driven response assessment of brain metastases to radiation therapy

In the previous chapters, we mentioned that the assessment of tumor response to therapy is conventionally done by measuring the longitudinal changes in tumor volume which may occur several months after treatment is completed. However, we further described that changes in tumor physiology, which could happen earlier and even during the course of treatment, have the potential to provide a means to predict tumor response to therapy ahead of time and also may provide a tool for therapy guidance. Hence, in this dissertation, we focused on two important aspects of the treatment effect on the tumor physiology for response assessment: 1- changes in tumor vascular properties and angiogenesis process, and 2- changes in tumor cellularity properties and tumor cells' death. In the rest of this chapter, we briefly review our achievements in each aspect and then discuss the direction for the future studies.

In chapter III of this dissertation, we described that dose painting/sculpting of a tumor based on the biological target volume has the potential to improve the local control or even outcome, [45] and then proposed an image analysis framework to delineate the biological target volume based upon the imaging-defined "phenotype" subvolumes of a tumor with high regional cerebral blood volume (rCBV) and Gd-DTPA transfer constant from blood plasma to tissue (K^{trans}), derived by fitting a pharmacokinetic (PK) model to the dynamic contract enhanced (DCE) curve of each tumor voxel. We showed that a percentage decrease in the tumor subvolumes with high rCBV and K^{trans} from Pre-RT to 2 weeks after the start of RT provides a metric to predict volumetric tumor response one month after RT significantly better than the changes in gross tumor volume (GTV) observed during the same time interval, and hence could be a candidate as a radiation boost target. However, we mentioned that to improve the performance of the proposed metric (from AUC=0.86), our general approach can be further used to test whether including other physiological imaging parameters into analysis, e.g. apparent diffusion coefficient (ADC), can improve the prediction of tumor response to therapy. Furthermore, in the chapter IV, as a complimentary part, we mentioned that deriving the physiological parameter maps, e.g. rCBV and K^{trans}, by fitting a PK model to DCE curves is time consuming and may involve a series of uncertainties. Hence, we proposed a PK model-free approach based upon principle component analysis (PCA) to delineate the response-driven subvolumes of a tumor directly from the DCE curves. We found that the first three principle components contain almost all response-related information of the DCE curve matrix. We observed that while the first principle component, related to the area under of the DCE curve, is the main factor to determine response, the third component, related to the first

derivative of the DCE curve, has a complimentary role. We also observed that both physiological-defined and PCA-defined subvolumes of a tumor could predict the response to therapy similarly while the PCA-defined subvolume can be derived more quickly.

In chapter V, we described a diffusion abnormality index (DAI) to quantify the abnormality of the tumor cellularity properties in compared to normal tissue. The normal tissue ADC histogram ($H_{NT,ADC}$) divided the tumor ADC histogram into 3 categories: low (high cellularity), normal, and high (edema and necrosis) ADC. A diffusion abnormality probability function (DAProF) of the tumor was then defined by 1-$H_{NT,ADC}$ and band-pass filtered to reduce noise influence at the two tails and a weighting factor (α) was used to weight the low-ADC subvolume, $SV_{low}(ADC)$, related to high-ADC subvolume, $SV_{high}(ADC)$, differently. The DAI was finally achieved as an integral of the DAProF$_\alpha$-weighted tumor ADC histogram. The change in DAI quantified the effect of treatment on the tumor cellularity over time and was used to evaluate the response of brain metastases in patients treated by either whole brain radiation therapy (WBRT) alone or combined with Bortezomib as a radiation sensitizer. In our experiments, we found that the best separation of group difference between responsive and progressive lesions resulted in α values of 0.7 and 0.2 for the groups of patients treated with WBRT alone and WBRT combined with Bortezomib, respectively, suggesting that a decrease in $SV_{high}(ADC)$ may have a different role in response assessment, depending on the treatment regimen and the tumor type, and also the change in $SV_{low}(ADC)$ could have a higher impact for determining response. In lesions treated with WBRT alone, we found that both a decrease in high cellularity and a decrease in edema could be an indicator of treatment response. However, when WBRT was combined with Bortezomib to treat melanoma metastases to the brain, we realized that a

99

decrease in $SV_{high}(ADC)$ is less important for response assessment. Also, we found that in this case, the performance of all tested ADC metrics, including the DAI, were worse than the metastases that were not from melanoma and treated by WBRT alone. We mentioned that since Bortezomib could alter vascular properties of the tumor, a change in vascular characteristics of the tumor could also be an important part of tumor response to therapy, and hence a perfusion change could be added into the DAI to improve response assessment. This hypothesis is preliminarily tested and will be extensively investigated in the future. The preliminary results are given in the following paragraphs.

In chapter III, we showed that changes in the subvolumes of brain metastases with high rCBV and K^{trans}, $SV_{high}(rCBV,K^{trans})$, could be an early indicator of tumor response to RT. Also, we have seen in chapter V that changes in tumor subvolume with low ADC, $SV_{low}(ADC)$, may have a greater impact on determining tumor response to therapy. Hence, all these together indicate the changes in subvolumes of a tumor with either high rCBV and K^{trans} or low ADC, $\Delta[SV_{high}(rCBV,K^{trans}) + SV_{low}(ADC)]$, could be a better response predictor. Therefore, using the same lesions used in chapter V, we tested this hypothesis. We found that in lesions treated with WBRT combined with Bortezomib, $\Delta[SV_{low}(ADC) + SV_{high}(rCBV,K^{trans})]$ showed a significantly greater decrease from pre-RT to 2W in the responsive lesions than the stable ones ($p<0.0003$), the progressive tumors ($p< 0.00002$), or the non-responsive ones {responsive + stable lesions} ($p<0.00004$). In Fig. VI.1, the performance of the new metric is compared with ΔDAI and some conventional metrics such as changes in the gross tumor volume (GTV), and the changes in the means of the tumor ADC, rCBV and K^{trans} within the same time interval for prediction of non-responsive lesions. In ROC analysis, the area under curve (AUC) of 0.96 ± 0.03 was obtained for $\Delta[SV_{low}(ADC) +$

$SV_{high}(rCBV,K^{trans})]$ in prediction of the non-responsive lesions treated with WBRT combined with Bortezomib. In lesions treated with WBRT alone, $\Delta DAI0.7$ performed well (AUC = 0.96 ± 0.04) and $SV_{high}(rCBV,K^{trans})$ did not add discriminatory information. This indicates that while the changes in tumor subvolumes with different tumor cellularity properties could determine response in RT alone, the change in vascular properties is also an important indicator for response when Bortezomib is used as a radiation sensitizer.
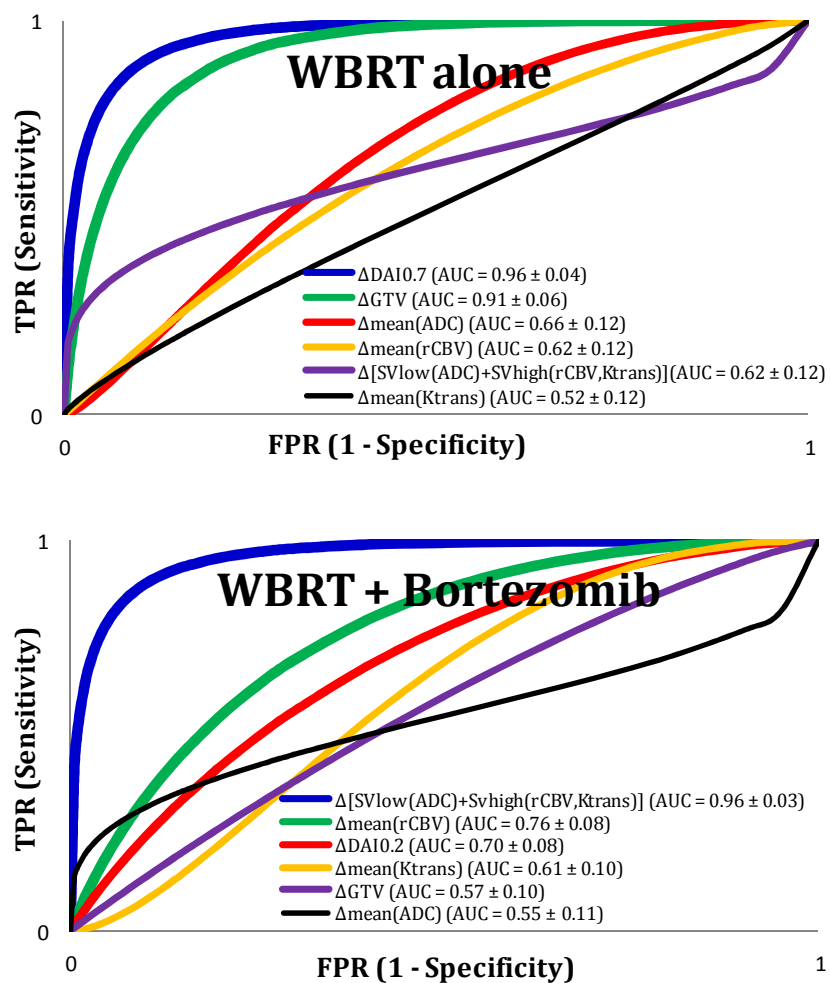
Fig. VI.1. ROC analysis for prediction of non-responsive lesions treated with either whole brain radiation therapy alone (top) or combined with Bortezomib as a radiation sensitizer (bottom). As shown, the areas under curve (AUCs) of 0.96 ± 0.04 (WBRT alone) and 0.96 ± 0.03 (WBRT + Bortezomib) were obtained in prediction of non-responsive lesions for $\Delta DAI_{0.7}$ and $\Delta[SV_{low}(ADC) + SV_{high}(rCBV,K^{trans})]$, respectively.
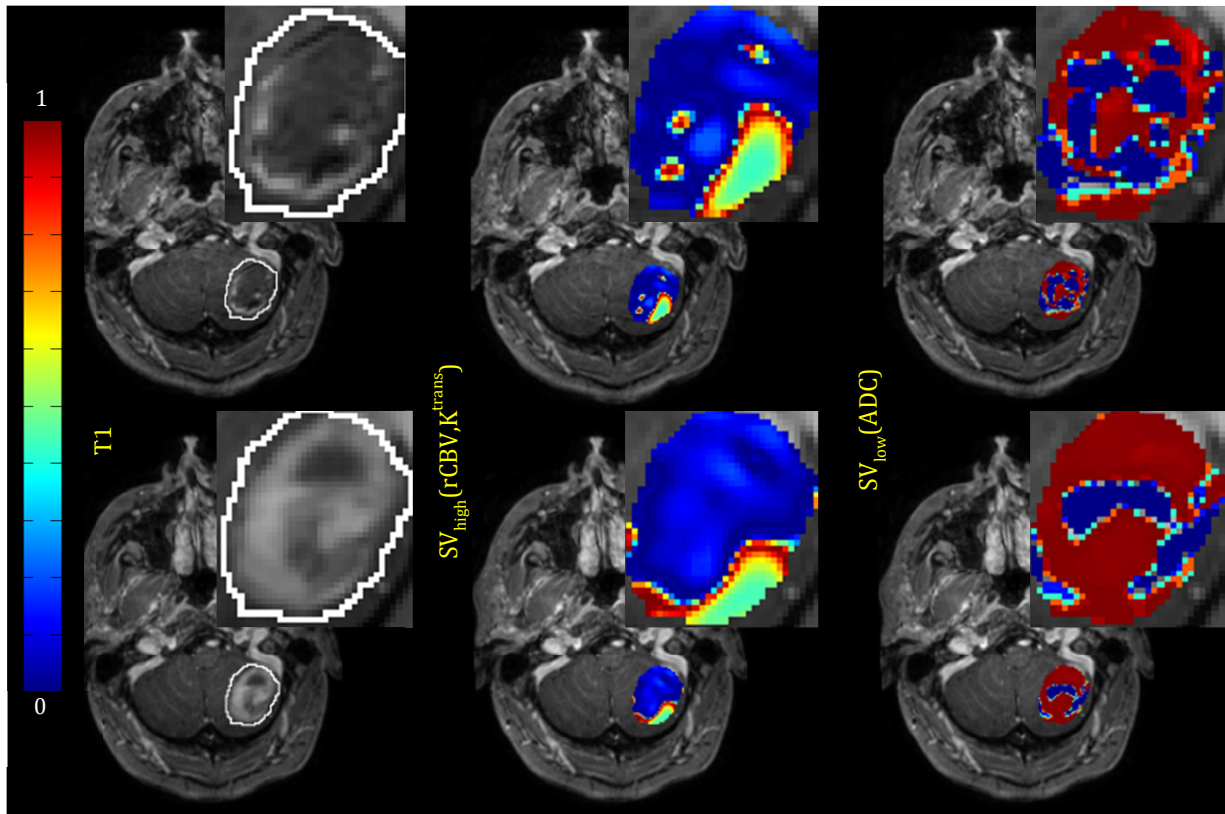
Fig. VI.2 Example of changes in tumor vascular and cellular maps in a non-responsive tumor with a volume of 14.6 cm^3. Although SV_{high}(rCBV,K^{trans}) decreased 24% from Pre-RT to 2W (2nd column), SV_{low}(ADC) increased 76% in the same time interval (3rd column) resulting in an overall increase of 61% in both subvolumes. ΔGTV was changed approximately 0.2% during the same period. The color code denotes the probability of a voxel belonging to SV_{high}(rCBV,K^{trans}) or SV_{low}(ADC) in the 2nd and 3rd column, respectively.

As an example, Fig. VI.2 shows the changes in tumor vascular and cellularity maps in a non-responsive tumor, with a volume of 14.6 cm^3, at pre-RT (top) and 2 weeks (bottom) after the start of RT. Although SV_{high}(rCBV, K^{trans}) decreased 24% from Pre-RT to 2W (2nd column), SV_{low}(ADC) increased 76% in the same time interval (3rd column), resulting in 61% increase in the sum of the subvolumes. The tumor subvolumes that are associated with poorer response to therapy could be considered as a target volume for intensified treatment.

The results of the multi-parametric analysis suggest that tumor response to a therapy is a complex process and should be evaluated from different standpoints. Also, it indicates that response process varies depending on the treatment and the tumor type. Hence, although this concept is presented here for brain metastases, this could be generalized to other tumor types like glioblastoma, and extended to combine other physiological, metabolic and molecular imaging parameters.

In summary, in this dissertation, we discussed two important aspects of tumor physiology in assessing response of brain metastases to radiation therapy. However, these results should be further validated in the future using a larger dataset and other types of tumor, e.g. glioblastoma or head & neck cancer. Also, including the predictive value of other physiological parameters such as ^{11}C-MET PET could also add value to the predictive models developed in this dissertation and should be further investigated in the future.

References

[1] Lassman AB, and DeAngelis LM. Brain metastases. Neurol Clin N Am 2003; 21: 1–23.

[2] Nussbaum ES, Djalilian HR, Cho KH, and Hall WA. Brain metastases. Histology, multiplicity, surgery, and survival. *Cancer* 1996; 78:1781-1788.

[3] Nguyen T and DeAngelis LM. Treatment of Brain Metastases. J Support Oncol 2004; 2:405–416.

[4] Chao JH, Phillips R, and Nickson JJ. Roentgen-ray therapy of cerebral metastases. Cancer 1954; 7:682–689.

[5] Leksell L. The stereotaxic method and radiosurgery of the brain. Acta Chir Scand 1951; 102:316–329.

[6] Shaw E, Scott C, Souhami L, Dinapoli R, Kline R, Loeffler J, and Farnan N. Single dose radio-surgical treatment of recurrent previously irradiated primary brain tumors and brain metastases: final report of RTOG protocol 90-05. Int J Radiat Oncol Biol Phys 2000; 47:291-298.

[7] Sze G, Milano E, Johnson C, and Heier L. Detection of brain metastases: comparison of contrast enhanced MR with unenhanced MR and enhanced CT. AJNR Am J Neuroradiol 1990; 11:785–91.

[8] Prastawa M, Bullitt E, Moon N, Leemput KV, and Gerig G. Automatic brain tumor segmentation by subject specific modification of atlas priors. Acad Radiol 2003; 10:1341–1348.

[9] Chang EL, Wefel JS, Hess KR et al. Neurocognition in patients with brain metastases treated with radiosurgery or radiosurgery plus whole-brain irradiation: a randomized controlled trial. Lancet Oncol 2009; 10:1037-44.

[10] J. Folkman, "The role of angiogenesis in tumor growth", *Seminar Cancer Biology.,* 3, pp.65–71, 1992.

[11] Amoroso, F. D. Porto, C. D. Monaco, P. Manfredini, and A. Afeltra, "Vascular endothelial growth factor: a key mediator of neoangiogenesis: a review", *European Review for Medical Pharmacological Science,* 1, pp. 17–25, 1997.

[12] D. J. Brat, E. G. V. Meir. "Glomeruloid microvascular proliferation orchestrated by VPF/VEGF: a new world of angiogenesis research", *American Journal Pathology,.* 158, pp. 789–796, 2001.

[13] S. W. Schneider, T. Ludwig, L. Tatenhorst L, S. Braune, H. Oberleithner, V. Senner and W. Paulus, "Glioblastoma cells release factors that disrupt blood-brain barrier features", *Acta Neuropathology (Berl),.* 107, pp. 272–276, 2004.

[14] K. H. Plate, W. Risau. "Angiogenesis in malignant gliomas", *Glia,.* 15, pp. 339–47, 1995.

[15] E. L. Lund, M. S.Thomsen, H. S. Poulsen, P. E. Kristjansen, "Tumor angiogenesis: a new therapeutic target in gliomas", *Acta Neurologica Scandinavia,.* 97, pp. 52–62, 1998.

[16] G. U. Dachs, D. J. Chaplin. "Microenvironmental control of gene expression: implications for tumor angiogenesis, progression, and metastasis", *Seminar Radiation Oncology,.* 8, pp. 208–216, 1998.

[17] Jackson A, Buckley DL, Parker GJM. Contrast-enhanced magnetic resonance imaging in oncology. Berlin: Springer, 2005.

[18] Jackson A, O'Connor JPB, Parker GJM, Jayson GC. Imaging tumor vascular heterogeneity and angiogenesis using dynamic contrast-enhanced magnetic resonance imaging. Clin Cancer Res 2007; 13:3449–3459.

[19] Yankeelov TE, Gore JC. Dynamic contrast enhanced magnetic resonance imaging in oncology: theory, data acquisition, analysis, and examples. Curr Med Imaging Rev 2007; 3:91–107.

[20] Tofts PS, Brix G, Buckley DL, et al. Estimating kinetic parameters from dynamic contrast-enhanced T(1)-weighted MRI of a diffusable tracer: standardized quantities and symbols. J Magn Reson Imaging 1999; 10:223-232.

[21] Hayes C, Padhani AR, Leach MO. Assessing changes in tumor vascular function using dynamic contrast-enhanced magnetic resonance imaging. NMR in Biomedicine 2002; 15:154 – 63.

[22] Brasch R, Turetschek K. MRI characterization and grading angiogenesis using a macromolecular contrast media: status report. Eur J Radiol 2000; 23:148 – 55.

[23] Eyal E, Degani H, Model-based and model-free parametric analysis of breast dynamic-contrast-enhanced MRI. NMR Biomed 2009; 22: 40–53.

[24] Padhani AR, Liu G, Mu-Koh D, Chenevert TL, Thoeny HC, Takahara T, Dzik-Jurasz A, Ross BD, Cauteren MV, Collins D, Hammoud DA, Rustin GJS, Taouli B, and Choyke PL. Diffusion-weighted magnetic resonance imaging as a cancer biomarker: consensus and recommendations. Neoplasia 2009; 11:102-125.

[25] Patterson DM, Padhani AR, and Collins DJ. Technology insight: water diffusion MRI-a potential new biomarker of response to cancer therapy. Nat Clin Pract Oncol 2008; 5:220-233.

[26] Moffat BA, Chenevert TL, Meyer CR, Mckeever PE, Hall DE, Hoff BA, Johnson TD, Rehemtulla A and Ross BD. The Functional Diffusion Map: An Imaging Biomarker for the Early Prediction of Cancer Treatment Outcome. Neoplasia 2006; 8:259-267.

[27] Moffat BA, Chenevert TL, Lawrence TS, Meyer CR, Johnson TD, Dong Q, Tsien CI, Mukherji S, Quint DJ, Gebarski SS, Robertson PL, Junck LR, Rehemtulla A, and Ross BD. Functional diffusion map: A noninvasive MRI biomarker for early stratification of clinical brain tumor response. Proc Natl Acad Sci 2005; 102: 5524-5529.

[28] Brunelli R. Template Matching Techniques in Computer Vision: Theory and Practice. John Wiley and Sons, 2009.

[29] Lee Y, Hara T, Fujita H, Itoh Sh, and Ishigaki T. Automated detection of pulmonary nodules in helical CT images based on an improved template-matching technique. IEEE Trans. Medic. Imaging 2001; 20:595-604.

[30] Li Q, Kutsuragawa Sh, and Doi K. Computer-aided diagnostic scheme for lung nodule detection in digital chest radiographs by use of a multiple-template matching technique. Med Phys 2001; 28:2070-76.

[31] Bae KT, Kim JS, Na YH, Kim KG, and Kim JH. Pulmonary nodule: automated detection on CT images with morphologic matching algorithm-preliminary results. Radiology 2005; 236:286-294.

[32] Wang P, DeNunzio A, Okunieff P, and O'Dell WG. Lung metastases detection in CT images using 3D template matching. Med Phys 2007; 34:915-922.

[33] Osman XO, Ozekes S, and Ucan ON. Lung nodule diagnosis using 3D template matching. Comput Biol Med 2007; 37:1167–1172.

[34] Moltz JH, Schwier M, Peitgen HO. A general framework for automatic detection of matching lesions in follow-up CT. ISBI 2009; 843-846.

[35] Tourassi GD, Vargas-Voracek R, Catarious DM, and Floyd CE. Computer-assisted detection of mammographic masses: A template matching scheme based on mutual information. Med Phys 2003; 30:2123-2130.

[36] Lochanambal KP, Karnan M, Sivakumar R. Identifying masses in mammograms using template matching. International Conference on Communication Software and Networks 2010; 339–342.

[37] Ambrosini RD, Wang P, and O'Dell WG. Computer-Aided Detection of Metastatic Brain Tumors Using Automated Three-Dimensional Template Matching. J of Mag Reson Imaging 2010; 31:85-83.

[38] Kansal AR, Torquato S, Harsh GR, Chioca EA, and Deisboeck TS. Simulated brain tumor growth dynamics using a three-dimensional cellular automaton. J Theor Biol 2000; 203:367-382.

[39] Chen CH, Pau LF, and Wang PSP. The Handbook of Pattern Recognition and Computer Vision, 2nd ed. Singapore: World Scientific Publishing, 1998.

[40] Gonzalez RC, and Woods RE. Digital Image Processing: 2nd Edition. Prentice-Hall Inc., 2002.

[41] Chakraborty DP, and Winter LHL. Free-Response Methodology: Alternate analysis and a new observer-performance experiment. Radiology 1990; **174**:873-881.

[42] Alirezaie J. Jernigan ME, and Nahmias C. Automatic Segmentation of Cerebral MR Images using Artificial Neural Networks. IEEE Trans Nucl Sci 1998; 45:2174-2182.

[43] http://www.fil.ion.ucl.ac.uk/spm/

[44] Ling CC, Humm J, Larson S, et al. Towards multidimensional radiotherapy (MD-CRT): Biological imaging abd biological conformality. Int J Radiat Oncol Biol Phys 2000; 3:551-560.

[45] Goitein M, and Niemierko A. Intensity modulated therapy and inhomogeneous dose to the tumor: a note of caution. Comment in: Int J Radiat Oncol Biol Phys 1996; 38:1138–1139. Int J Radiat Oncol Biol Phys 1196; 36:519–522.

[46] Cao Y, Shen Z. Integrated software tools for multi-modality functional images in cancer clinical trials. Med Phys 2007; 34:2395-2395.

[47] Cao Y, Nagesh V, Hamstra D, et al. The extent and severity of vascular leakage as evidence of tumor aggressiveness in high-grade gliomas. Cancer Res 2006; 66:8912-8917.

[48] Cao Y, Tsien CI, Nagesh V, et al. Survival prediction in high-grade gliomas by perfusion MRI prior to and during early stage of RT. Int J Rad Onc Biol Phys 2006; 64: 876-885.

[49] Huber PE, Hawighorst H, Fuss M, et al. Transient enlargement of contrast uptake on MRI after linear accelerator (linac) stereotactic radiosurgery for brain metastases. Int J Radiat Oncol Biol Phys 2001; 49: 1339-49.

[50] Eng J. ROC analysis: web-based calculator for ROC curves. Baltimore: Johns Hopkins University [updated 2006 May 17]. Available from: http://www.jrocfit.org.

[51] DeLong ER, DeLong DM, and Clarke-Pearson DL. Comparing the area under two or more correlated receiver operating characteristic curve: a nonparametric approach, Biometrics 1988; 44: 837-845.

[52] Galba CJ, Chenevert TL, Meyer CR et al. The parametric response map is an imaging biomarker for early cancer treatment outcome, Nature in Medicine 2009; 15:572-576, 2009.

[53] Law M, Young R, Babb J et al. Histogram analysis versus region of interest analysis of dynamic susceptibility contrast perfusion MR imaging data in the grading of cerebral Gliomas. Am J Neuroradiol 2007; 28:761-766.

[54] Menegakis A, Eicheler W, Yaromina A et al. Residual DNA double strand breaks in perfused but not in unperfused areas determine different radiosensitivity of tumours. Radiotherapy and Oncology 2011; 100: 137–144.

[55] Wang P, Popovtzer A, Eisbruch A, Cao Y, An approach to identify, from DCE MRI, significant subvolumes of tumors related to outcomes in advanced head-and-neck cancer. Med Phys 2012; 39:5277-85.

[56] Eyal E, Degani H, Model-based and model-free parametric analysis of breast dynamic-contrast-enhanced MRI. NMR Biomed 2009; 22: 40–53.

[57] Frouin F, Bazin JP, Paola MD, Jolivet O, Paola RD. FAMIS: a software package for functional feature extraction from biomedical multidimensional images. Comput Med Imaging Graph 1992; 16: 81–91.

[58] Zagdanski AM, Sigal R, Bosq J, Bazin JP, Vanel D, Paola RD. Factor analysis of medical image sequences in MR of head and neck tumors. Am J Neuroradiol 1994; 15: 1359–1368.

[59] Yoo SS, Gil Choi B, Han JY, Hee Kim H. Independent component analysis for the examination of dynamic contrast-enhanced breast magnetic resonance imaging data: preliminary study. Invest Radiol 2002; 37: 647–654.

[60] Twellmann T, Saalbach A, Gerstung O, Leach MO, Nattkemper TW. Image fusion for dynamic contrast enhanced magnetic resonance imaging. Biomed Eng Online 2004; 3: 35.

[61] Eyal E, Bloch NB, Rofsky NM, Furman-Haran E, Genega EM, Lenkinski RE, Degani H. Principal component analysis of dynamic contrast enhanced MRI in human prostate cancer. Invest Radiol 2010; 45:174-181.

[62] Eyal E, Badikhi D, Furman-Haran E, Kelcz F, Kirshenbaum KJ, Degani H. Principal component analysis of breast DCE-MRI adjusted with a model-based method. J Magn Reson Imaging 2009; 30:989–998.

[63] Bruwer MJ, MacGregor JF, Noseworthy MD. Dynamic contrast-enhanced MRI diagnostics in oncology via principal component analysis. J Chemometrics 2008; 22: 708–716.

[64] Spath H. One Dimensional Spline Interpolation Algorithms. Wellesley, MA, A K Peters Ltd. 1995; 416p.

[65] Cao Y, Shen Z, Chenevert TL, Ewing JR. Estimate of vascular permeability and cerebral blood volume using Gd-DTPA contrast enhancement and dynamic T2*-weighted MRI. J Magn Reson Imaging 2006; 24:288–296.

[66] Law M, Yang S, Babb JS, Knopp EA, Golfinos JG, Zagzag D, Johnson G. Comparison of cerebral blood volume and vascular permeability from dynamic susceptibility contrast-enhanced perfusion MR imaging with Glioma grade. Am J Neuroradiol 2007; 25:746-755.

[67] Law M, Young RJ, Babb JS et al. Gliomas: Predicting time to progression or survival with cerebral blood volume measurements at dynamic susceptibility-weighted contrast-enhanced perfusion MR Imaging. Radiology 2008; 247:490-498.

[68] Tuncbilek N, Kaplan M, Altaner S, Atakan IH, Süt N, Inci O, Demir MK. Value of dynamic contrast-enhanced MRI and correlation with tumor angiogenesis in bladder cancer. AJR Am J Roentgenol. 2009; 192:949-955.

[69] Cao Y, Li D, Shen Z, Normolle D. Sensitivity of Quantitative Metrics Derived from DCE MRI and a Pharmacokinetic Model to Image Quality and Acquisition Parameters. Acad Radiol 2010; 17:468–478.

[70] Moffat BA, Chenevert TL, Meyer CR, Mckeever PE, Hall DE, Hoff BA, Johnson TD, Rehemtulla A and Ross BD. The Functional Diffusion Map: An Imaging Biomarker for the Early Prediction of Cancer Treatment Outcome. Neoplasia 2006; 8:259-267.

[71] Moffat BA, Chenevert TL, Lawrence TS, Meyer CR, Johnson TD, Dong Q, Tsien CI, Mukherji S, Quint DJ, Gebarski SS, Robertson PL, Junck LR, Rehemtulla A, and Ross BD. Functional diffusion map: A noninvasive MRI biomarker for early stratification of clinical brain tumor response. Proc Natl Acad Sci 2005; 102: 5524-5529.

[72] Hamstra DA, Galban CJ, Meyer CR, Johnson TD, Sundgren PC, Tsien CI, Lawrence TS, Junck L, Ross DJ, Rehemtulla A, Ross BD, and Chenevert TL. Functional Diffusion Map As an Early Imaging Biomarker for High-Grade Glioma: Correlation With Conventional Radiologic Response and Overall Survival. J Clin Oncol 2008; 26: 3387-3394.

[73] Ellingson BM, Cloughesy TF, Lai A, Mischel PS, Nghiemphu PL, Lalezari S, Schmainda KM, and Pope WB. Graded functional diffusion map–defined characteristics of apparent diffusion coefficients predict overall survival in recurrent glioblastoma treated with bevacizumab. Neuro Oncol 2011; 13: 1151-1161.

[74] Ellingson BM, Cloughesy TF, Zaw T, Lai A, Nghiemphu PL, Harris R, Lalezari S, Wagle N, Naeini KM, Carrillo J, Liau LM, and Pope WB. Functional diffusion maps (fDMs) evaluated before and after radiochemotherapy predict progression-free and overall survival in newly diagnosed glioblastoma. Neurooncol 2012 14: 333-343.

[75] Ellingson BM, Cloughesy TF, Lai A, Nghiemphu PL, and Pope WB. Nonlinear registration of diffusion-weighted images improves clinical sensitivity of functional diffusion maps in recurrent glioblastoma treated with bevacizumab. Magn Reson Med 2012; 67: 237-245.

[76] Pope WB, Kim HJ, Huo J, Alger J, Brown MS, Gjertson D, Sai V, Young JR, Tekchandani L, Cloughesy T, Mischel PS, Lai A, Nghiemphu P, and Rahmanuddin S, Goldin J. Recurrent glioblastoma multiform: ADC histogram analysis predicts response to bevacizumab treatment. Radiology 2009; 252: 182-189.

[77] Pope WB, Qiao XJ, Kim HJ, Lai A, Nghiemphu P, Xue X, Ellingson BM, Schiff D, Aregawi D, Cha S, Puduvalli VK, Wu J, Yung WA, Young GS, Vredenburgh J, Barboriak D, Abrey LE, Mikkelsen T, Jain R, Paleologos NA, Lada P, Prados M, Goldin J, Wen PY, and Cloughesy T. Apparent diffusion coefficient histogram analysis stratifies progression-free and overall survival in patients with recurrent GBM treated with bevacizumab: a multi-center study. J Neurooncol 2012; 108: 491-8.

[78] Pope WB, Lai A, Mehta R, Kim HJ, Qiao J, Young JR, Xue X, Goldin J, Brown MS, Nghiemphu PL, Tran A, and Cloughesy TF. Apparent diffusion coefficient histogram

analysis stratifies progression-free survival in newly diagnosed bevacizumab-treated glioblastoma. Am J Neuroradiol 2011; 32: 882-889.

[79] Kang Y, Choi SH, and Kim YJ. Gliomas: histogram analysis of apparent diffusion coefficient maps with standard- or high- b–value diffusion-weighted MR imaging— correlation with tumor grade. Radiology 2011; 261: 882-890.

[80] Nowosielski M, Recheis W, Goebel G, Güler O, Tinkhauser G, Kostron H, Schocke M, Gotwald T, Stockhammer G, and Hutterer M. ADC histograms predict response to anti-angiogenic therapy in patients with recurrent high-grade glioma. Neuroradiology 2011; 53: 291-302.

[81] King AD, Chow KK, Yu KH, Mo FK, Yeung DK, Yuan J, Bhatia KS, Vlantis AC, and Ahuja AT. Head and neck squamous cell carcinoma: diagnostic performance of diffusion-weighted MR imaging for the prediction of treatment Response. Radiology 2012 Ahead of print doi:10.1148/radiol.12120167.

[82] Chang Q, Wu N, Ouyang H, and Huang Y. Diffusion-weighted magnetic resonance imaging of lung cancer at 3.0 T: a preliminary study on monitoring diffusion changes during chemoradiation therapy. Clinical Imaging 2012; 36: 98-103.

[83] Iima M, Bihan DL, Okumura R, Okada T, Fujimoto K, Kanao S, Tanaka S, Fujimoto M, Sakashita H, and Togashi K, Apparent Diffusion Coefficient as an MR Imaging Biomarker of Low-Risk Ductal Carcinoma in Situ: A Pilot Study. Radiology 2011; 260: 364-372.

[84] Kim S, Loevner L, Quon H, Sherman E, Weinstein G, Kilger A,and Poptani H. Diffusion-Weighted Magnetic Resonance Imaging for Predicting and Detecting Early Response to Chemoradiation Therapy of Squamous Cell Carcinomas of the Head and Neck. Clin Cancer Res 2009; 15: 986-994.

[85] Oh J, Henry RG, Pirzkall A, Lu Y, Li X, Catalaa I, Chang S, Dillon WP, Sarah J. and Nelson SJ. Survival analysis in patients with Glioblastoma multiforme: predictive value of choline-

to-NAcetylaspartate index, apparent diffusion coefficient, and relative cerebral blood volume. J Magn Reson Imaging 2004; 19: 546-554.

[86] Monguzzi L, Ippolito D, Bernasconi DP, Trattenero C, Galimberti S, Sironi S. Locally advanced rectal cancer: Value of ADC mapping in prediction of tumor response to radiochemotherapy, Eur J Radiol 2012; ahead of print doi: 10.1016/j.ejrad.2012.09.027.

[87] Hilario A, Ramos A, Perez-Nunez, A, Salvador E, Millan JM, Lagares A, Sepulveda JM, Gonzalez-Leon P, Hernandez-Lain A, and Ricoy JR. The added value of apparent diffusion coefficient to cerebral blood volume in the preoperative grading of diffuse gliomas, Am J Neuroradiol 2012; 33: 701-707.

[88] Oikawa T, Sasaki T, Nakamura M, Shimamura M, Tanahashi N, Omura S, and Tanaka K. The Proteasome Is Involved in Angiogenesis. Biochem Biophys Res Commun 1998; 246: 243-8.

[89] Wang X, Zhang Z, and Yao C. Bortezomib Inhibits the Angiogenesis Mediated by Mesenchymal Stem Cells. Cancer Invest 2012; 30: 657-62.